NASA
Technical
Paper
2825

August 1988

Helicopter Main-Rotor Noise

Determination of Source Contributions Using Scaled Model Data

Thomas F. Brooks,
J. Ralph Jolly, Jr.,
and Michael A. Marcolini

NASA

NASA Technical Paper 2825

1988

Helicopter Main-Rotor Noise

Determination of Source Contributions Using Scaled Model Data

Thomas F. Brooks
Langley Research Center
Hampton, Virginia

J. Ralph Jolly, Jr.
Planning Research Corporation
Hampton, Virginia

Michael A. Marcolini
Langley Research Center
Hampton, Virginia

National Aeronautics and Space Administration

Scientific and Technical Information Division

Symbols

a_0	medium speed of sound, m/s
C_T	rotor thrust coefficient, $\frac{\text{Thrust}}{\rho\pi R^2(\Omega R)^2}$
c	blade chord length, m
F_1, F_2, F_3	dividing frequencies (in figures, used as F1, F2, F3)
f	frequency, Hz
Δf	spectral analysis bandwidth, Hz
f_{bp}	blade passage frequency, Blade number $\times$ Ω, Hz
K	constant
p	acoustic pressure, Pa
q	total pressure, Pa
q_0	ambient total pressure, Pa
R	rotor radius, m
r	observer distance from rotor hub, m
T	rotor period, $2\pi/\Omega$, s/cycle; also thrust, N
t	time, s
$\bar{t}$	normalized time scale
Δt	time between data samples, s
V	tunnel flow velocity, m/s
V_T	rotor tip speed, m/s
V_x	helicopter horizontal velocity, m/s
V_z	helicopter rate of descent, m/s
x	observer position; also tunnel streamwise axis
$\bar{x}$	normalized observer position
y	tunnel spanwise axis
z	tunnel height axis
α_{TPP}	rotor tip-path-plane angle, referenced to tunnel streamwise axis, deg
α'_{TPP}	effective α_{TPP}, corrected for open wind-tunnel effects, deg
$\Delta\alpha$	wind-tunnel correction deflection angle, deg
γ	scale factor, ratio of full-scale to model-scale geometry
$\Delta\xi$	shear-layer refraction angle correction
θ	helicopter descent angle, deg
μ	advance ratio, $V/\Omega R$
ν	induced velocity, m/s
ρ	medium density, kg/m^3
τ	fluctuation duration, s
ϕ	directivity angle of observer, deg

Ω	rotor rotation frequency, rad/s or rpm
Subscripts:	
e	equivalent full-scale flyover value
geo	geometric
m	measured value for model
sl	shear layer
tot	total
Abbreviations:	
BVI	blade-vortex interaction
BWI	blade-wake interaction
corr	corrected
DNW	Deutsch-Niederlandischer Windkanal (German-Dutch Wind Tunnel)
dBA	A-weighted sound pressure level, dB (re 2×10^{-5} Pa)
HHL	higher harmonic loading
Mic	microphone
OASPL	overall sound pressure level, dB
obs	observer
PNL	perceived noise level, dB
Re	Reynolds number
SPL	sound pressure level, dB

Summary

Acoustic data from a test of a 40-percent-sized model MBB BO-105 helicopter main rotor is scaled to equivalent "full-scale" flyover cases. The test was conducted in the anechoic open test section of the German-Dutch Windtunnel (DNW). The operating conditions, for the four-bladed rotor, range from low to moderate flight speeds for various climb and descent rates at design thrust. The measured data are in the form of acoustic pressure time histories and spectra from two out-of-flow microphones underneath and forward of the model. These are scaled to correspond to measurements made at locations 150 m below the flight path of a full-scale rotor. Aerodynamic analyses include open wind-tunnel corrections and a flight condition determination of corresponding full-scale descent rates. Acoustic analyses include determination of frequency adjustments, to account for model size scaling and Doppler effects, and amplitude changes, to correct shear-layer refraction effects and observer distance changes. For the scaled data thus obtained, a detailed analysis is given for the identification in the data of the noise contributions from different rotor noise sources. Key results include a component breakdown of the noise contributions, in terms of noise criteria calculations of A-weighted sound pressure level (dBA) and perceived noise level (PNL), as functions of rotor advance ratio and descent angle. It is shown for the scaled rotor that during descent, impulsive blade-vortex interaction (BVI) noise is the dominant contributor to the noise. In level flight and mild climb, broadband blade-turbulent wake interaction (BWI) noise is dominant due to the avoidance of BVI activity. At high climb angles, BWI is reduced and self-noise from blade boundary-layer turbulence becomes the most prominent.

1. Introduction

NASA Langley Research Center conducted a helicopter main rotor aeroacoustics experiment in the German-Dutch Wind Tunnel (Deutsch-Niederlandischer Windkanal, DNW). The test was conducted with the cooperation of the Deutsche Forschungs- und Versuchsanstalt fur Luft- und Raumfahrt (DFVLR) and with partial support provided by the Federal Aviation Administration (FAA) and the Aerostructures Directorate, USAARTA-AVSCOM. The model tested was a large (40-percent scale) dynamically and Mach number scaled Messerschmitt-Bölkow-Blohm (MBB) BO-105 four-bladed helicopter main rotor. The study is the first to systematically measure helicopter rotor broadband noise, in conjunction with discrete noise sources, in a well-controlled environment for reasonable model scales and operating conditions. Brooks, Marcolini, and Pope (ref. 1) presented details of the test, identified noise sources based on rotor test variations of operational and geometric parameters, and verified broadband noise predictive capability. The present paper presents an additional step in the analysis of this benchmark data base. Herein the noise results are scaled to "full-scale" helicopter flight conditions and quantitative evaluations are made of noise source importance.

Results of reference 1 serve as background for the present paper. A key result was the distinction made possible between the regions of dominance of discrete and broadband sources for the rotor at different operating conditions. An important broadband noise source due to blade-wake interaction (BWI) was newly identified and its character demonstrated. The analysis employed the diagnostic data base and comparisons with predictions for broadband self-noise developed by the National Aeronautics and Space Administration. Four noise mechanisms were identified for the data of this medium-tip-speed main rotor. One is discrete loading noise due to steady and azimuthally dependent blade loading, which dominates the lower harmonics of the blade passage frequency f_{bp}. Next is a discrete source of impulsive character, blade-vortex interaction (BVI), which if present can dominate a large number of harmonics. The sketch of figure 1 illustrates a tip vortex that a blade may encounter. At somewhat higher frequencies, broadband noise dominates because of BWI from blade interactions with turbulence in and about the general rotor wake. The particular turbulence illustrated in figure 1 is that entrained about the representative tip vortex. Broadband self-noise controls the high-frequency part of the spectra. Self-noise is due to blade interaction with boundary-layer and near-wake turbulence. The relative significance of each of these mechanisms is dependent on rotor operating conditions.

The purpose of the present paper is to scale measured model acoustic data to equivalent "full-scale" flyover cases and to use the spectral results to establish the importance of discrete and broadband rotor noise sources as a function of operating conditions. An overview of the test is given, along with the test matrix of interest and details of the data processing. Sections 3 through 5 address the scaling problem. An aerodynamic scaling approach is specified which involves a wind-tunnel correction analysis to determine the effective rotor angles and a flight condition analysis to find the corresponding full-scale descent rates. The acoustic scaling approach presented involves frequency shifts due to model- to full-scale rotor size

ratios and due to the Doppler effect. Also spectral amplitude changes are made to correct for tunnel shear-layer refraction and to account for tunnel-to-flyover observer distance changes. The observer distance calculations depend on determining the effective flyover observer angle corresponding to the particular tunnel test case and microphone. Noise measured for two microphones is scaled to correspond to observer positions located 150 m below "full-scale" helicopter flight paths. Acoustic pressure time histories and narrowband spectra are used to discuss details of the different source mechanisms and their dependence on operating conditions. The spectra regions of dominance are then determined for the sources. Summary results are presented in terms of perceived noise level (PNL) and A-weighted sound pressure level (dBA) as a function of advance ratio μ and descent angle θ.

2. Test Program

Details of the experiment are given in reference 1. Some key features are presented in this section of the hardware and instrument geometry, model scaling, the test matrix of interest, and the acoustic data processing.

2.1. Test Geometry

Figure 2 shows an overview of the test setup in the DNW. The open anechoic configuration is seen which has a nozzle 8 m wide by 6 m high to provide a free jet with a low turbulence potential core. The rotor is positioned in the flow between the nozzle on the right and the collector on the left. Figure 3 is a drawing detailing the tunnel geometry which shows the relationship of the model rotor, at the zero tip-path-plane angle α_{TPP} position, to the microphones. At other α_{TPP} angles the rotor hub changes the x position, with y and z held constant. The microphones of interest are numbered 19 and 21 (below and forward of the model) which are out of the flow and placed 1.1 m above the floor wedge tips.

The rotor is a 40-percent-scale, four-bladed, hingeless BO-105 rotor with a diameter of 4.0 m and a chord of 0.121 m. The blades have a $-8°$ linear twist and a 20-percent cutout from the hub center. The model has a similar blade mass and stiffness distribution compared with full scale, but chord length is slightly larger in scale to maintain the proper ratio between the aerodynamic forces and the mass and elastic forces. Thus, rotor solidity σ is 0.077 rather than the full-scale value of 0.070.

2.2. Test Matrix

For the test cases of interest the rotor speed Ω is a nominal 1050 rpm (hover tip Mach number of 0.64) and the thrust coefficient C_T is 0.0044. The three tunnel velocities V are 19, 38, and 62 m/s which correspond to advance ratios μ of 0.086, 0.173, and 0.282. The rotor tip-path-plane angle α_{TPP} is varied from $-20°$ to $3.5°$, where negative α_{TPP} corresponds to a climb condition. In table 1, the specific values of μ, C_T, and α_{TPP} as referenced to the tunnel centerline are listed for each test run point number. Table 1 also contains the important parameters used in scaling the model data to full scale. These parameters are subsequently developed.

The rotor is operated with "zero flapping" by employing cyclic pitch control. The shaft moment is minimized so that the tip-path plane is approximately perpendicular to the rotor shaft axis.

2.3. Data Processing

The microphone signals were high-pass-filtered at 50 Hz and then recorded on an FM tape recorder such that the response would be flat to 20 kHz. During postprocessing, the data were simultaneously digitized at a sample rate of 2048 samples per rotor revolution, keyed to the 1-per-revolution pulse. For time history studies, data from single rotor revolutions are used, with a nominal Δt between samples of 27.9 μs. The spectral data are ensemble averaged over 200 revolutions, with a nominal bandwidth of $f_{bp}/4$, or 17.5 Hz. Additional detail is found in references 1 and 2.

3. Wind-Tunnel Corrections

The tip-path-plane angle α_{TPP} is referenced to the test section centerline. When a rotor (or any other lifting device) is operated in an open tunnel, the incident flow is deflected more than would occur for flight in free air by an amount $\Delta\alpha$. An effective or corrected angle

$$\alpha'_{\mathrm{TPP}} = \alpha_{\mathrm{TPP}} + \Delta\alpha \tag{1}$$

can be defined which would represent that angle in free air corresponding aerodynamically to the tunnel α_{TPP} value. The angle α'_{TPP} would be used in any performance analysis. This wind-tunnel correction can be determined from the program of Heyson (ref. 3). These corrections are given in table 1 for each of the test cases considered in this report. Note that the largest magnitude correction of $\Delta\alpha$ is less than $5°$. At these low angles, correction using this approach should be quite accurate. Alternately a closed-form solution, although less exact, can be determined to permit physical insight and a more convenient calculation of values in many scaling applications. The analysis is given in appendix A. Calculations of values based on equation (A8) are given

for comparison in table 1 and are seen to closely match the more exact results of Heyson.

4. Flight Condition Analysis

The DNW test matrix is defined based on parameters of μ, α_{TPP}, and C_T for the rotor operated with zero flapping. It is required that the test conditions be matched with equivalent full-scale BO-105 flight cases. In the following development, a force balance is used to relate the parameters to full-scale flight data of the BO-105. It is noted that an apparently similar but independent analysis was performed by Boxwell et al. (ref. 4) for a Bell Cobra helicopter model and related to full scale by using a rotor performance program.

In figure 4, the forces acting on a helicopter in forward flight are shown. The helicopter is descending at angle θ at velocity V. The descent angle θ is positive in descent. The rotor-tip-path plane is oriented at angle α to the ground plane, whereas the tip-path plane is referenced to the flight direction at angle α'_{TPP}. Note that α'_{TPP} is used instead of α_{TPP} to indicate that this analysis is for a rotor in free flight, not in the tunnel environment. The thrust vector T is perpendicular to the rotor plane and must be balanced by the vector sum of the fuselage-rotor weight W and drag D for this nonaccelerating case. Components of T in directions parallel and perpendicular to the ground are F_1 and F_2, respectively. From the geometry, it is seen that

$$\tan\theta = \frac{W - F_2}{F_1} \tag{2}$$

$$\sin\alpha = \frac{F_1}{T} \tag{3}$$

and

$$\frac{F_1}{\cos\theta} = D = \frac{1}{2}\rho V^2 A C_D \tag{4}$$

Equation (4) relates the functional form for drag force. The term C_D is a drag coefficient and A is an equivalent drag area for the helicopter. Using a small angle approximation for α and θ, one obtains

$$\alpha = \frac{\frac{1}{2}\rho V^2 A C_D}{C_T \rho \left(\pi R^2\right) V^2/\mu^2} = \frac{K\mu^2}{C_T} \tag{5}$$

Here α is referenced to the ground. The rotor angle α'_{TPP} is referenced to the flight velocity V and is related by

$$\alpha'_{\mathrm{TPP}} = -\alpha + \theta = \frac{-K\mu^2}{C_T} + \tan^{-1}\left(\frac{V_z}{V_x}\right) \tag{6}$$

where V_z is the rate of descent (positive down) and V_x is the forward velocity parallel to the horizontal ground plane. We have approximately

$$\alpha'_{\mathrm{TPP}} = \frac{-K\mu^2}{C_T} + \frac{V_z}{V_x} = \frac{-K\mu^2}{C_T} + \frac{V_z}{\mu V_T} \tag{7}$$

The constant K is related to fuselage-rotor drag effects. The BO-105 manufacturer, Messerschmitt-Bölkow-Blohm (MBB) of the Federal Republic of Germany, has provided unpublished data to the authors in the form of α'_{TPP} versus μ for different descent rates V_z for the BO-105 full-scale helicopter for trimmed operating conditions. It was found that employing $K = 0.00768$ produced excellent agreement with the data, which encompass the present test range of interest. It is noted that this value corresponds to an equivalent "flat-plate" drag area (ref. 5) of 1.2 m^2 for the helicopter. Employing this value with equation (7) for the case of a gross weight of 2000 kg ($C_T \approx 0.0044$) and design V_T gives

$$\alpha'_{\mathrm{TPP}} = -100\mu^2 + \frac{0.2604 V_z}{\mu} \tag{8}$$

where α'_{TPP} is in degrees and V_z is in meters per second and is positive for descent.

This preceding analysis is for a helicopter in free flight. In the context of the DNW experiment, one can match C_T, μ, and the corrected angle α'_{TPP} as being equivalent to the free-flight case. Also V_z is correct in absolute magnitude, since the model and full-scale V_T are the same for the cases of interest. Equation (8) should then correctly connect the DNW data base to full-scale flight. In the tables and figures of this report, the equivalent flyover descent angle θ is related by

$$\theta = \alpha'_{\mathrm{TPP}} + \frac{0.44\mu^2}{C_T} \tag{9}$$

Sections 3 and 4 establish the flight conditions that match the wind-tunnel model test matrix. Now the acoustic scaling problem must be addressed.

5. Acoustic Scaling

5.1. Model Size Scaling

The acoustic data, both pressure time histories and spectra, can be scaled directly from the DNW 0.4 scale to full scale. Using the Ffowcs-Williams and Hawkings equation, Schmitz et al. (ref. 6) show that given a model with a scale factor of $\gamma = R/R_m$ (where R is the full-scale rotor radius and R_m the model radius), if rotor tip Mach number, μ, C_T, and

rotor angles are matched, then the acoustic pressure time history waveforms are matched. This is true for an observer at x for the same orientation and normalized distance $|x| = r$ away, where $r/R = r_m/R_m$. The acoustic pressure time history for the model with respect to the full-scale pressure time history is

$$p_m(\bar{x}_m, \bar{t}_m) = p(\bar{x}, \bar{t}) \left[\frac{\rho_m \left(a_0^2\right)_m}{\rho a_0^2} \right]$$
$$= p(\bar{x}, \bar{t}) \left[\frac{(p_0)_m}{p_0} \right] \qquad (10)$$

where $p(\bar{x}, \bar{t})$ is the corresponding full-scale pressure history, ρ is the medium density, a_0 is the medium speed of sound, and p_0 is the ambient pressure. The normalized observer positions are denoted by $\bar{x} = x/R$ and $\bar{x}_m = x_m/R_m$. The normalized time scales are denoted by $\bar{t} = t/T$ and $\bar{t}_m = t_m/T_m$, where T is the full-scale rotor period of rotation $2\pi/\Omega$ and the model period is

$$T_m = \left(\frac{1}{\gamma}\right) \left[\frac{a_0}{(a_0)_m} \right] T$$

This compression of the time scale is due to the increased model rotational speed made necessary to match the tip Mach number of the full-scale case. For the model,

$$\Omega_m = \gamma \left[\frac{(a_0)_m}{a_0} \right] \Omega$$

The scaling should be valid for both discrete and broadband noise mechanisms. This all assumes exact scaling of the flow field about the blade which says, for example, that the boundary-layer thickness δ is a set percentage of chord c at corresponding blade locations. Flow similarity can be approximately true only above certain Reynolds number ranges—never exactly true. The question of flow similarity and the self-noise mechanisms are dealt with in section 7.

For matched observer positions, the procedure that scales spectral data to account for rotor size is straightforward. For matched atmospheric conditions, a measured model spectrum defined by dB $[(f)_m]$ with bandwidth $(\Delta f)_m$ becomes a full-scale spectrum dB(f) with bandwidth Δf. The level dB $[(f)]_m$ of say the n'th band equals that of the n'th band dB(f), but since $f = 0.4(f)_m$ and $\Delta f = 0.4(\Delta f)_m$, the acoustic energy is pushed to lower frequencies. Summing power over the same number of bands, of course, would give identical results.

5.2. Flyover and Tunnel Geometry Match

It is desired to scale the DNW data to fixed observer positions on the ground below standard 150-m altitude flyovers. The simple frequency shift procedure given in section 5.1 only accounts for rotor size. In the following analysis, the wind-tunnel–flyover geometries are matched for the test conditions while taking into account shear-layer corrections and the Doppler effects. The flyover geometry is shown in figure 5 where the flight path of the helicopter is 150 m directly above the observer and at a descent angle of θ. For each microphone for a particular test case, the scaled result must match an effective observer position at directivity angle θ_e and observer distance r_e from a noise emission location along the flight path. Both θ_e and r_e are uniquely determined by the test case and the flyover geometry.

The geometric arrangement of the model rotor with respect to the microphones of interest (19 and 21) is shown in figure 6. The rotor is shown with a negative value of angle α_{TPP} whereas the other angles are positive as shown. The figure relates the geometric changes which occur when the angle α_{TPP} is changed. In the test, α_{TPP} changes are accomplished by moving the sting vertically and tilting the rotor. The sting motion is programmed so that the hub remains at the same vertical height but moves horizontally by

$$\Delta x = -4.22 \cos\left(20^\circ + \alpha_{\text{TPP}}\right) + 3.97 \qquad (11)$$

in meters. Negative α_{TPP} (climb condition) gives negative Δx, which places the rotor closer to the nozzle. Also shown in figure 6 is $-\Delta\alpha$ ($-\Delta\alpha$ is positive as shown) which is the open wind-tunnel correction deflection angle in the vicinity of the rotor defined in equation (1). The effective observer angle θ_e is determined from the wind-tunnel condition as follows, corresponding to microphones 19 and 21:

$$\left.\begin{aligned} (\phi_{19})_e &\approx \phi_{19} + \Delta\phi_{19} - \Delta\alpha + \Delta\xi_{19} \\ (\phi_{21})_e &\approx \phi_{21} + \Delta\phi_{21} - \Delta\alpha + \Delta\xi_{21} \end{aligned}\right\} \qquad (12)$$

where

$$\phi_{19} = 88.5^\circ$$
$$\phi_{21} = 62.3^\circ$$
$$\Delta\phi_{19} \approx \frac{-(180/\pi)\ \Delta x \sin\ \phi_{19}}{r_{19}}$$

and

$$\Delta\phi_{21} \approx \frac{-(180/\pi)\ \Delta x \sin\ \phi_{21}}{r_{21}}$$

with $r_{19} = 7.75$ m and $r_{21} = 8.75$ m and $\Delta\xi_{19}$ and $\Delta\xi_{21}$ being shear-layer refraction angle corrections defined in section 5.3. The hub to microphone distance r' is

$$r'_{19} \approx r_{19} + \Delta x \cos \phi_{19} \tag{13a}$$

and

$$r'_{21} \approx r_{21} + \Delta x \cos \phi_{21} \tag{13b}$$

for microphones 19 and 21, respectively. Here a shear-layer refraction distance correction is not required, as discussed later. The observer distance r_e from the flyover geometry of figure 5 is

$$r_e = 150 \left(\frac{\cos \theta}{\sin \phi_e} \right) \tag{14}$$

where ϕ_e is made equal to $(\phi_{19})_e$ and $(\phi_{21})_e$ as determined in equations (12). One may now adjust the spectral level to account for the increased distance r_e compared with that of the test, that is,

$$\left.\begin{aligned} (\Delta \mathrm{dB}_{19})_{\mathrm{geo}} &= 10 \log \left[\frac{\gamma r'_{19}}{(r_{19})_e} \right]^2 \\ (\Delta \mathrm{dB}_{21})_{\mathrm{geo}} &= 10 \log \left[\frac{\gamma r'_{21}}{(r_{21})_e} \right]^2 \end{aligned}\right\} \tag{15}$$

where $\gamma = 2.5$. These values are added to the spectral levels measured in the tunnel for the model.

5.3. Tunnel Shear-Layer Corrections

The shear-layer refraction corrections for angle and amplitude are now addressed. Before reaching the microphones, the noise from the rotor is convected downstream in the tunnel flow and then passes through the open jet shear layer where it is refracted. This results in both an angle and amplitude change in the noise field. These can be dealt with as corrections to apply to the data. In table 2, the correction angles $\Delta\xi_{19}$ and $\Delta\xi_{21}$ (of eqs. (12)) and amplitude corrections $(\Delta \mathrm{dB}_{19})_{\mathrm{sl}}$ and $(\Delta \mathrm{dB}_{21})_{\mathrm{sl}}$ are given for the three wind-tunnel test velocities. These corrections are seen to be small. The values were calculated from a program for the test conditions based on the theory of Amiet (ref. 7). With the corrections, the effect of convection and refraction is removed by redefining the spatial relationship between the noise source and observer. The observer is placed at a corrected position and the source is placed at a retarded position, but the distances between these are at the same measured values (ref. 7). This should make the data representative with the case specified in figure 5 where the noise propagation path is in a medium at rest.

5.4. Doppler Shift

An additional effect to take into account is the Doppler shift of frequency due to the motion of the rotor with respect to the stationary observer of the flyover geometry of figure 5. The data to be scaled, of course, are from fixed rotor and microphone locations. This frequency shift is in addition to that shift previously discussed for the rotor size effect. The equivalent flyover frequency scale becomes

$$f_e = f\,(1 - M \cos \phi_e)^{-1} \tag{16}$$

for the Doppler effect. For the combined Doppler and size effects the frequency scale is

$$f_e = f_m \gamma^{-1}\,(1 - M \cos \phi_e)^{-1} \tag{17}$$

Corresponding bandwidths are defined accordingly with Δf_e and Δf_m replacing f_e and f_m in equation (17). Equation (17) constitutes the complete frequency shift required to scale the measured spectra in this tunnel to equivalent flyover spectra.

Note that no level adjustment is made for a "convective amplification" effect. This is because these effects are already included in the experimental wind-tunnel case where the model encounters the flow and the noise source definition depends on the convective flow of the test. Convective amplification analyses are needed when predicting directivity, such as scaling from static to flight cases, but not in the present case of applying wind-tunnel data to matched flight cases.

5.5. Equivalent Flyover Spectra

In summary, the frequency scale of the tunnel-measured spectra is changed from f_m with bandwidth Δf_m to f_e with bandwidth Δf_e by use of equation (17). The equivalent observer angle ϕ_e with respect to a source emission location on the flight path is given by equations (12) employing equations (1) and (11) and table 2. The total level change to add to the measured spectra is

$$(\Delta \mathrm{dB})_{\mathrm{tot}} = (\Delta \mathrm{dB})_{\mathrm{geo}} + (\Delta \mathrm{dB})_{\mathrm{sl}} \tag{18}$$

from equations (15) and table 2, respectively. The values of these adjustments for the two microphones are given in table 1 for the test cases of interest.

Not included in the above corrections are adjustments due to possible changes in atmospheric conditions. Changes in barometric pressure can be incorporated in equation (10). No adjustments are needed

to account for attenuation due to atmospheric absorption for the scaled overflight measurement distances involved here. Also no ground plane correction is included—the observer is still in free space. One would need to add +3 dB or +6 dB to account for ground effects for microphones mounted 1.5 m above the surface or flush mounted on the surface, respectively.

6. Results

The interaction of the rotor blade with tip vortices and wakes of previous blades, and the resultant noise, depends to the first order on the rotor tip-path-plane angle. This dependency is shown in reference 1 by employing data from an overhead microphone. Here in a parallel manner, figure 7 shows a series of instantaneous acoustic pressure time histories obtained from microphone 19 under the rotor. The rotor operated at a nominal advance ratio μ of 0.173 and $C_T = 0.0044$ for the three different tunnel-referenced α_{TPP} values shown. The corresponding wind-tunnel-corrected angles α'_{TPP} are also given. For each α_{TPP} the pressure shown is for a sample period T of 1 rotor revolution. Also shown is another sample taken 3 periods later to illustrate acoustic pressure signal variability. Samples of 1 and 2 periods later showed about the same variability demonstrating the independence of the samples.

Figure 7(a) is a mild descent rotor case ($\alpha_{\text{TPP}} = 1.6°$) where BVI is occurring. In this case, the rotor wake stays in and about the rotor disk plane resulting in the interactions. The most intense BVI impulsive noise is seen as the large negative peaks occurring at 1/4 rotor period. For reference, a rough approximation of the time duration of this BVI is indicated by the period ratio τ_A/T. When comparing the two periods shown in figure 7(a), the particular BVI appears phase locked with the period of revolution. Other BVI occurrences, many of approximately the same τ_A/T duration, of both positive and negative impulses are more random in time occurrence and intensity. These BVI's are probably with "older," more evolved tip vortices, whereas the former is with the most recent, and thus more phased-locked, shed tip vortex. Regardless of the variability, the BVI acoustic signal is deterministic in character and must be thought of as discrete noise. This is because conceptually a deterministic aerodynamic analysis of the flow distribution, coupled with an acoustic analysis, could produce a similar time history and spectrum. Changing from the $\alpha_{\text{TPP}} = 1.6°$ descent to a climb condition virtually eliminates BVI activity as seen in figure 7(b) for $\alpha_{\text{TPP}} = -3.9°$ for the same μ and C_T values. Here relatively mild interactions replace the sharp BVI impulses of figure 7(a). The larger separation distances for the tip vortices to the blades cause the impulsive BVI noise to degenerate to a non-impulsive higher harmonic loading type noise. Also indicated in figure 7(b) are acoustic pressure fluctuations with a typical duration of τ_B/T. They are also present in figure 7(a) but now are more evident with the disappearance of BVI. These fluctuations are identified in reference 1 as BWI noise. A sketch of wake region turbulence is shown in figure 1. A typical turbulence of length scale λ_B is indicated. A crude approximation of λ_B may be made by associating λ_B with the value $\tau_B/T = 0.007$ given in figure 7(b). Assuming dominant noise production at $0.8R$ on the advancing blade side, one determines $\lambda_B \approx 0.7c$. A corresponding analysis to determine a typical BVI "encounter length" λ_A gives $\lambda_A \approx 3.0c$. A more negative α_{TPP} of $-9.9°$ reduces the BWI noise as seen in figure 7(c). This increased climb case further removes the rotor wake from the rotor disk area. Finer grain fluctuations are now observed with a duration that is approximated to be on the order of $\frac{\tau_C}{T} \approx 0.002$. Also reduced in level is low-frequency loading noise at period $\frac{1}{f_{bp}} = \frac{T}{4}$.

The spectra corresponding to the cases of figure 7 are given in figure 8. Indicated are the spectral regions controlled by the various rotor noise mechanisms as well as the frequencies corresponding to the nominal fluctuation periods τ_A for BVI and τ_B for BWI. The nominal period τ_C corresponds to a frequency range dominated by the boundary-layer-related self-noise. The spectral presentation shows quite clearly that in going from the mild descent to the mild climb case, BVI disappears, whereas the low-frequency loading noise, BWI noise, and self-noise generally maintain or increase their levels. In the same frequency range as BVI, but much lower in level, is the higher harmonic loading (HHL) noise. At the higher climb case, BWI is reduced, leaving self-noise to control a larger portion of the spectrum.

In order to show spectral detail at lower frequencies, the spectra of figure 8 are given in figure 9 for a lower frequency range. For the mild descent case where $\alpha_{\text{TPP}} = 1.6°$ the first 20 harmonics of f_{bp} are visible; for the others, less than 10 are seen. However, significant contributions appear to extend past 30 harmonics for the discrete BVI and/or HHL noise, although the previously mentioned pressure signal variability (nonrepeatability between 1-per-revolution samples) causes spectral smearing and resulting broadband appearance. This effect of signal jitter is examined by Brooks (ref. 8). At higher frequencies, the noise is broadband in mechanism as well as appearance.

6.1. Data Presentation

A key contribution of this report is the presentation of acoustic pressure histories and scaled spectra for the full range of operating conditions tested. These data are presented in appendix B in a manner somewhat paralleling that of figures 7 and 8. Because the scaled spectra are employed in noise criteria calculations which identify noise components, the spectra in appendix B are given with multiple frequency and level scales as well as source region identification. Figure 10 illustrates the format. The narrowband noise spectrum is of microphone 21 for a descent case ($\alpha_{TPP} = 3.6°$). The spectral scales SPL_m and f_m are the measured spectral level and frequency obtained for the model. The scales SPL_e and f_e are scaled spectral level and frequency for the corresponding equivalent flyover case as determined by the methods defined previously.

The spectrum of figure 10 is divided into regions where the four individual source mechanisms are identified as dominant. These divisions are based on observation and arguments such as those of figures 8 and 9 along with guidance from other examples given in reference 1 which contain self-noise prediction comparisons. The estimated dividing frequencies F_1, F_2, and F_3 are taken as those frequencies where adjoining source spectra equally contribute to the spectral level. The choices are believed to be accurate, here and for the spectra in appendix B, within 50 Hz model-scale frequency for F_1 and within 500 Hz for F_2 and F_3. The dominant spectral regions are used in assessing the relative importance in the spectra of the sources for different rotor operating cases. Each region of course contains contributions not only from its dominant source but also from the sources of adjoining regions. Therefore, error is introduced when describing a region as a single source region. Fortunately, however, these errors are offsetting between the adjoining regions. Errors of this nature are again addressed in section 7. It is noted here that a more exacting separation of source contributions would require substantial spectral modeling and analysis not warranted by the requirements of this report.

With regard to the spectral weighting analysis, spectral levels are required for high enough full-scale flyover f_e frequencies to permit determination of one-third-octave-band levels through the 10-kHz band. It is seen in figure 10 that the spectrum is not defined much beyond $f_e = 6$ kHz. The 3-dB down point for the antialiasing filter is at a model frequency of $f_m = 16$ kHz. Indicated in figure 10 is a line representing an extension to the spectrum defined by

$$SPL_m\,(f_m > 14.7\text{ kHz}) = dB' - 10\,\frac{(f_m - 14.7\text{ kHz})}{15\text{ kHz}}$$

where dB′ is the average SPL_m of the last 10 narrowband levels below 14.7 kHz. This, when converted to SPL_e and f_e, is taken to define the higher frequency spectral range in all PNL and A-weighted SPL (dBA) calculations. This curve-fit equation was determined from the wider frequency range data of reference 1. The net effect of any error from the spectral fit in determining self-noise contribution to dBA is estimated to be negligible. The effect is further minimized when considering the total PNL and dBA calculations from all mechanisms.

Another adjustment required for the spectra was the removal of contaminants at two locations near $f_m = 10$ kHz. The contaminants were extraneous tones caused by tape head vibration during playback and were located at identical frequencies for all spectra. The levels of the flat regions, which replace the tones, are taken as the average SPL_m of 10 narrowband levels below the contamination regions.

6.2. Scaled Results

The scaled spectral results of appendix B are now employed in calculations of the noise assessment criteria (ref. 9) of A-weighted sound pressure level (dBA) and perceived noise level (PNL). Table 3 summarizes the frequency limit choices, as well as PNL, dBA, and linear SPL calculations. Figure 11 shows the dBA results for the forward microphone 21 as a function of descent angle θ for different advance ratios μ. For each case, the total dBA value is given, along with the contributions to the total from those spectral regions dominated by the different sources. The limits of the regions are defined from the F_1, F_2, and F_3 frequencies. The results indicate that the BVI and HHL noise regions dominate the calculations of dBA for the rotor in descent. For climb cases, the broadband sources of BWI and self-noise dominate. The low-frequency loading noise contributes little to dBA. It should be noted in interpreting figure 11 that the scaled observer locations show little variation in most cases with respect to the flight paths. From table 1, one may approximate $r_e \approx 163$ m and $\phi_e \approx 65°$ for all cases of figure 11.

Figure 12 shows the dBA results for microphone 19, in an identical format to that of figure 11, where $r_e \approx 148$ m and $\phi_e \approx 94°$. The results here are very similar to those found for microphone 21. There appears to be some decrease in the BVI/HHL sources and some increase in the BWI source. The

differences are totally due to rotor source directivity differences.

The dBA results of figure 11 for microphone 21 are shown in a different format in figure 13(a). Each test case is indicated by a plus sign and its dBA value is given to the left. The contour lines show approximate trends for the values. The hatched areas show where the spectral regions of the different noise sources dominate the calculation of dBA. The inset sketch illustrates the observer location with respect to two example flight paths. Figure 13(b) shows the corresponding results where PNL is calculated from the spectra of microphone 21. The trends are very similar.

In figure 14, the dBA and PNL contours and regions of source dominance for microphone 19 are shown. The small increase in the importance of the broadband sources is seen, especially near the level flight condition. Also calculated and listed in table 3 for microphones 19 and 21 are the linearly weighted overall sound pressure levels (OASPL) for the scaled observer as well as the contributions from the individual sources. The linear spectral weighting makes the low-frequency loading noise dominant and diminishes the relative importance of the broadband sources.

7. Scope and Accuracy of Results

These noise criteria calculations cannot be construed as an overall evaluation of the importance of helicopter (in this case an MBB BO-105) noise sources as functions of operating conditions. The results are of course for a main rotor alone—no tail rotor, engine, or transmission are present. Also the results represent only two noise emission-observer points along each flight path, although the large range of flight paths presented make the results in one sense more general. No tone corrections to PNL values were made. A more complete evaluation of the rotor sources would include a calculation of effective perceived noise levels (EPNL). Of course, this would require arrays of measurement locations not available here. However, the general results of such measurements may possibly be anticipated. BVI noise can often have directivity with strong levels at shallow angles forward of the aircraft (ref. 10), whereas the broadband source directivities tend to be dipole in character with maximum levels generally underneath the rotor. Therefore if the data were available to produce EPNL results similar to the main rotor results shown for PNL and dBA, one would expect somewhat increased relative levels of BVI/HHL noise over those already shown.

7.1. Source Contribution Considerations

In section 6, sources of error are discussed which apply to the noise criteria calculations. In figures 11 and 12, the component noise contributions to dBA refer specifically to the integrated spectral regions, which are dominated by particular noise mechanisms. The regions also contain noise from mechanisms of adjoining regions due to overlapping source spectra. The limits of the regions are bounded by frequencies F_1, F_2, and F_3, shown in appendix B. From the discussion of the accuracy of F_1, F_2, and F_3 choices, the error associated with the component values should not exceed 1 dBA for most cases. The source overlap problem increases the potential for error, although these errors tend to offset between adjoining regions. The net errors should still be small (within about 1 to 2 dB) for source mechanisms which are major contributors to the total levels. For those mechanisms which make negligible contributions, errors may be as high as 3 to 4 dB for some cases. The results shown in figures 13 and 14 are of course affected by this error only to the extent that the source dominance area boundaries could be shifted slightly. Other potential error sources, such as the measured spectra modifications discussed in section 6, should not in any significant way add to the net errors estimated.

7.2. Scaling Concerns

As mentioned in section 5, the scaling of the 40-percent rotor model acoustic data to full scale assumes that the deterministic and turbulent flow field about the blades is exactly scaled. Whereas the test Mach numbers did match the corresponding full-scale cases, Reynolds numbers (Re) were 40 percent of full scale. By nearly all testing standards, this model is large, with Re sufficiently high enough to closely match the primary features of the full-scale flow conditions. Based on this anticipation, the reduced Re with respect to the discrete sources of loading and BVI are expected to have rather small impact on the results shown here. The effect on BWI noise is also expected to be small because the Re values should be sufficiently high to produce similar wake turbulence. The actual interaction processes for BVI and BWI are believed to be independent of Re effects, at least to first order for the range of Re found for the model and full-scale rotor.

In contrast to these interaction noise sources, blade self-noise can be strongly influenced by Re conditions. The subject is treated extensively in reference 1 where the various self-noise mechanisms are examined. For the present results, the only mechanism that is significantly affected by the reduced Re is the laminar boundary-layer–vortex-shedding

noise. The vortex shedding occurs over blade portions where the boundary layer is mostly laminar over at least one side of the blade. The mechanism is increased with increased rotor C_T (increased pitch) and decreased Re. For all the data of reference 1 which match the present data (C_T = 0.0044 and rotor speed Ω_m = 1050 rpm), the vortex-shedding mechanism appears to have increased the measured total self-noise by at most 3 dB, generally less, and only in limited frequency ranges. This conclusion is based on the detailed comparison between prediction and data given in reference 1. It is then concluded that the scaled spectra of appendix B may contain somewhat elevated levels in portions of the self-noise spectra. The integrated results for the self-noise portions of dBA and PNL should be less elevated, on the order of 1 to 2 dB for some cases and 0 dB for other cases. For total levels the effect should be negligible.

Clearly, although one can justify scaling the self-noise for this rotor model for these conditions, one should be cautious when applying the procedure to smaller or slower rotors (lower Re) and/or increased C_T values than those presented here.

8. Concluding Remarks

An aerodynamic and acoustic scaling analysis is presented for helicopter main rotor testing in an anechoic open wind tunnel. This analysis scales both rotor operating conditions and acoustic measurements to equivalent full-scale flyover results. The acoustic pressure time histories and spectral data, both measured and scaled, should prove useful in fundamental rotor noise studies as well as noise prediction development and validation. Importantly, the data can be directly compared with full-scale flyover results for corresponding helicopter operating conditions. Corrections applied to scale the model rotor data include wind-tunnel corrections, determination of equivalent flight conditions, rotor size scaling, shear-layer refraction effects, Doppler shift, and distance changes.

An analysis of characteristics and parametric dependence of spectra—given in a talk presented by Brooks, Marcolini, and Pope at the 1987 American Helicopter Society's National Specialists' Meeting on Aerodynamics and Aeroacoustics and extended herein—permits the identification of noise contributions from different mechanisms. In the talk, broadband blade-wake interaction (BWI) noise is identified as a major source in the midfrequency range and the quantitative character of broadband self-noise is defined. In the present paper the spectral regions, where the mechanisms dominate, are specified for a range of rotor conditions.

Noise criteria calculations are made. Both dBA and PNL are presented for spectra from two "overflight" microphone positions. This quantitatively establishes, for the first time, the importance of the different source types with respect to main rotor operation. It is found for this MBB BO-105 rotor that during descent, impulsive blade-vortex interaction (BVI) and/or higher harmonic loading (HHL) noise dominate annoyance. In going to level flight and mild climb the broadband noise mechanism BWI becomes the major contributor to the noise as BVI no longer occurs. At higher climb angles, BWI is reduced and broadband self-noise becomes the most important. Thus both discrete and broadband noise sources must be considered when addressing the complete helicopter noise problem.

NASA Langley Research Center
Hampton, Virginia 23665-5225
June 10, 1988

Appendix A

Simplified Open Wind-Tunnel Correction Analysis for a Rotor

The fundamental basis for wind-tunnel corrections is given by Pope and Harper (ref. 11). For open-jet wind tunnels, the only first-order correction to apply to test data is the open-jet flow deflection or downwash effect correction discussed in section 3. Reduced to the simplest terms, the correction $\Delta\alpha$ of equation (1) is proportioned to the deflection angle that a model (wing or rotor) would cause due to lifting or thrusting; that is,

$$\Delta\alpha = F\frac{\nu}{V} \tag{A1}$$

Here V is the tunnel stream velocity, ν is an induced velocity, and F is a function of model-tunnel relationships such as span load distributions, ratio of model span to tunnel width, shape of test section, and whether the model is near the tunnel centerline. The angle $\Delta\alpha$ is found, first, by determining the deflection angle α_d to relate to ν/V in equation (A1), and then, by determining F by comparing results with values of $\Delta\alpha$ determined from reference 3. The term F is a constant for a given tunnel and rotor model size; F would approach zero for a small rotor in a very large tunnel.

In figure 15 a velocity vector relationship between the undisturbed tunnel velocity V and the rotor-disk-induced velocity which is perpendicular to the rotor operating at zero flapping is shown. The thrust vector T is also perpendicular to the rotor disk. The angle deflection α_d defined here for the rotor is analogous to an angle of attack for an isolated airfoil with regard to gross velocity vectoring. From figure 15, it is seen that

$$\tan\alpha_d = \frac{\nu\ \cos\ \alpha_{TPP}}{V - \nu\ \sin\ \alpha_{TPP}} \tag{A2}$$

which is correct for positive and negative α_{TPP} values. Positive α_{TPP} is shown. From Gessow and Myers (ref. 5, p. 186), the induced velocity for this forward flight case is

$$\nu = \frac{\frac{1}{2}C_T\Omega R}{\left[\left(\frac{V\ \sin\ \alpha_{TPP} - \nu}{\Omega R}\right)^2 + \left(\frac{V}{\Omega R}\ \cos\ \alpha_{TPP}\right)^2\right]^{1/2}} \tag{A3}$$

Upon rearranging, equations (A2) and (A3) become

$$\alpha_d = \tan^{-1}\left[\frac{\left(\frac{\nu}{\Omega R}\right)\ \cos\ \alpha_{TPP}}{\mu - \left(\frac{\nu}{\Omega R}\right)\ \sin\ \alpha_{TPP}}\right] \tag{A4}$$

and

$$\left(\frac{\nu}{\Omega R}\right) = \frac{\frac{1}{2}C_T}{\left[\mu^2 + \left(\frac{\nu}{\Omega R}\right)^2 - 2\mu\left(\frac{\nu}{\Omega R}\right)\ \sin\ \alpha_{TPP}\right]^{1/2}} \tag{A5}$$

If the advance ratio μ is much larger than $\nu/\Omega R$ ($\mu >$ 0.1 is generally a valid region), then equation (A5) becomes

$$\left(\frac{\nu}{\Omega R}\right) = \frac{\frac{1}{2}C_T}{\mu} \tag{A6}$$

The solution for corrected tip-path-plane angle is

$$\alpha'_{TPP} = \alpha_{TPP} + \Delta\alpha = \alpha_{TPP} + F\alpha_d \tag{A7}$$

For the higher tunnel speed cases where equation (A6) is valid,

$$\alpha'_{TPP} = \alpha_{TPP} + F\ \tan^{-1}\left(\frac{C_T\ \cos\ \alpha_{TPP}}{2\mu^2 - C_T\ \sin\ \alpha_{TPP}}\right) \tag{A8}$$

For the more general case, equation (A5) must be solved and employed in equations (A4) and (A7). Calculations of $\Delta\alpha$ made by using equation (A8) are shown in table 1. The value of F chosen was –0.27 to match the results using reference 3. The comparisons show that equation (A8) closely matches the more accurate $\Delta\alpha$ values.

Appendix B

Measured Results for Operating Range

Time History Results

Acoustic pressure time histories, each representing one rotor period, for microphones 19 and 21 are given in figure 16. The figure format is similar to that of figure 7. Figures 16(a)–(g) are for an advance ratio $\mu \approx 0.086$, 16(h)–(p) for $\mu \approx 0.174$, and 16(q)–(u) for $\mu \approx 0.280$. For each value of μ, data are presented in order from most positive to most negative α_{TPP} angle. Given for each case are values of wind-tunnel corrected angle α'_{TPP} and the equivalent flyover descent angle θ. The results for both microphones are presented together to allow easy detection of rotor noise directivity differences for the microphone position as well as the rotor-to-microphone transmission time differences. In analyzing the noise signals one can draw parallels with the analysis of figure 7. It is noted that the microphone 19 results of figures 16(i), (l), and (n) correspond to the same cases as 7(a), (b), and (c), respectively, and are repeated here for completeness.

The cases given for the nominal value $\mu \approx 0.086$, in figures 16(a)–(g), all correspond to climb conditions (descent angles θ are negative). Here the periodic portion of the signal appears to be dominated by higher harmonic loading noise rather than BVI. Microphone 21 shows, for most cases, more HHL noise than microphone 19. This might be expected because of the relative locations of the microphones. Microphone 19 is directly under the rotor hub, whereas microphone 21 is further forward, where loading noise in general should be more intense. The effect of rotor angle change on the data is seen to be a rather gradual decrease in HHL noise and broadband BWI noise as the rotor angle becomes more negative. Large reductions in BWI are not seen until $\theta = -18.8°$ in figure 16(f), where self-noise then dominates.

BVI noise is apparent for the nominal 0.174 cases which correspond to the descent conditions in figures 16(h) and (j). For the climb cases of figures 16(k)–(n), BWI becomes dominant in the data, with BVI not evident. Self-noise dominates at the steeper climb conditions of figures 16(o) and (p). A significant feature of these $\mu \approx 0.174$ cases is the $T/4$ periodicity with which BWI activity is concentrated. This suggests that there are azimuthally localized regions where BWI occurs. Figure 1, which illustrates the wake turbulence being entrained about the tip vortex, may be an accurate presentation of the interacted turbulence, as evidenced by figures 16(h)–(j) showing fixed phase relationships between BVI and BWI activity occurrences. The periodicity with BWI is also seen but to a lesser degree in the data at $\mu \approx 0.086$, indicating possible broader rotor regions where BWI occurs.

Mostly climb conditions are shown for the $\mu \approx 0.280$ cases of figures 16(q)–(u). The prominent BVI impulses appear more numerous and more variable for some angles than that shown for $\mu \approx 0.174$. BWI contributes at small descent angles, such as in figures 16(s) and (t), but generally in the presence of dominating BVI. For the climb case of figure 16(u), BVI and BWI are not seen.

Spectral Results

In figure 17 are spectra from microphone 21 given in the same order as the time histories of figure 16. In figure 18 are those from microphone 19. For each case, equivalent flyover angles and observer positions are given from table 1. The frequency divisions F_1, F_2, and F_3 from table 3 are shown in each figure.

The noise mechanism discussion given for figure 16, of course, applies to figures 17 and 18. The logic of the choices for the frequency limits can be followed by studying the functional behavior of the mechanisms' spectra as the rotor angle is changed. Keep in mind that both the low-frequency loading noise and high-frequency self-noise levels are rather insensitive to rotor angle for constant μ values. Changes in frequency limits depend primarily on the spectral behavior of BVI/HHL and BWI noise.

References

1. Brooks, Thomas F.; Marcolini, Michael A.; and Pope, D. Stuart: Main Rotor Broadband Noise Study in the DNW. *National Specialists' Meeting on Aerodynamics and Aeroacoustics—Proceedings,* American Helicopter Soc., c.1987.
2. Marcolini, Michael A.; and Brooks, Thomas F.: Rotor Noise Measurement Using a Directional Microphone Array. AIAA-87-2746, Oct. 1987.
3. Heyson, Harry H.: *Use of Superposition in Digital Computers To Obtain Wind-Tunnel Interference Factors for Arbitrary Configurations, With Particular Reference to V/STOL Models.* NASA TR R-302, 1969.
4. Boxwell, D. A.; Schmitz, F. H.; Splettstoesser, W. R.; and Schultz, K. J.: Helicopter Model Rotor-Blade Vortex Interaction Impulsive Noise: Scalability and Parametric Variations. *J. American Helicopter Soc.,* vol. 32, no. 1, Jan. 1987, pp. 3–12.
5. Gessow, Alfred; and Myers, Garry C., Jr.: *Aerodynamics of the Helicopter.* Frederick Ungar Publ. Co., c.1952.
6. Schmitz, F. H.; Boxwell, D. A.; Splettstoesser, W. R.; and Schultz, K. J.: Model-Rotor High-Speed Impulsive Noise: Full-Scale Comparisons and Parametric Variations. *Vertica,* vol. 8, no. 4, 1984, pp. 395–422.
7. Amiet, R. K.: Refraction of Sound by a Shear Layer. *J. Sound & Vibration,* vol. 58, no. 4, June 1978, pp. 467–482.
8. Brooks, Thomas F.: *Effect of Signal Jitter on the Spectrum of Rotor Impulsive Noise.* NASA TM-100477, 1987.
9. Edge, Philip M., Jr.; and Cawthorn, Jimmy M.: *Selected Methods for Quantification of Community Exposure to Aircraft Noise.* NASA TN D-7977, 1976.
10. Martin, R. M.; Splettstoesser, W. R.; Elliott, J. W.; and Schultz, K.-J.: *Advancing-Side Directivity and Retreating-Side Interactions of Model Rotor Blade-Vortex Interaction Noise.* NASA TP-2784, AVSCOM TR 87-B-3, 1988.
11. Pope, Alan; and Harper, John J.: *Low-Speed Wind Tunnel Testing.* John Wiley & Sons, Inc., c.1966.

Table 1. Model Rotor Test Conditions and Corresponding Scaled Parameters

Run point	Advance ratio, μ	Descent angle, θ, deg	Mic	Rotor speed, rpm	Thrust coefficient, C_T	α_{TPP}, deg	α'_{TPP}, deg (ref. 3)	$\Delta\alpha$, deg (ref. 3)	$\Delta\alpha$, deg (eq. (A8))	ϕ_e, deg (eqs. (12))	r_e, m (eq. (14))	f_e/f_m (eq. (17))	$(\Delta dB)_{tot}$ (eq. (18))
659	0.086	−1.2	21	1042	0.00430	2.7	−2.0	−4.6	−4.4	67.1	162.8	0.41	−17.1
660	0.086	−3.8	21	1050	0.00441	0.1	−4.5	−4.7	−4.5	67.5	162.0	0.41	−17.1
661	0.088	−6.1	21	1048	0.00434	−2.4	−6.9	−4.6	−4.2	67.8	161.1	0.41	−17.1
662	0.087	−7.8	21	1043	0.00439	−3.9	−8.5	−4.6	−4.3	68.0	160.3	0.41	−17.0
669	0.085	−13.8	21	1046	0.00438	−9.9	−14.6	−4.7	−4.3	68.6	156.4	0.41	−16.9
670	0.084	−18.8	21	1047	0.00435	−14.9	−19.5	−4.6	−4.2	68.9	152.2	0.41	−16.7
671	0.082	−23.9	21	1047	0.00433	−19.9	−24.5	−4.6	−4.1	68.9	147.0	0.41	−16.4
638	0.174	5.5	21	1053	0.00441	3.6	2.4	−1.2	−1.1	64.0	166.1	0.42	−17.0
640	0.175	3.5	21	1050	0.00447	1.6	0.4	−1.2	−1.1	64.3	166.1	0.42	−17.0
642	0.174	1.9	21	1051	0.00445	0.1	−1.1	−1.2	−1.1	64.6	166.0	0.42	−17.0
646	0.172	−0.7	21	1053	0.00446	−2.4	−3.6	−1.2	−1.2	64.9	165.6	0.42	−17.0
649	0.173	−2.1	21	1052	0.00448	−3.9	−5.1	−1.2	−1.1	65.1	165.3	0.42	−17.0
652	0.173	−6.7	21	1053	0.00452	−8.4	−9.6	−1.2	−1.1	65.6	163.6	0.42	−17.0
653	0.171	−8.2	21	1052	0.00443	−9.9	−11.1	−1.2	−1.1	65.7	163.0	0.42	−16.9
656	0.169	−13.4	21	1049	0.00457	−14.9	−16.1	−1.2	−1.2	66.0	159.7	0.42	−16.8
657	0.164	−18.6	21	1042	0.00457	−19.8	−21.1	−1.2	−1.2	66.1	155.5	0.42	−16.5
679	0.281	9.4	21	1055	0.00426	1.6	1.2	−0.5	−0.4	64.0	164.7	0.43	−16.4
677	0.279	7.7	21	1055	0.00434	0.1	−0.3	−0.5	−0.4	64.2	165.1	0.43	−16.5
680	0.280	5.2	21	1054	0.00436	−2.4	−2.8	−0.5	−0.4	64.6	165.4	0.43	−16.5
682	0.281	3.7	21	1052	0.00435	−3.9	−4.3	−0.5	−0.4	64.7	165.5	0.43	−16.5
681	0.278	−2.6	21	1054	0.00436	−9.9	−10.3	−0.5	−0.4	65.3	164.9	0.43	−16.5

Table 1. Concluded

Run point	Advance ratio, μ	Descent angle, θ, deg	Mic	Rotor speed, rpm	Thrust coefficient, C_T	α_{TPP}, deg	α'_{TPP}, deg (ref. 3)	$\Delta\alpha$, deg (ref. 3)	$\Delta\alpha$, deg (eq. (A8))	ϕ_e, deg (eqs. (12))	r_e, m (eq. (14))	f_e/fm (eq. (17))	$(\Delta dB)_{tot}$ (eq. (18))
659	0.086	−1.2	19	1042	0.00430	2.7	−2.0	−4.6	−4.4	93.8	150.3	0.40	−17.8
660	0.086	−3.8	19	1050	0.00441	0.1	−4.5	−4.7	−4.5	94.3	150.1	0.40	−17.8
661	0.088	−6.1	19	1048	0.00434	−2.4	−6.9	−4.6	−4.2	94.6	149.6	0.40	−17.8
662	0.087	−7.8	19	1043	0.00439	−3.9	−8.5	−4.6	−4.3	95.0	149.2	0.40	−17.7
669	0.085	−13.8	19	1046	0.00438	−9.9	−14.6	−4.7	−4.3	95.7	146.4	0.40	−17.6
670	0.084	−18.8	19	1047	0.00435	−14.9	−19.5	−4.6	−4.2	96.0	142.8	0.40	−17.4
671	0.082	−23.9	19	1047	0.00433	−19.9	−24.5	−4.6	−4.1	96.1	138.0	0.40	−17.1
638	0.174	5.5	19	1053	0.00441	3.6	2.4	−1.2	−1.1	91.3	149.4	0.40	−17.6
640	0.175	3.5	19	1050	0.00447	1.6	0.4	−1.2	−1.1	91.8	149.8	0.40	−17.7
642	0.174	1.9	19	1051	0.00445	0.1	−1.1	−1.2	−1.1	92.1	150.0	0.40	−17.7
646	0.172	−0.7	19	1053	0.00446	−2.4	−3.6	−1.2	−1.2	92.5	150.1	0.40	−17.7
649	0.173	−2.1	19	1052	0.00448	−3.9	−5.1	−1.2	−1.1	92.7	150.1	0.40	−17.7
652	0.173	−6.7	19	1053	0.00452	−8.4	−9.6	−1.2	−1.1	93.3	149.2	0.40	−17.6
653	0.171	−8.2	19	1052	0.00443	−9.9	−11.1	−1.2	−1.1	93.4	148.7	0.40	−17.6
656	0.169	−13.4	19	1049	0.00457	−14.9	−16.1	−1.2	−1.2	93.8	146.2	0.40	−17.5
657	0.164	−18.6	19	1042	0.00457	−19.8	−21.1	−1.2	−1.2	94.0	142.5	0.40	−17.2
679	0.281	9.4	19	1055	0.00426	1.6	1.2	−0.5	−0.4	92.6	148.1	0.40	−17.4
677	0.279	7.7	19	1055	0.00434	0.1	−0.3	−0.5	−0.4	92.9	148.9	0.40	−17.4
680	0.280	5.2	19	1054	0.00436	−2.4	−2.8	−0.5	−0.4	93.3	149.6	0.40	−17.5
682	0.281	3.7	19	1052	0.00435	−3.9	−4.3	−0.5	−0.4	93.6	150.0	0.40	−17.5
681	0.278	−2.6	19	1054	0.00436	−9.9	−10.3	−0.5	−0.4	94.3	150.3	0.39	−17.5

Table 2. Open-Jet Shear-Layer Corrections To Add to Measured Angles and dB Levels

Tunnel velocity, V, m/s	$\Delta\xi_{19}$, deg	$(\Delta dB_{19})_{sl}$	$\Delta\xi_{21}$, deg	$(\Delta dB_{21})_{sl}$
19	1.2	0.0	0.6	0.3
38	2.4	0.1	1.1	0.6
62	4.0	0.3	1.5	1.1

Table 3. Noise Contributions From Individual Sources as Calculated From Scaled Spectra

Run point	Advance ratio, μ	Descent angle, θ, deg	Mic	Load limit F_1, kHz	BVI limit F_2, kHz	BWI limit F_3, kHz	Total PNL, dB	Total dBA, dB	Loading dBA, dB	BVI dBA, dB	BWI dBA, dB	Self dBA, dB	OASPL, dB	Loading SPL, dB	BVI SPL, dB	BWI SPL, dB	Self SPL, dB
659	0.086	−1.2	21	0.25	2.0	7.5	86.8	73.8	56.7	68.9	71.4	62.2	82.6	81.3	75.3	70.9	61.6
660	0.086	−3.8	21	0.25	2.0	8.0	86.3	73.3	55.5	66.3	71.8	62.5	82.4	81.6	71.4	71.1	61.9
661	0.088	−6.1	21	0.25	2.2	8.0	87.7	74.8	54.7	69.6	72.6	63.7	82.2	80.9	73.9	71.8	63.1
662	0.087	−7.8	21	0.25	2.0	8.0	86.3	73.2	53.7	67.0	71.4	62.8	81.1	80.1	71.4	70.7	62.3
669	0.085	−13.8	21	0.25	1.5	7.5	82.7	69.7	45.5	56.5	68.6	62.2	77.3	76.4	63.4	67.9	61.6
670	0.084	−18.8	21	0.25	1.2	6.5	78.8	64.3	41.1	48.2	60.5	61.8	71.6	70.5	58.5	59.9	61.3
671	0.082	−23.9	21	0.25	2.3	4.0	77.2	62.2	41.3	50.7	50.8	61.5	69.8	68.9	57.4	50.1	61.0
638	0.174	5.5	21	0.25	3.0	8.0	94.7	82.3	58.1	82.0	69.6	63.9	89.9	85.3	87.9	68.5	63.7
640	0.175	3.5	21	0.25	2.7	8.0	89.0	76.1	48.3	75.4	67.0	60.8	84.8	81.4	82.1	66.0	60.5
642	0.174	1.9	21	0.25	2.6	8.0	87.3	75.1	48.9	73.9	67.9	61.8	83.5	81.0	79.6	67.0	61.4
646	0.172	−0.7	21	0.25	2.4	7.5	85.8	72.6	45.6	67.2	70.1	64.3	80.7	79.3	73.2	69.2	63.6
649	0.173	−2.1	21	0.25	2.0	8.0	86.3	72.4	49.8	63.3	71.0	64.3	81.8	80.5	74.3	70.1	63.7
652	0.173	−6.7	21	0.25	2.0	7.0	81.4	66.2	49.4	56.9	61.8	63.1	79.5	78.9	69.5	61.0	62.5
653	0.171	−8.2	21	0.25	2.0	7.0	80.8	65.3	49.2	55.8	59.9	62.8	79.1	78.6	68.2	59.1	62.3
656	0.169	−13.4	21	0.25	2.0	5.5	78.0	62.4	46.9	54.6	53.9	60.6	77.6	77.3	64.5	53.6	60.2
657	0.164	−18.6	21	0.25	2.5	4.4	78.5	63.2	45.9	56.0	51.8	61.7	76.4	75.9	64.1	51.3	61.1
679	0.281	9.4	21	0.25	3.5	7.5	91.0	77.7	59.1	77.1	65.7	63.6	92.5	91.9	82.9	64.6	63.6
677	0.279	7.7	21	0.25	3.5	8.0	92.4	80.1	56.5	79.7	68.1	65.0	92.6	91.8	84.8	67.0	65.0
680	0.280	5.2	21	0.25	2.8	7.5	94.7	82.2	57.8	81.0	75.0	70.1	96.0	95.5	85.7	74.0	69.5
682	0.281	3.7	21	0.25	2.5	8.0	93.5	80.0	56.2	77.1	75.7	70.6	95.9	95.6	82.8	74.7	70.1
681	0.278	−2.6	21	0.25	1.7	5.5	86.4	71.0	56.0	65.8	66.1	66.4	94.4	94.3	78.3	66.3	66.1

Table 3. Concluded

Run point	Advance ratio, μ	Descent angle, θ, deg	Mic	Load limit F_1, kHz	BVI limit F_2, kHz	BWI limit F_3, kHz	Total PNL, dB	Total dBA, dB	Loading dBA, dB	BVI dBA, dB	BWI dBA, dB	Self dBA, dB	OASPL, dB	Loading SPL, dB	BVI SPL, dB	BWI SPL, dB	Self SPL, dB
659	0.086	−1.2	19	0.25	1.1	7.4	85.0	73.4	51.2	61.7	72.7	62.1	79.8	78.0	69.7	73.2	61.6
660	0.086	−3.8	19	0.25	1.2	7.7	85.0	73.2	49.5	61.7	72.4	62.2	78.8	76.7	70.2	72.6	61.8
661	0.088	−6.1	19	0.25	1.6	7.8	85.8	74.2	47.9	66.1	73.1	62.9	78.2	75.1	70.9	72.8	62.4
662	0.087	−7.8	19	0.25	1.4	7.5	85.2	73.6	46.2	63.2	72.7	63.2	77.7	74.9	69.1	72.6	62.7
669	0.085	−13.8	19	0.25	1.1	7.5	81.9	69.6	36.7	52.5	68.6	62.2	74.4	72.4	62.5	68.4	61.6
670	0.084	−18.8	19	0.25	1.1	6.5	78.8	64.7	37.3	48.5	61.0	62.1	69.8	67.8	60.6	60.4	61.5
671	0.082	−23.9	19	0.25	1.5	4.5	77.7	62.9	37.0	48.8	53.6	62.1	68.3	66.4	59.4	53.4	61.5
638	0.174	5.5	19	0.25	3.0	8.0	95.8	82.6	52.4	82.2	70.9	65.5	90.2	80.6	89.6	70.0	65.2
640	0.175	3.5	19	0.25	2.0	7.6	89.5	76.8	50.0	75.8	68.9	62.2	84.6	78.9	83.1	68.7	61.7
642	0.174	1.9	19	0.25	2.5	8.0	86.0	73.1	50.4	70.8	68.2	62.0	81.4	78.5	77.8	67.4	61.6
646	0.172	−0.7	19	0.25	1.5	7.5	85.2	72.3	47.6	63.6	71.0	63.3	78.6	76.4	71.8	70.7	62.8
649	0.173	−2.1	19	0.25	0.9	7.5	85.3	72.5	46.5	57.0	71.8	63.5	79.7	78.3	69.5	71.7	62.9
652	0.173	−6.7	19	0.25	1.2	7.0	81.4	67.0	43.5	54.9	64.5	62.7	75.9	75.0	65.3	63.8	62.2
653	0.171	−8.2	19	0.25	1.3	7.5	81.1	66.4	43.1	54.6	63.7	62.5	75.5	74.6	64.8	62.8	62.1
656	0.169	−13.4	19	0.25	2.0	5.5	78.8	63.4	43.9	54.8	55.0	61.9	74.9	74.3	63.9	54.1	61.5
657	0.164	−18.6	19	0.25	2.2	4.5	78.9	63.6	43.8	55.2	54.8	62.2	73.5	72.6	63.5	53.9	61.6
679	0.281	9.4	19	0.25	3.7	8.0	92.1	79.4	57.4	79.0	66.7	64.5	87.8	84.5	85.0	65.5	64.4
677	0.279	7.7	19	0.25	3.5	7.8	93.4	81.0	54.9	80.6	68.2	65.4	88.4	83.9	86.4	67.1	65.2
680	0.280	5.2	19	0.25	2.3	7.5	93.0	79.8	57.8	77.4	75.1	68.0	91.2	90.0	84.4	74.1	67.6
682	0.281	3.7	19	0.25	2.5	8.0	92.0	78.2	55.8	74.3	75.2	67.4	90.9	90.3	80.6	74.2	67.3
681	0.278	−2.6	19	0.25	1.7	5.6	86.6	70.8	59.0	65.9	64.9	66.3	90.2	90.0	74.9	64.3	66.0

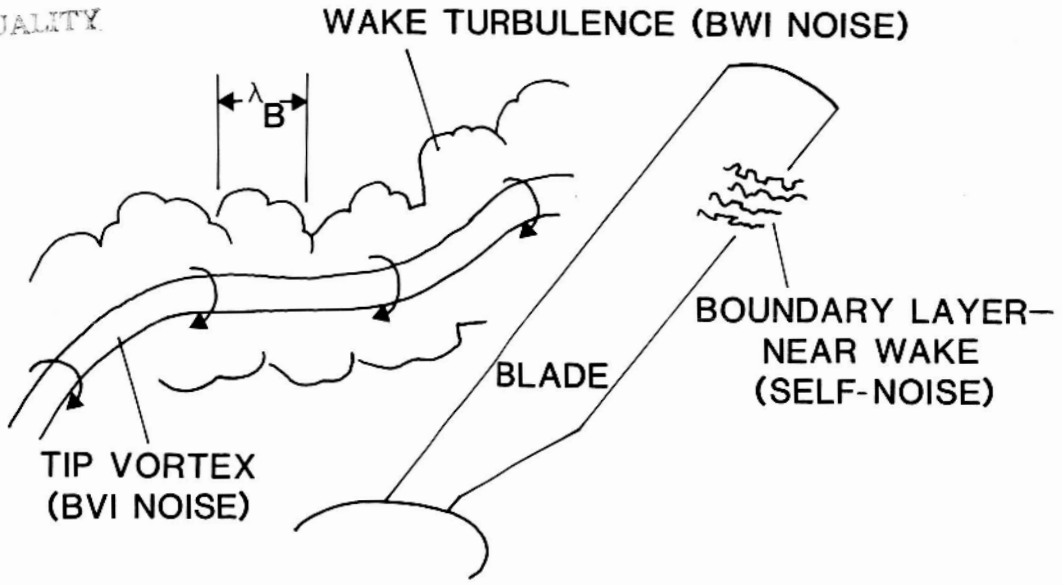

Figure 1. Flow field encountered by blade.

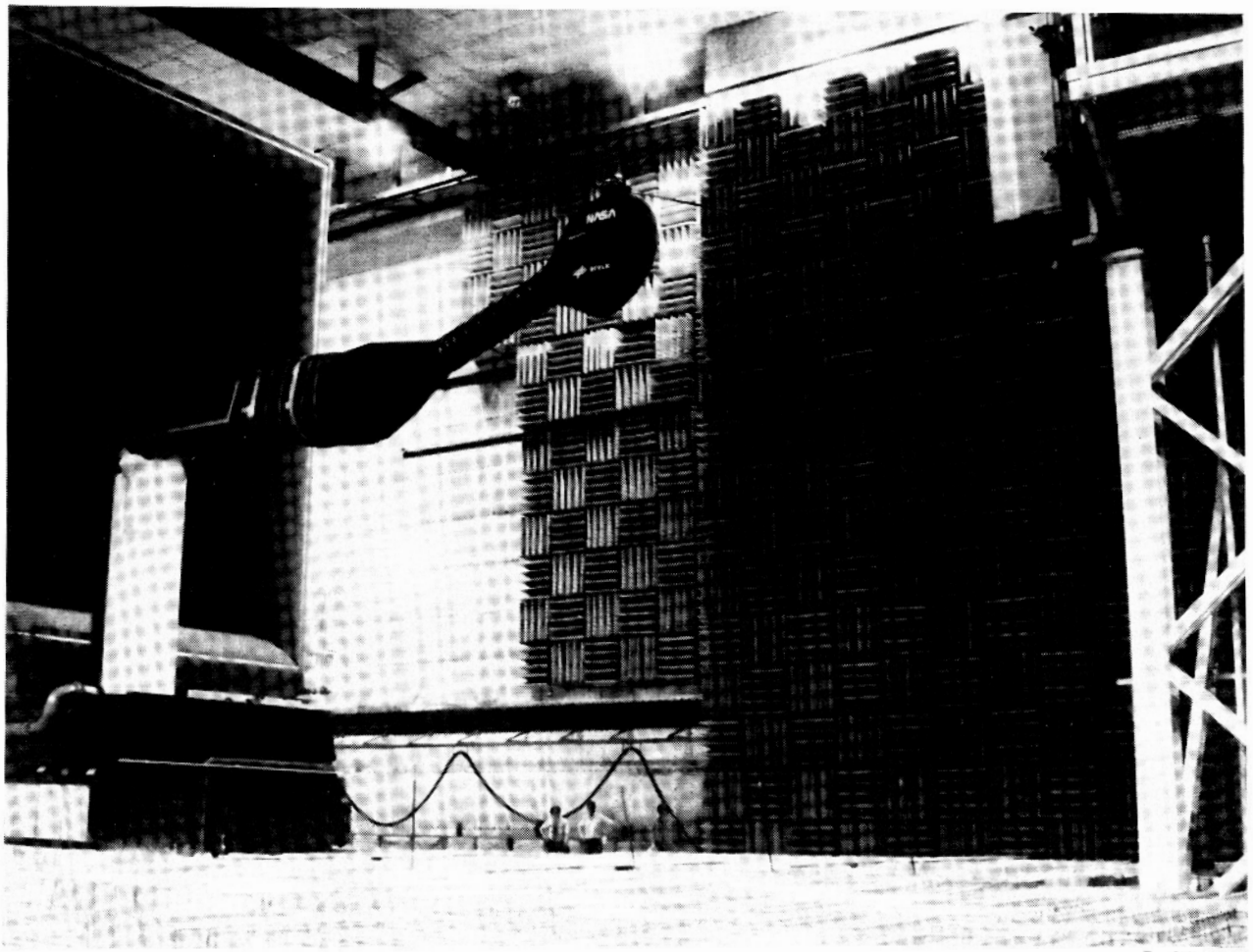

L-88-100

Figure 2. Overview of test setup.

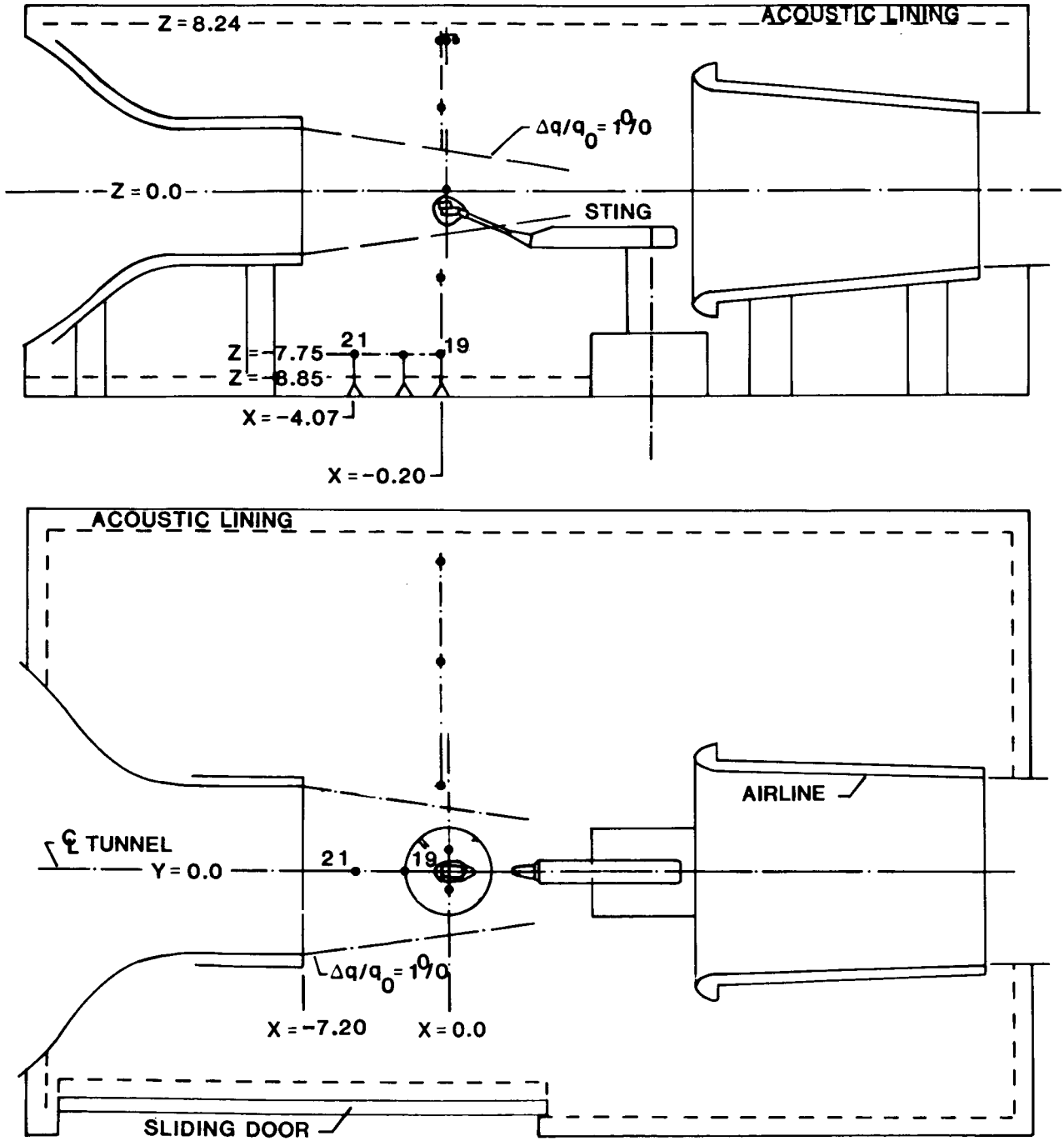

Figure 3. Detail of test setup.

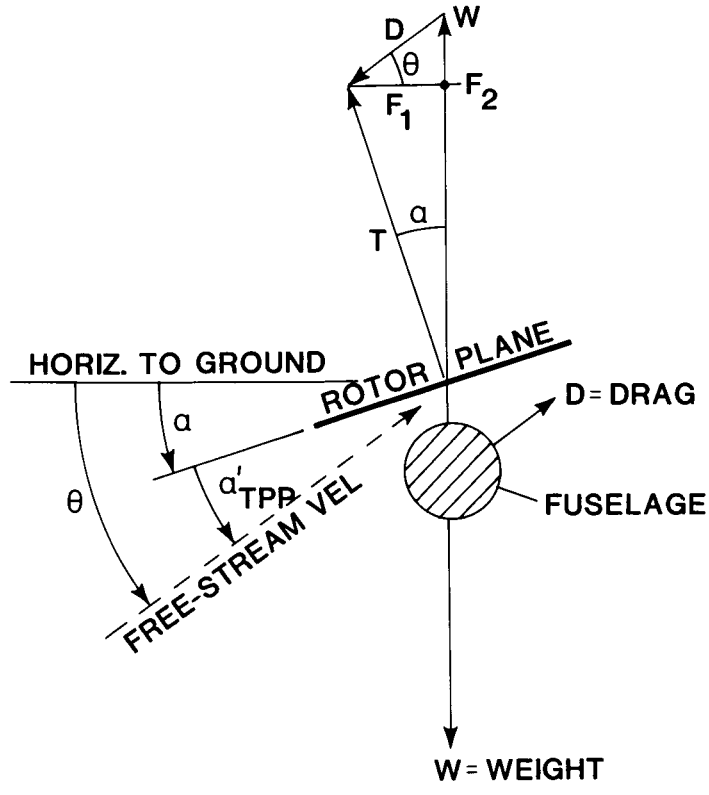

Figure 4. Force balance to relate α'_{TPP}, μ, and descent angle θ. Descent condition is shown; angles shown are positive.

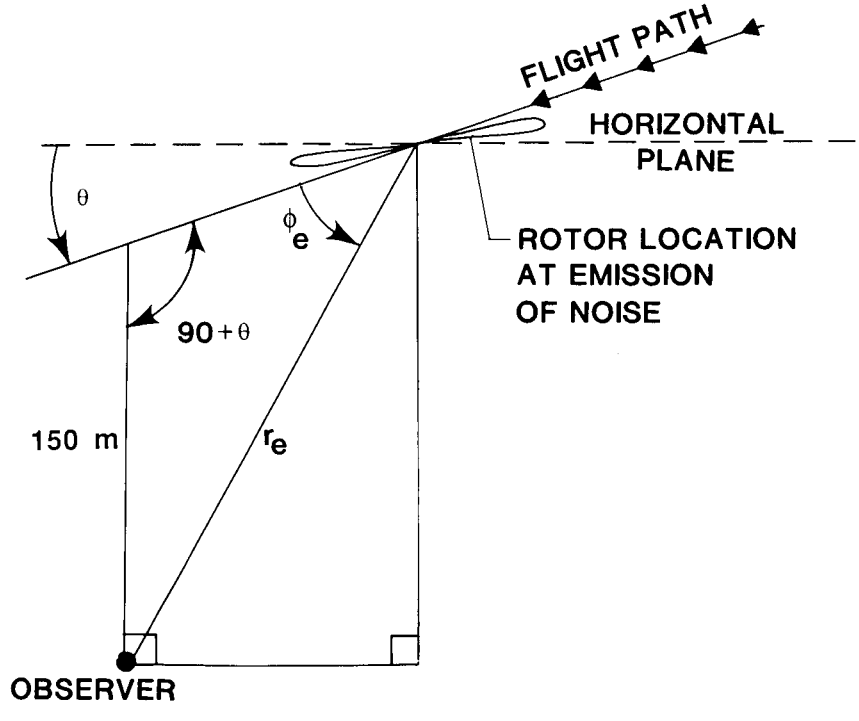

Figure 5. Geometry of flyover to which scaling is required to match.

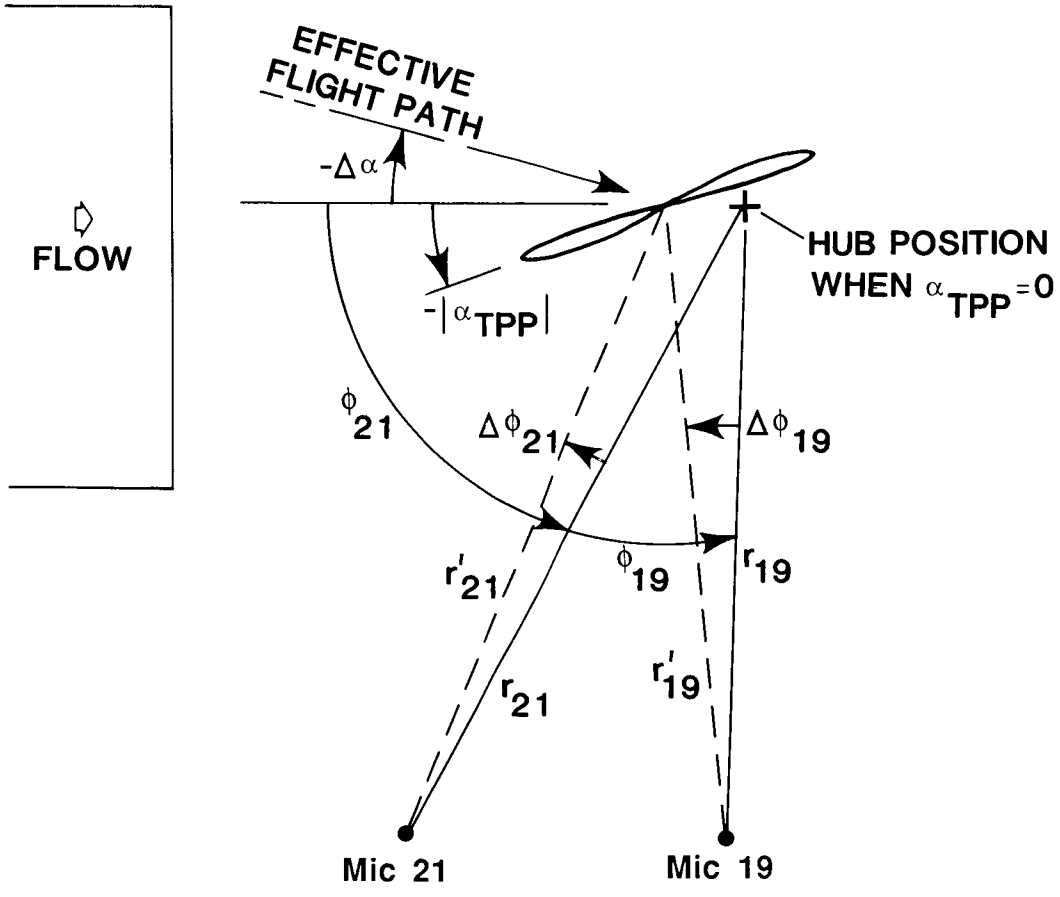

Figure 6. Geometric arrangement of DNW rotor with respect to microphone positions.

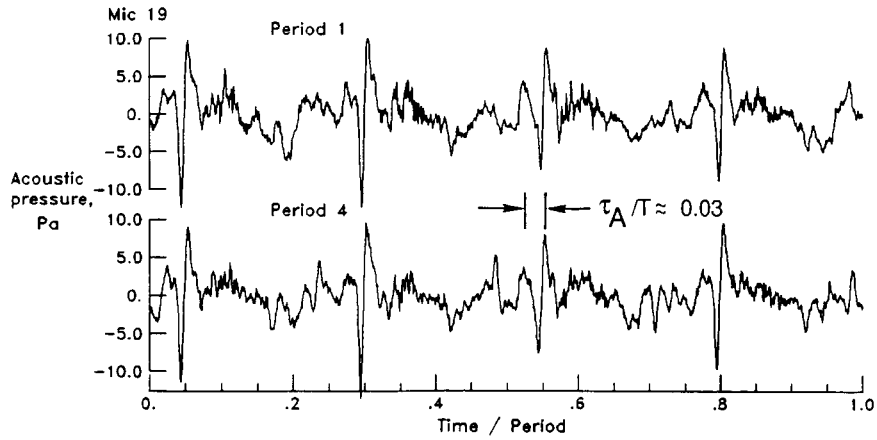

(a) $\alpha_{TPP} = 1.6°$; $\alpha'_{TPP} = 0.4°$; $\mu = 0.175$; $\theta = 3.5°$. Run point 640.

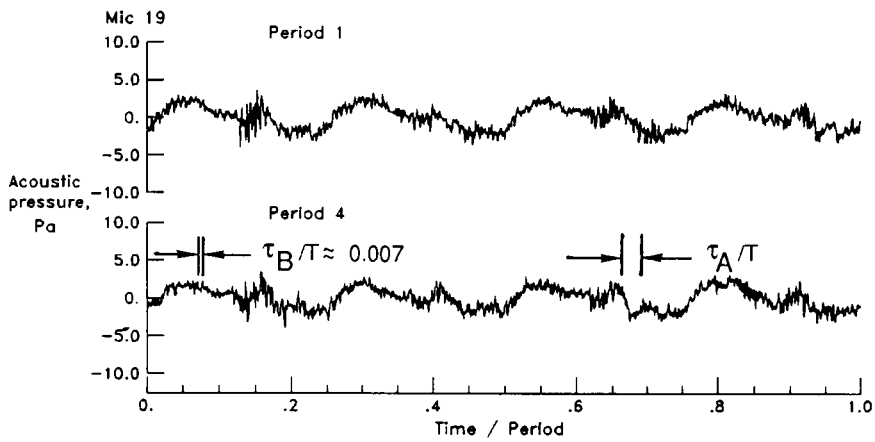

(b) $\alpha_{TPP} = -3.9°$; $\alpha'_{TPP} = -5.1°$; $\mu = 0.173$; $\theta = -2.1°$. Run point 649.

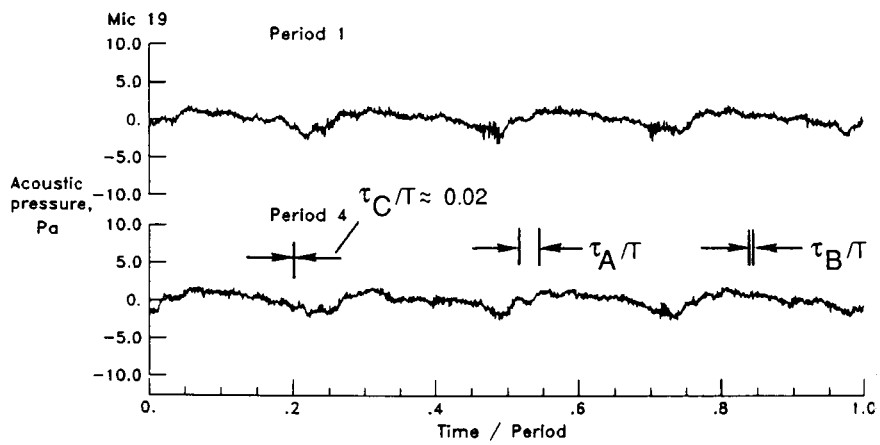

(c) $\alpha_{TPP} = -9.9°$; $\alpha'_{TPP} = -11.1°$; $\mu = 0.171$; $\theta = -8.2°$. Run point 653.

Figure 7. Microphone 19 signal time histories showing effect of varying rotor angle α_{TPP} for constant $C_T \approx 0.0044$ and $\mu \approx 0.173$ ($V = 38$ m/s) at rotor speed of 1050 rpm.

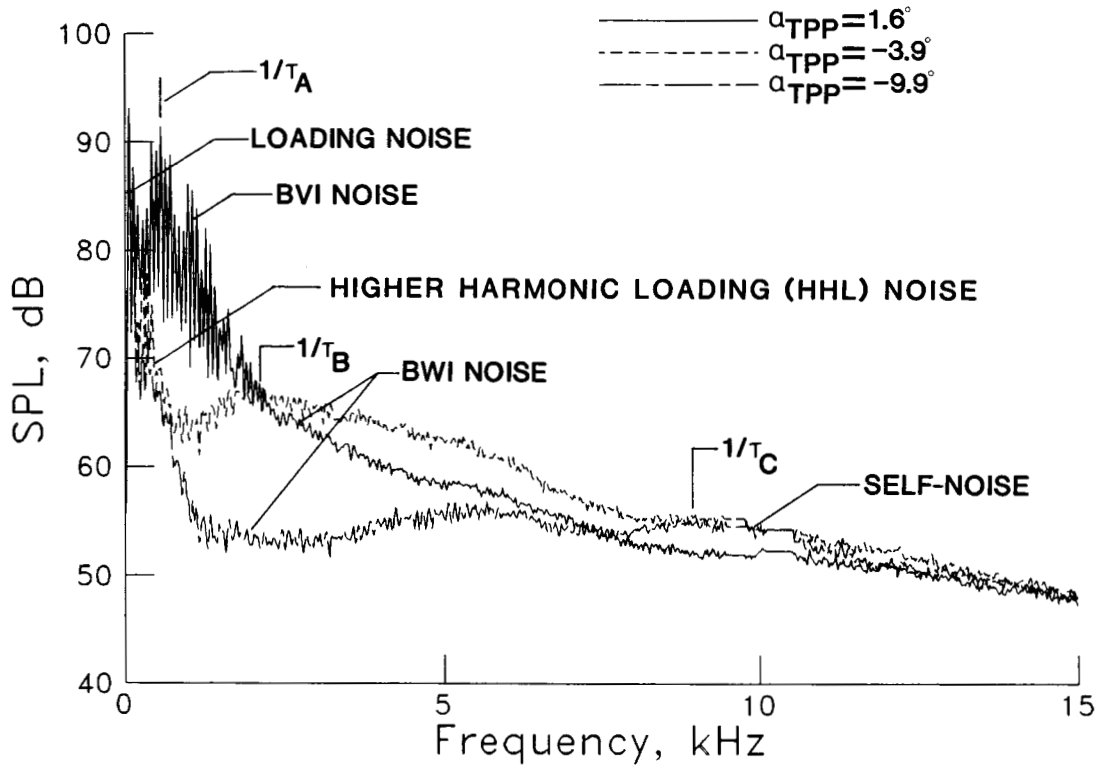

Figure 8. Narrowband noise spectra for cases of figure 7. Reference frequencies: $1/\tau_A$ = 580 Hz, $1/\tau_B$ = 2.5 kHz, and $1/\tau_C$ = 8.75 kHz. Bandwidth is $f_{bp}/4$ or 17.5 Hz.

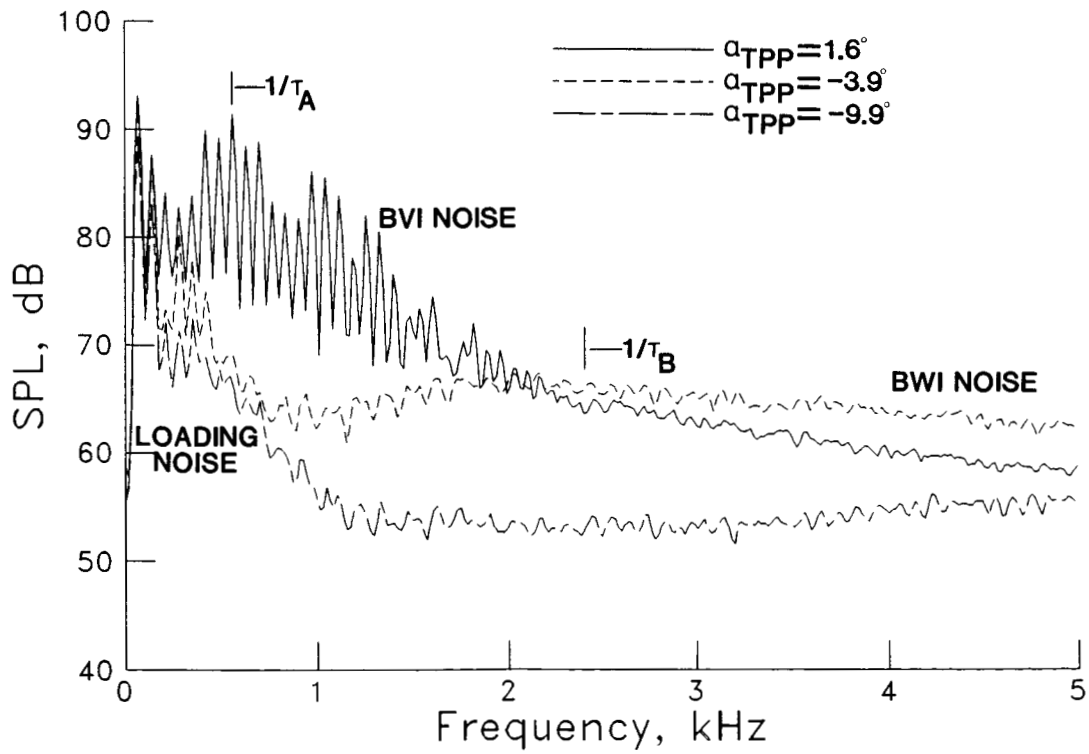

Figure 9. Narrowband noise spectra with expanded frequency scale for cases of figures 7 and 8.

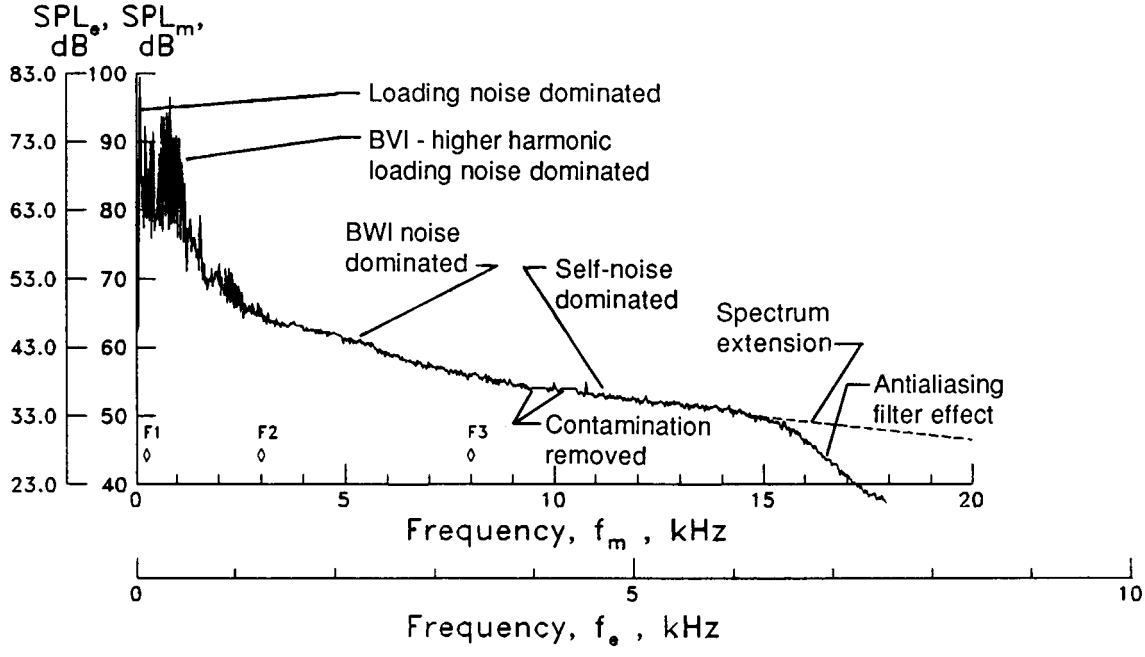

Figure 10. Noise spectrum from microphone 21 for $\alpha_{\mathrm{TPP}} = 3.6°$ and $\mu = 0.174$ (run point 638) with equivalent flyover-observer scaling. Bandwidths $\Delta f_m = 17.5$ and $\Delta f_e = 7.35$ Hz.

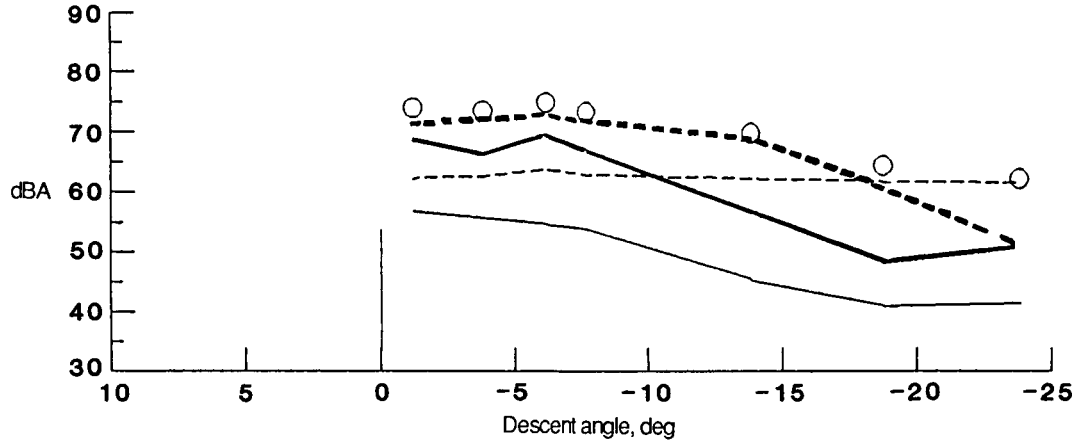

(a) Advance ratio = 0.086.

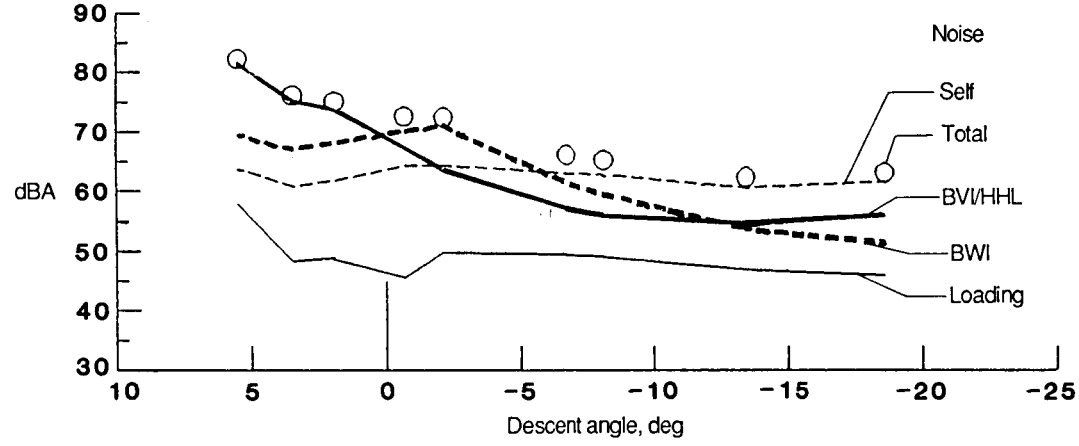

(b) Advance ratio = 0.172.

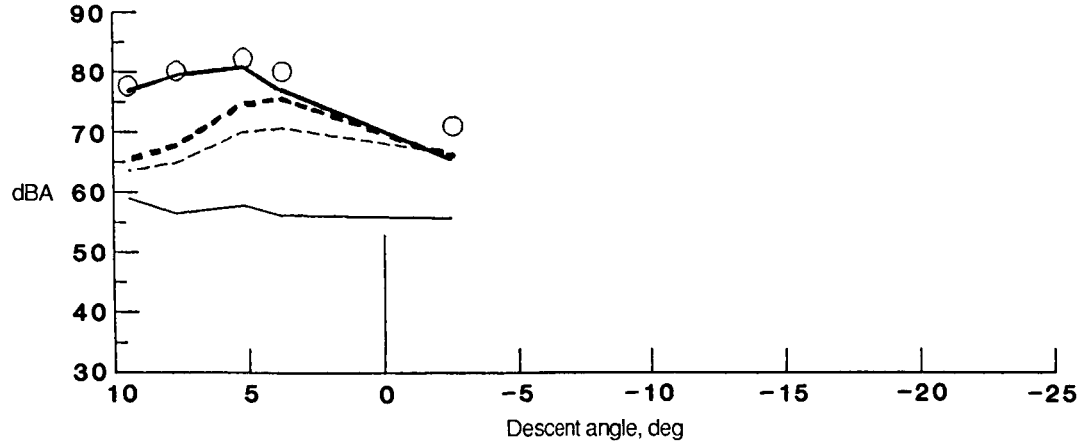

(c) Advance ratio = 0.280.

Figure 11. Contributions from different noise sources to calculation of dBA for observer at $r_e \approx 163$ m and $\phi_e \approx 65°$ to "full-scale" flight paths. Data from microphone 21; no ground effect added.

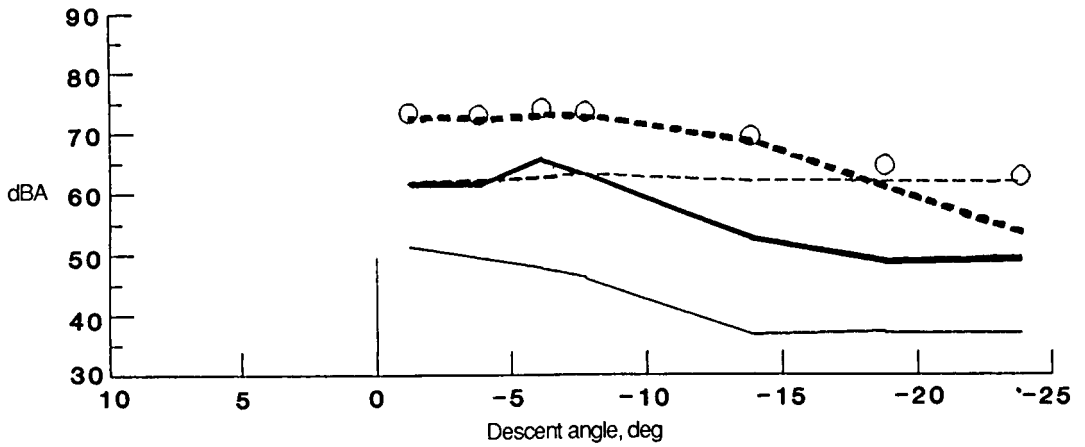

(a) Advance ratio = 0.086.

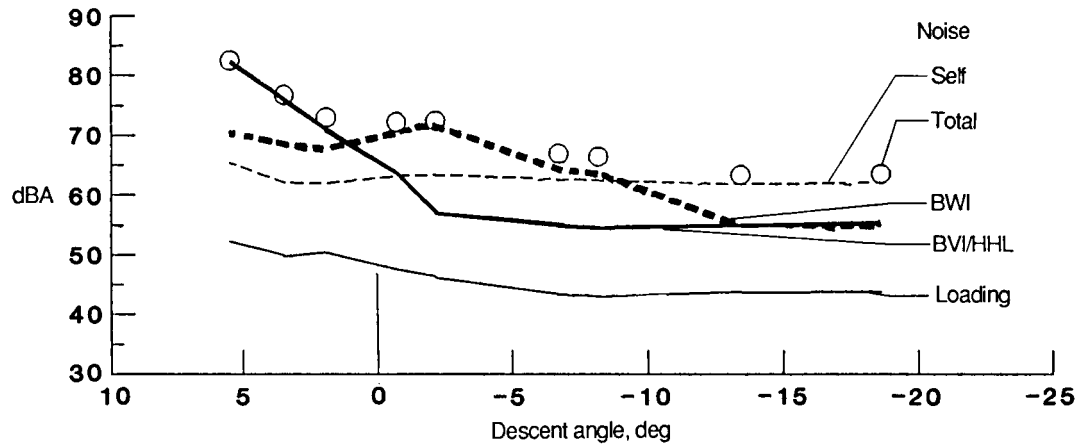

(b) Advance ratio = 0.172.

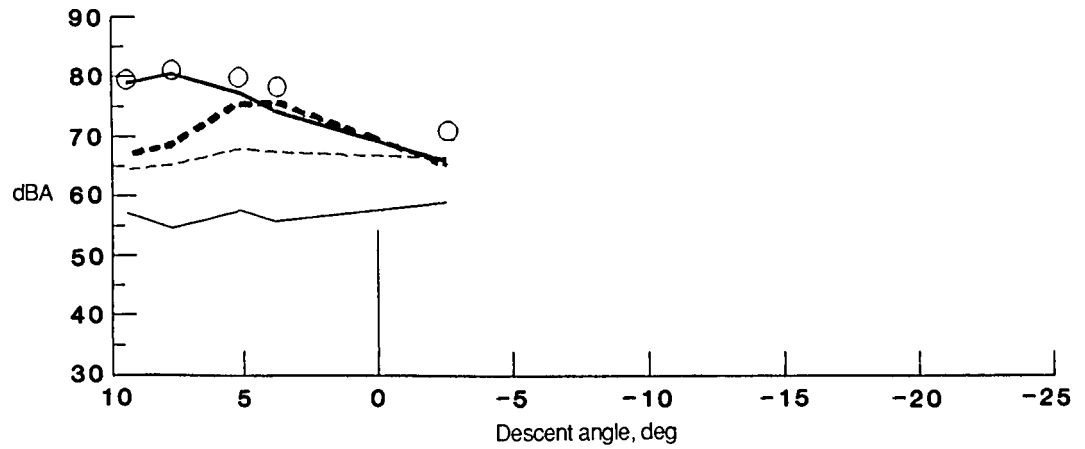

(c) Advance ratio = 0.280.

Figure 12. Contributions from different noise sources to calculation of dBA for observer at $r_e \approx 148$ m and $\phi_e \approx 94°$ to "full-scale" flight paths. Data from microphone 19; no ground effect added.

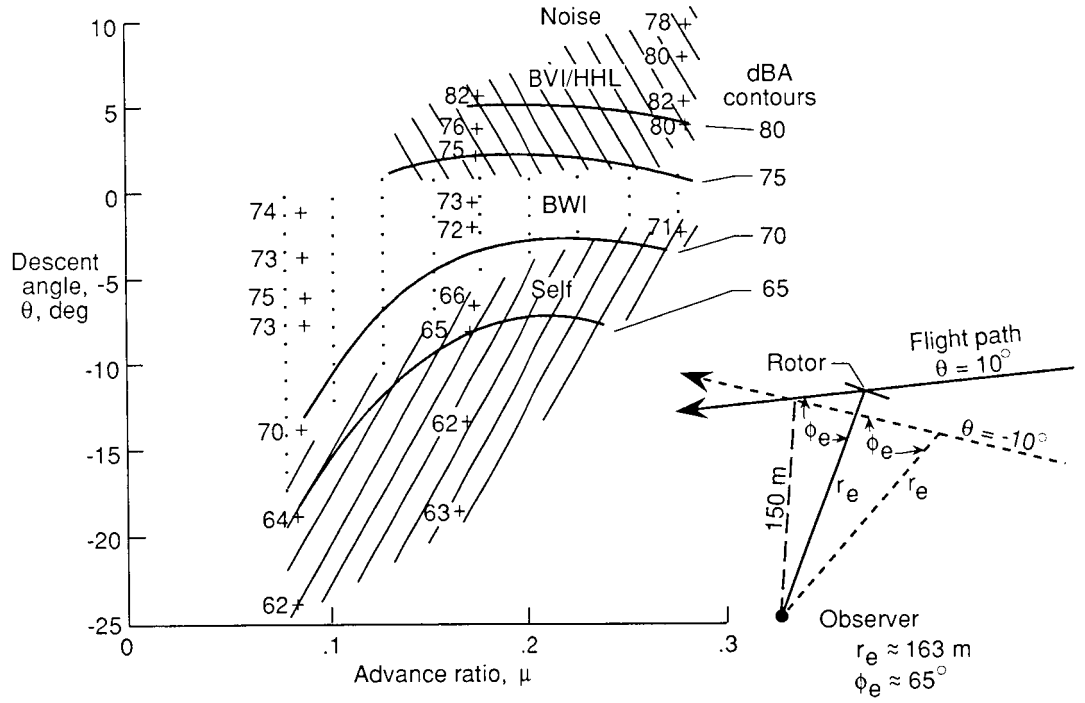

(a) dBA.

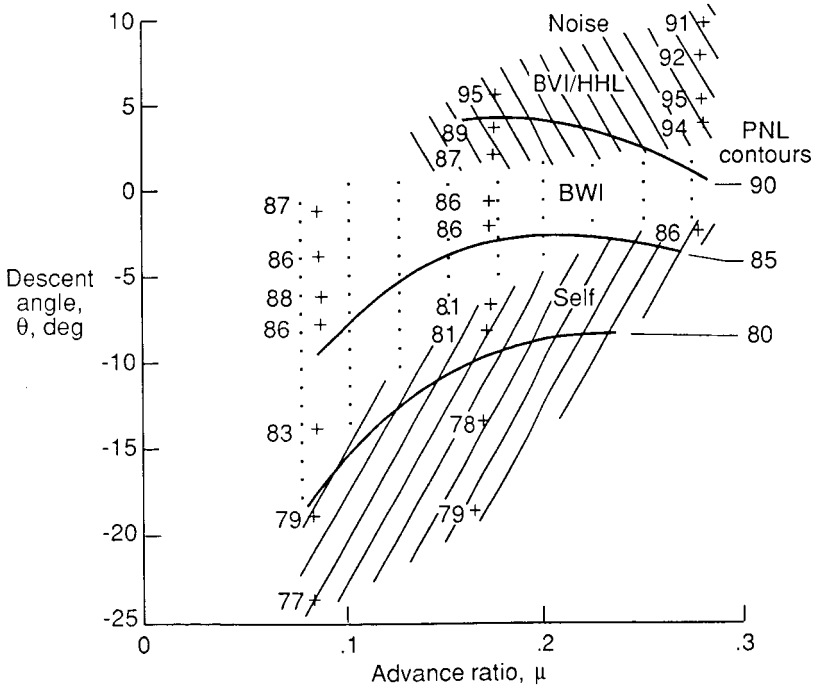

(b) PNL.

Figure 13. Values of dBA and PNL for different operating conditions for observer at $r_e \approx 163$ m and $\phi_e \approx 65°$. Hatched regions indicate source dominance in their calculation; data from microphone 21; no ground effect added.

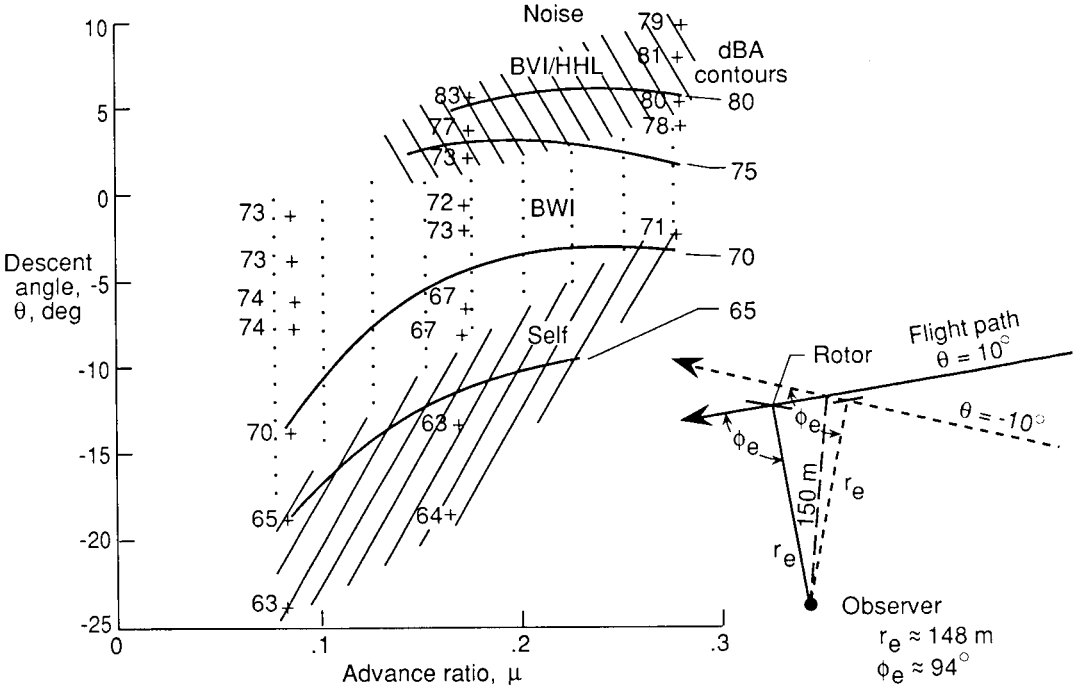

(a) dBA.

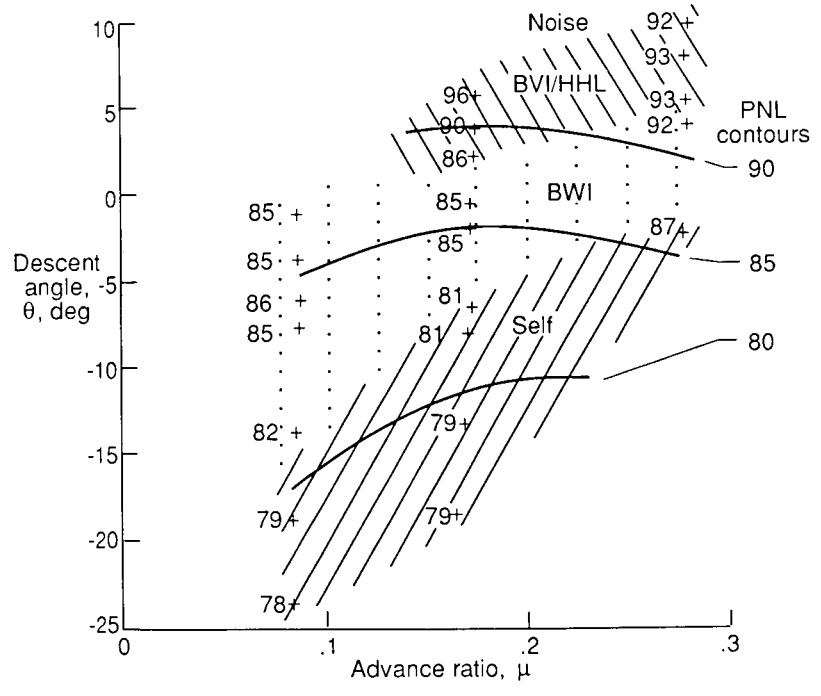

(b) PNL.

Figure 14. Values of dBA and PNL for different operating conditions for observer at $r_e \approx 148$ m and $\phi_e \approx 94°$. Hatched regions indicate source dominance in their calculation; data from microphone 19; no ground effect added.

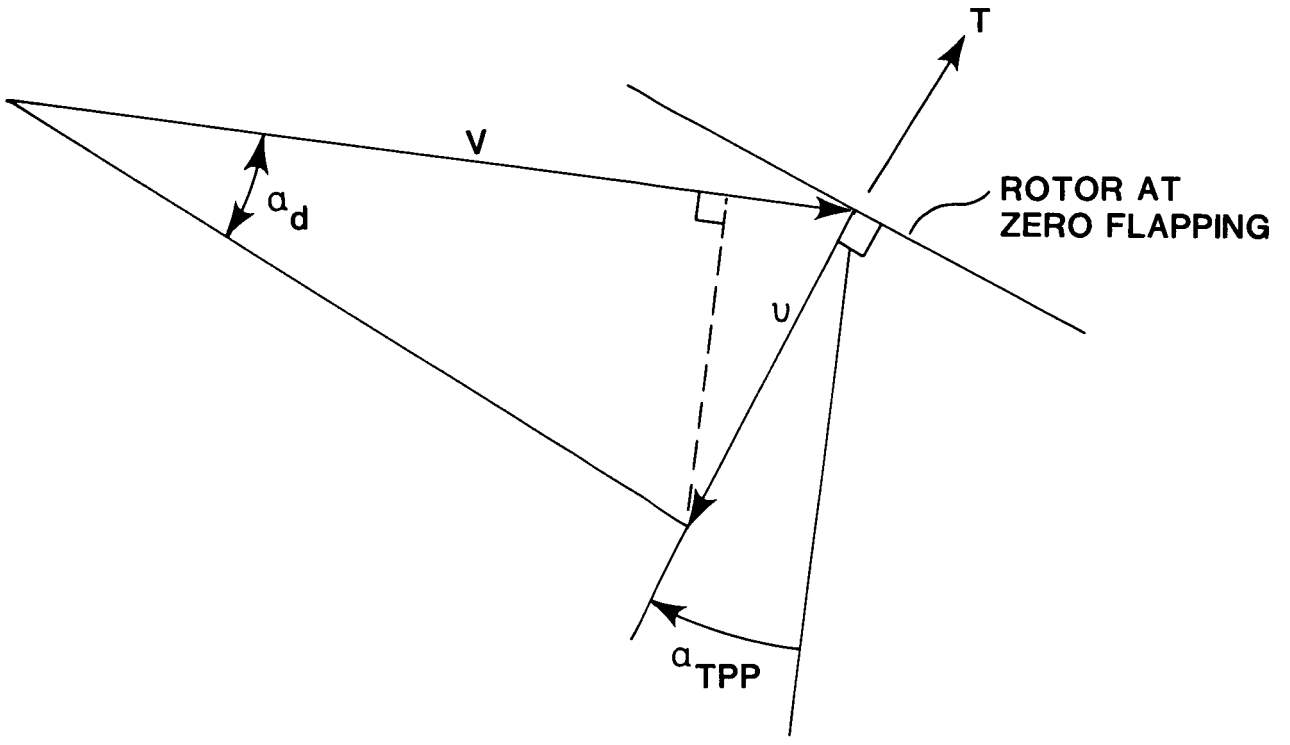

Figure 15. Illustration of velocity vectors at rotor.

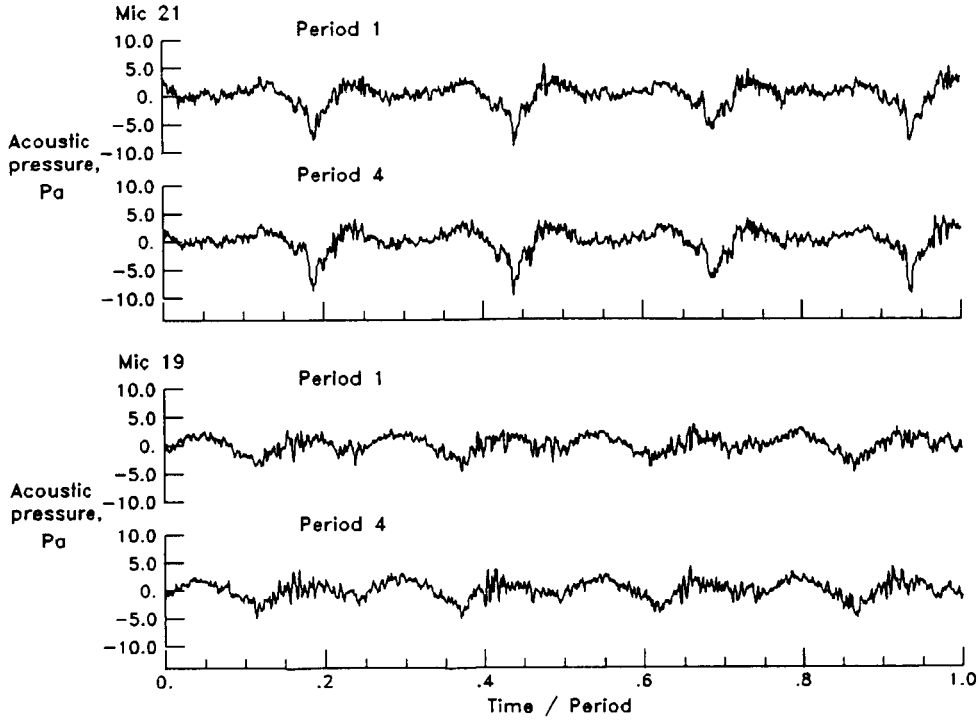

(a) $\alpha_{\mathrm{TPP}} = 2.7°$; $\alpha'_{\mathrm{TPP}} = -2.0°$; $\mu = 0.086$; $\theta = -1.2°$. Run point 659.

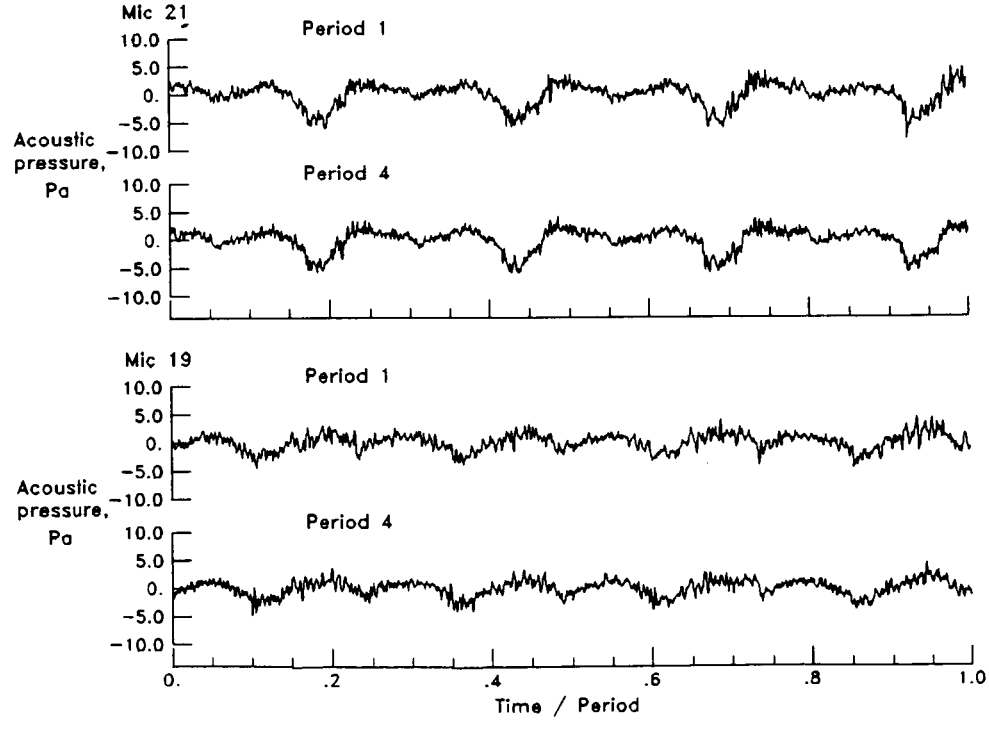

(b) $\alpha_{\mathrm{TPP}} = 0.1°$; $\alpha'_{\mathrm{TPP}} = -4.5.°$; $\mu = 0.086$; $\theta = -3.8°$. Run point 660.

Figure 16. Microphone signal time histories showing effect of varying rotor angle for different advance ratios.

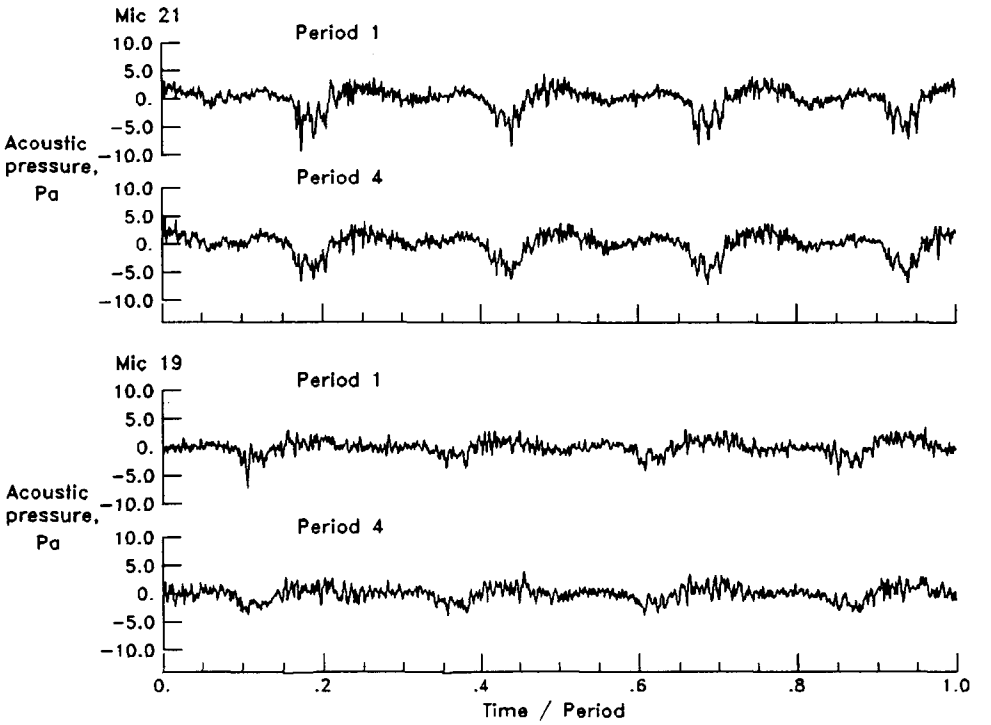

(c) $\alpha_{\mathrm{TPP}} = -2.4°$; $\alpha'_{\mathrm{TPP}} = -6.9°$; $\mu = 0.088$; $\theta = -6.1°$. Run point 661.

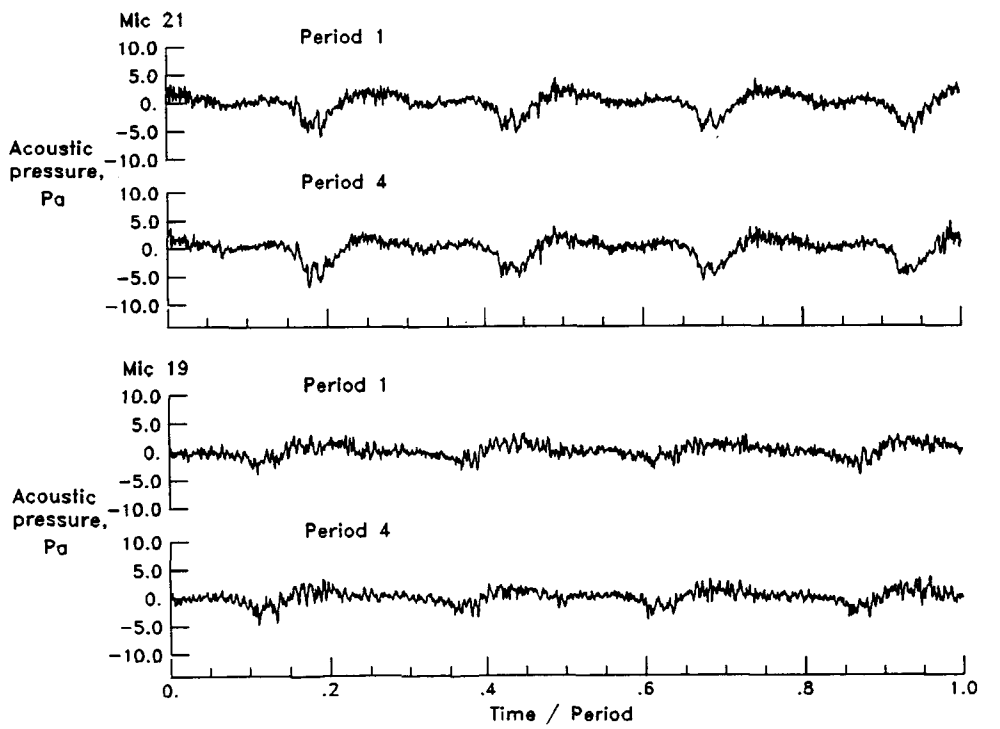

(d) $\alpha_{\mathrm{TPP}} = -3.9°$; $\alpha'_{\mathrm{TPP}} = -8.5°$; $\mu = 0.087$; $\theta = -7.8°$. Run point 662.

Figure 16. Continued.

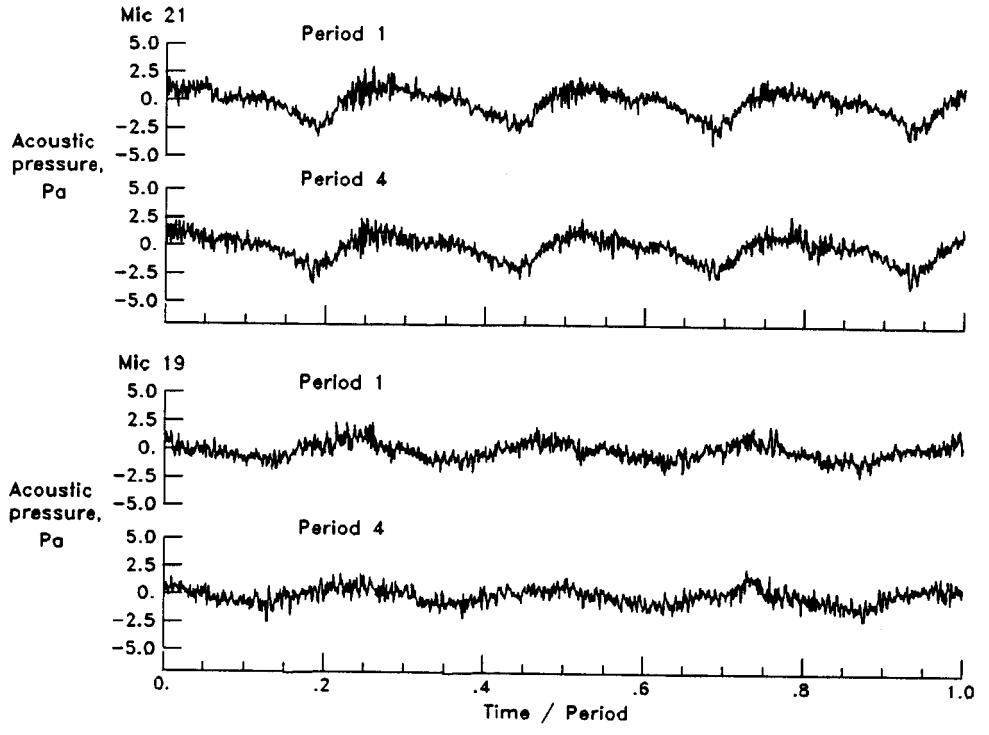

(e) $\alpha_{\mathrm{TPP}} = -9.9°$; $\alpha'_{\mathrm{TPP}} = -14.6°$; $\mu = 0.085$; $\theta = -13.8°$. Run point 669.

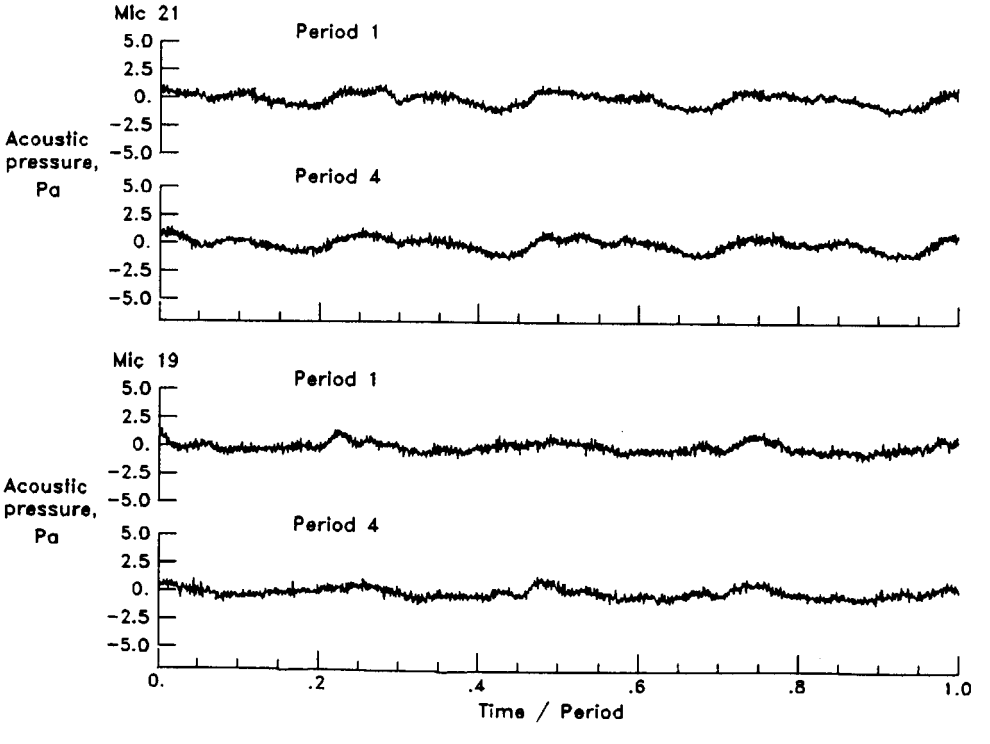

(f) $\alpha_{\mathrm{TPP}} = -14.9°$; $\alpha'_{\mathrm{TPP}} = -19.5°$; $\mu = 0.084$; $\theta = -18.8°$. Run point 670.

Figure 16. Continued.

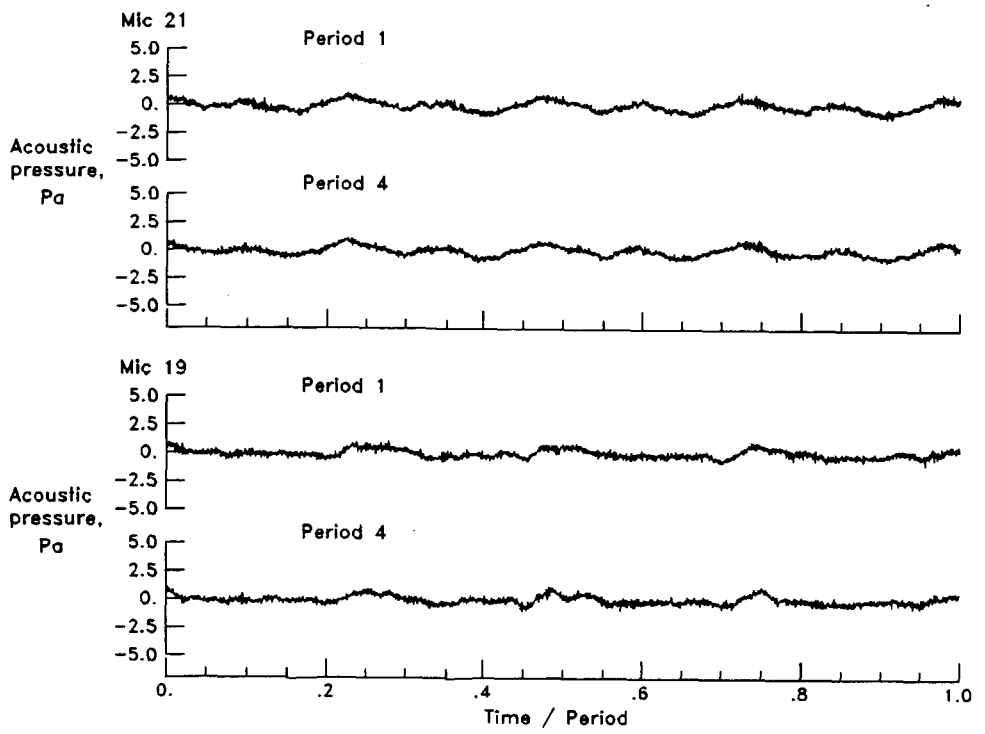

(g) $\alpha_{\mathrm{TPP}} = -19.9°$; $\alpha'_{\mathrm{TPP}} = -24.5°$; $\mu = 0.082$; $\theta = -23.9°$. Run point 671.

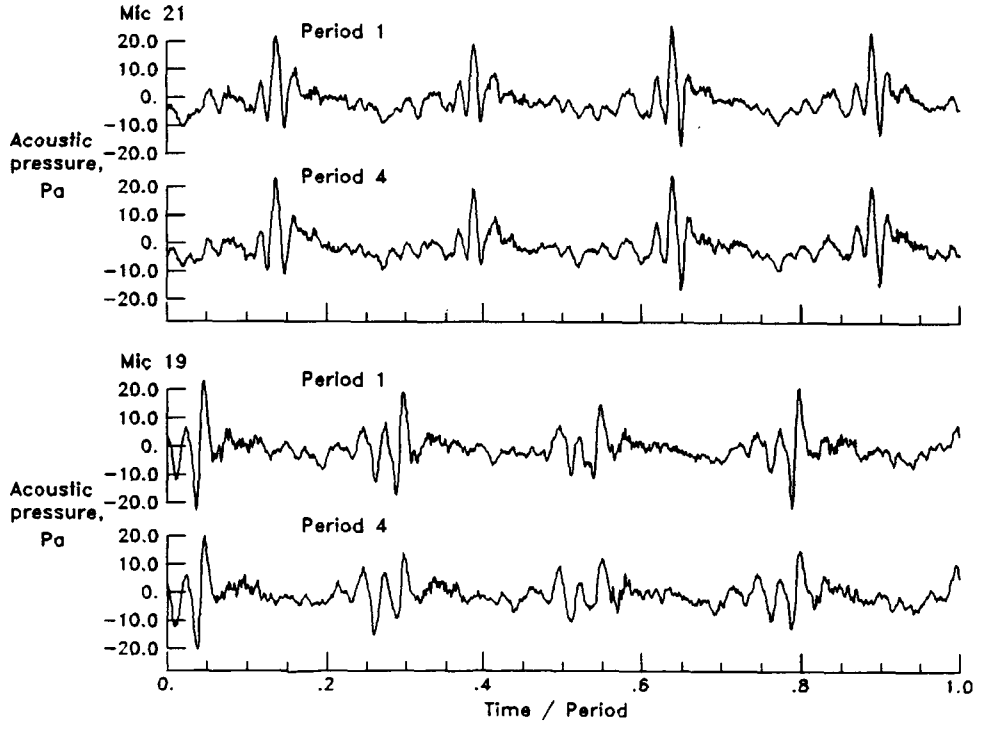

(h) $\alpha_{\mathrm{TPP}} = 3.6°$; $\alpha'_{\mathrm{TPP}} = 2.4°$; $\mu = 0.174$; $\theta = 5.5°$. Run point 638.

Figure 16. Continued.

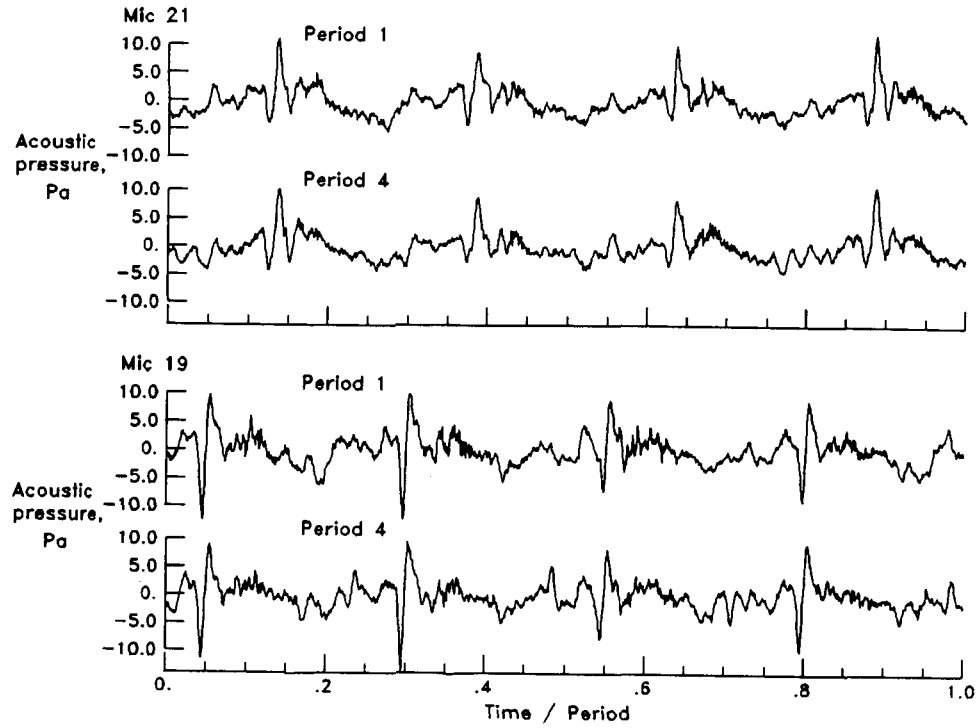

(i) $\alpha_{\mathrm{TPP}} = 1.6°$; $\alpha'_{\mathrm{TPP}} = 0.4°$; $\mu = 0.175$; $\theta = 3.5°$. Run point 640.

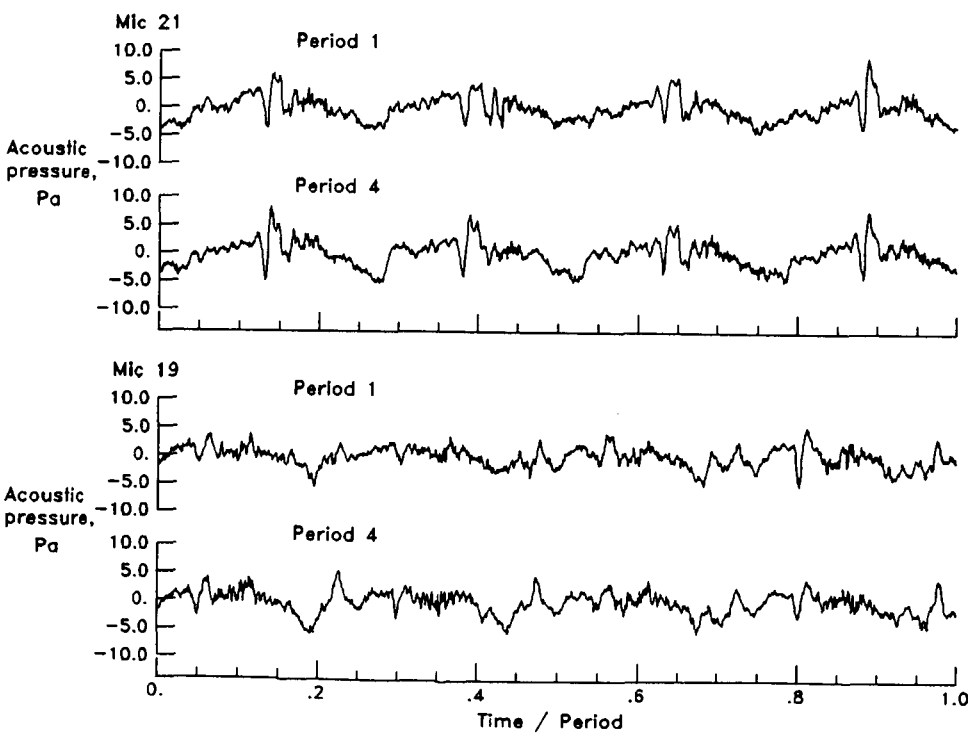

(j) $\alpha_{\mathrm{TPP}} = 0.1°$; $\alpha'_{\mathrm{TPP}} = -1.1°$; $\mu = 0.174$; $\theta = 1.9°$. Run point 642.

Figure 16. Continued.

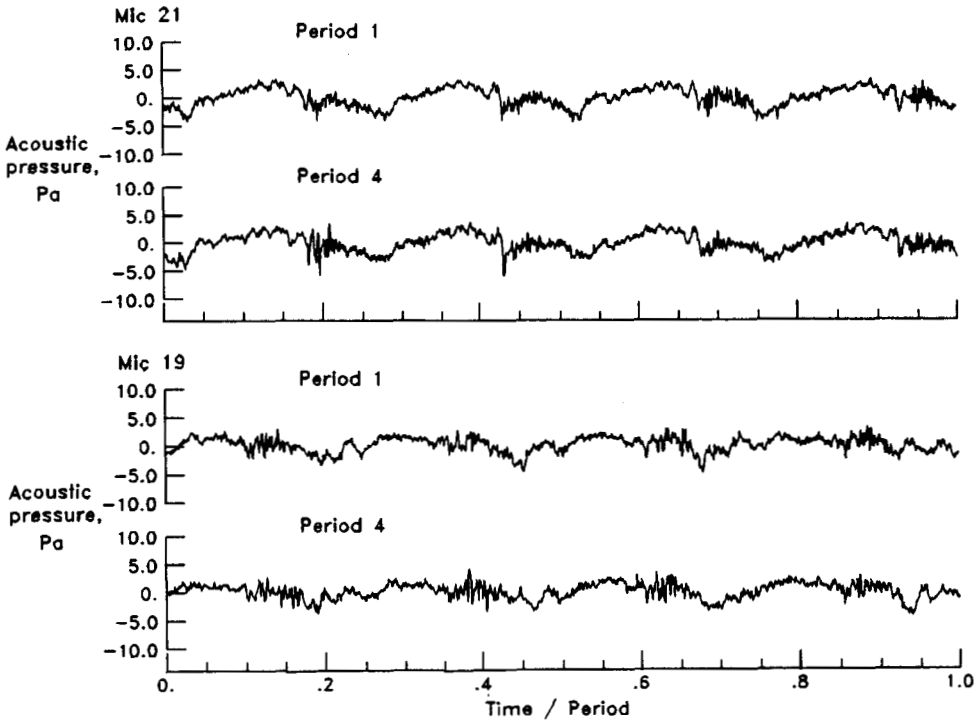

(k) $\alpha_{\mathrm{TPP}} = -2.4°$; $\alpha'_{\mathrm{TPP}} = -3.6°$; $\mu = 0.172$; $\theta = -0.7°$. Run point 646.

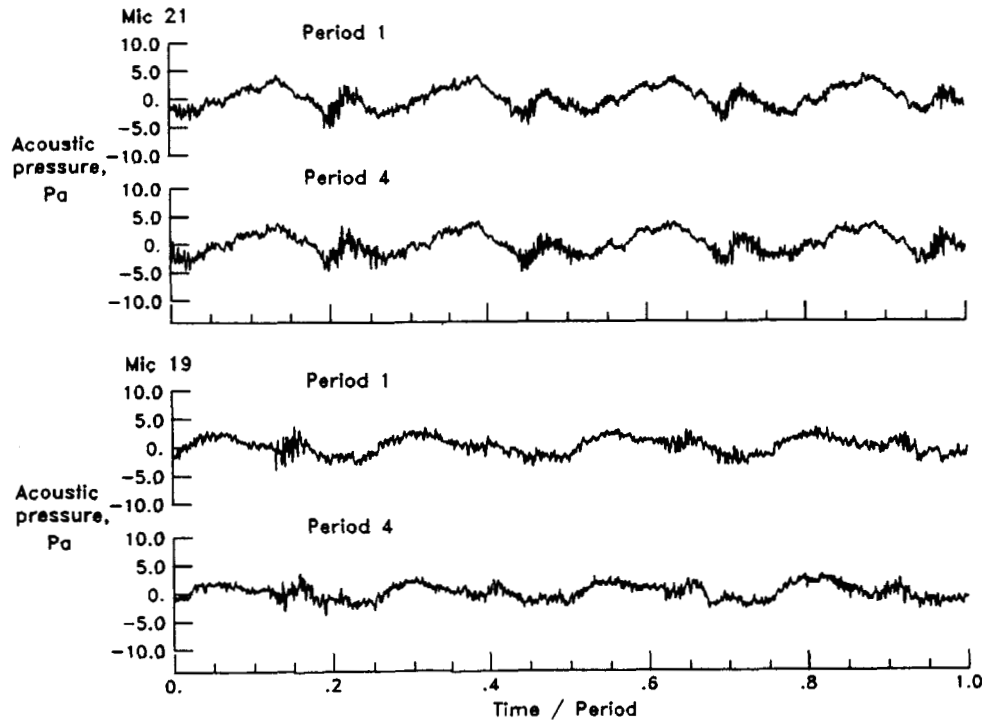

(l) $\alpha_{\mathrm{TPP}} = -3.9°$; $\alpha'_{\mathrm{TPP}} = -5.1°$; $\mu = 0.173$; $\theta = -2.1°$. Run point 649.

Figure 16. Continued.

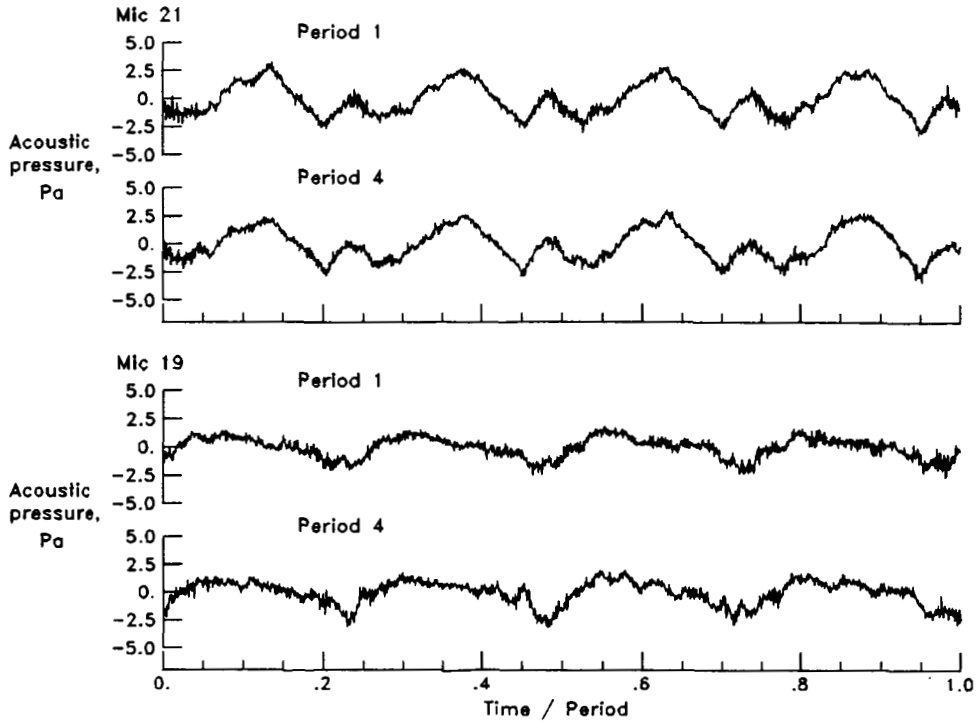

(m) $\alpha_{\mathrm{TPP}} = -8.4°$; $\alpha'_{\mathrm{TPP}} = -9.6°$; $\mu = 0.173$; $\theta = -6.7°$. Run point 652.

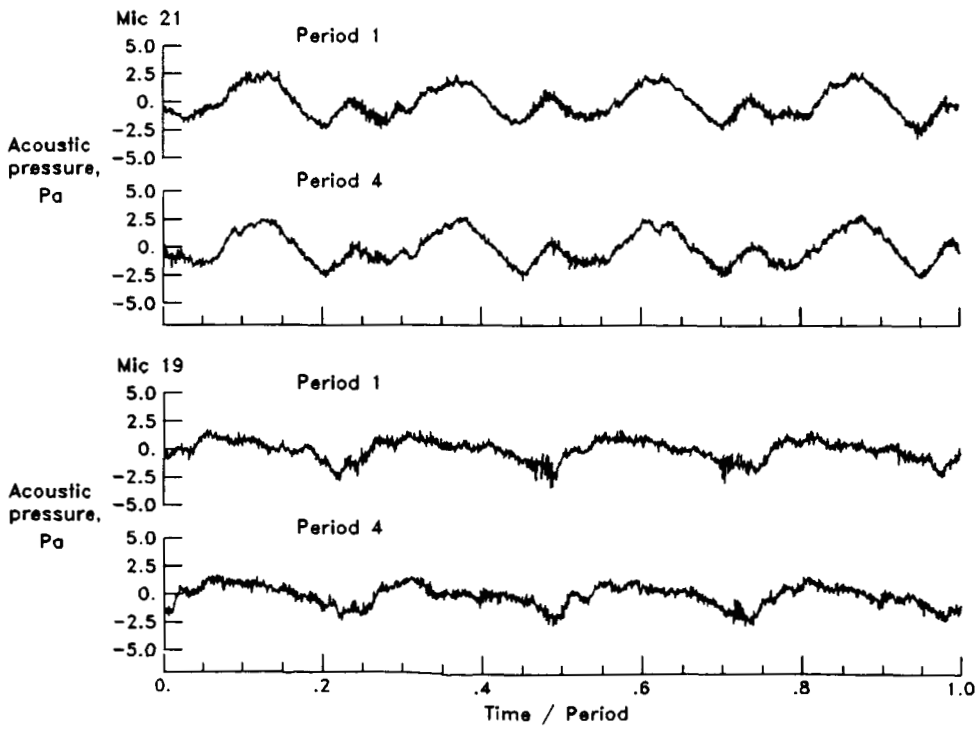

(n) $\alpha_{\mathrm{TPP}} = -9.9°$; $\alpha'_{\mathrm{TPP}} = -11.1°$; $\mu = 0.171$; $\theta = -8.2°$. Run point 653.

Figure 16. Continued.

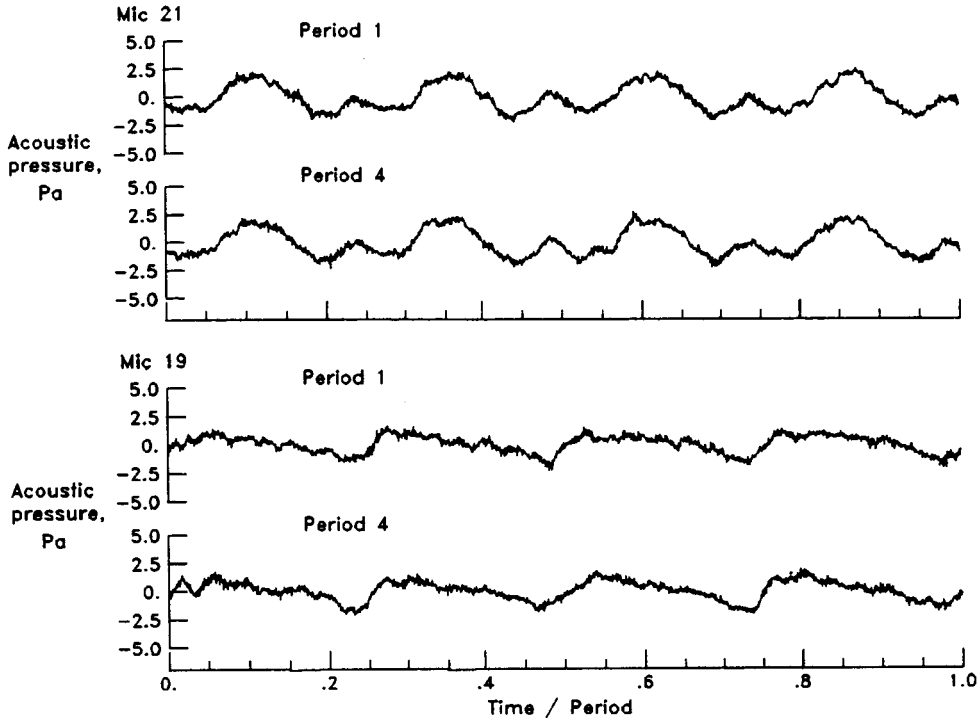

(o) $\alpha_{\mathrm{TPP}} = -14.9°$; $\alpha'_{\mathrm{TPP}} = -16.1°$; $\mu = 0.169$; $\theta = -13.4°$. Run point 656.

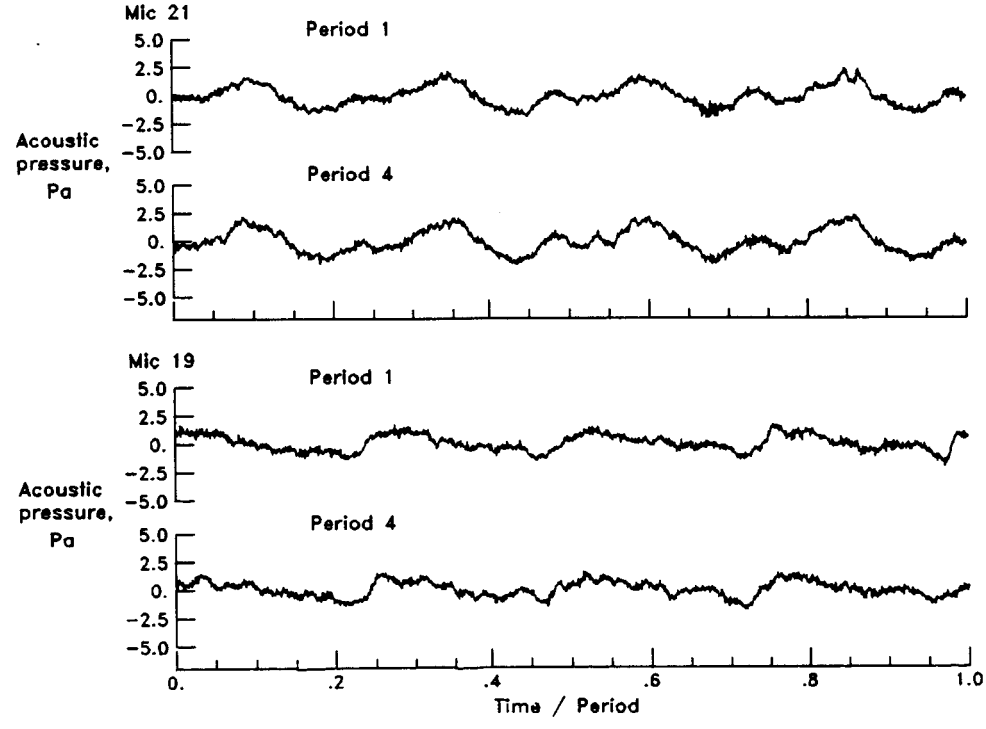

(p) $\alpha_{\mathrm{TPP}} = -19.8°$; $\alpha'_{\mathrm{TPP}} = -21.1°$; $\mu = 0.164$; $\theta = -18.6°$. Run point 657.

Figure 16. Continued.

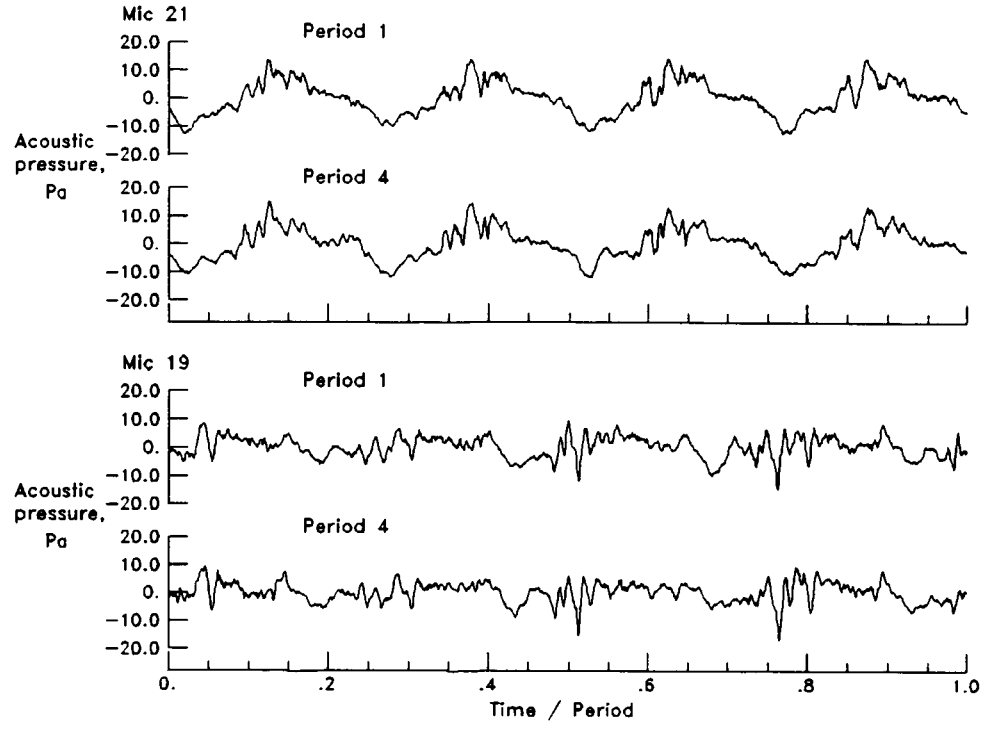

(q) $\alpha_{TPP} = 1.6°$; $\alpha'_{TPP} = 1.2°$; $\mu = 0.281$; $\theta = 9.4°$. Run point 679.

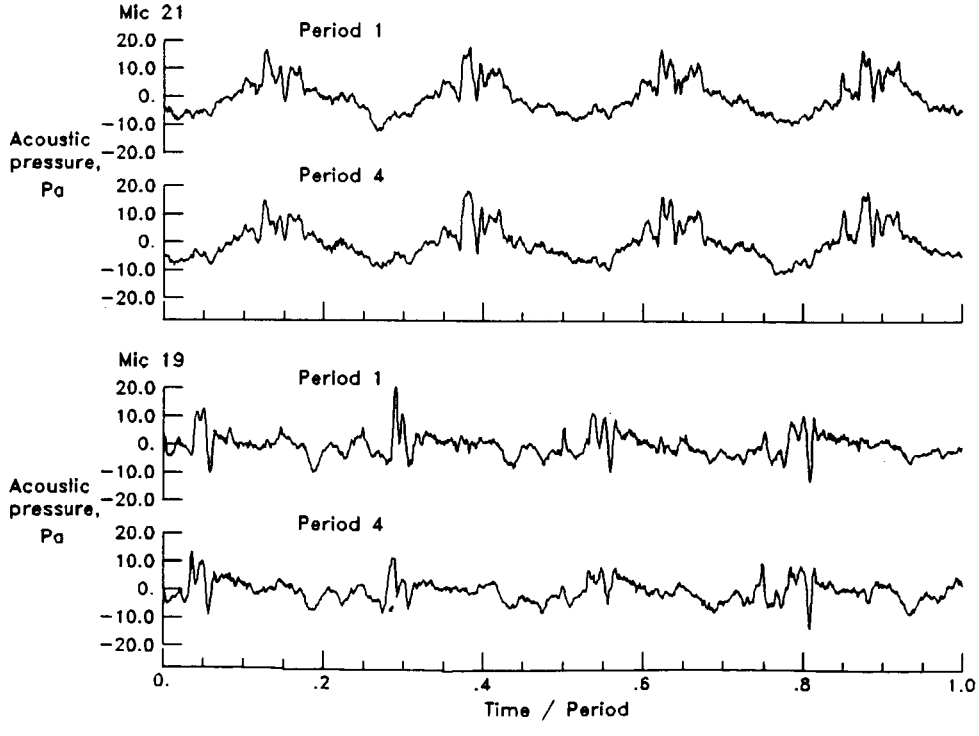

(r) $\alpha_{TPP} = 0.1°$; $\alpha_{TPP} = -0.3°$; $\mu = 0.279$; $\theta = 7.7°$. Run point 677.

Figure 16. Continued.

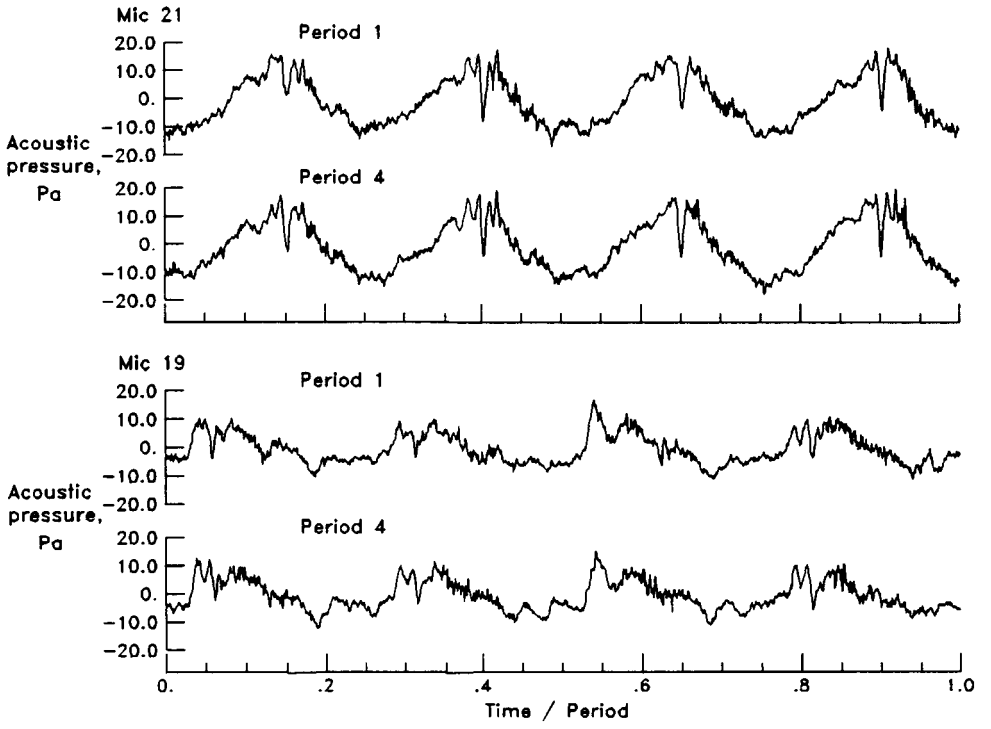

(s) $\alpha_{\mathrm{TPP}} = -2.4°$; $\alpha'_{\mathrm{TPP}} = -2.8°$; $\mu = 0.280$; $\theta = 5.2°$. Run point 680.

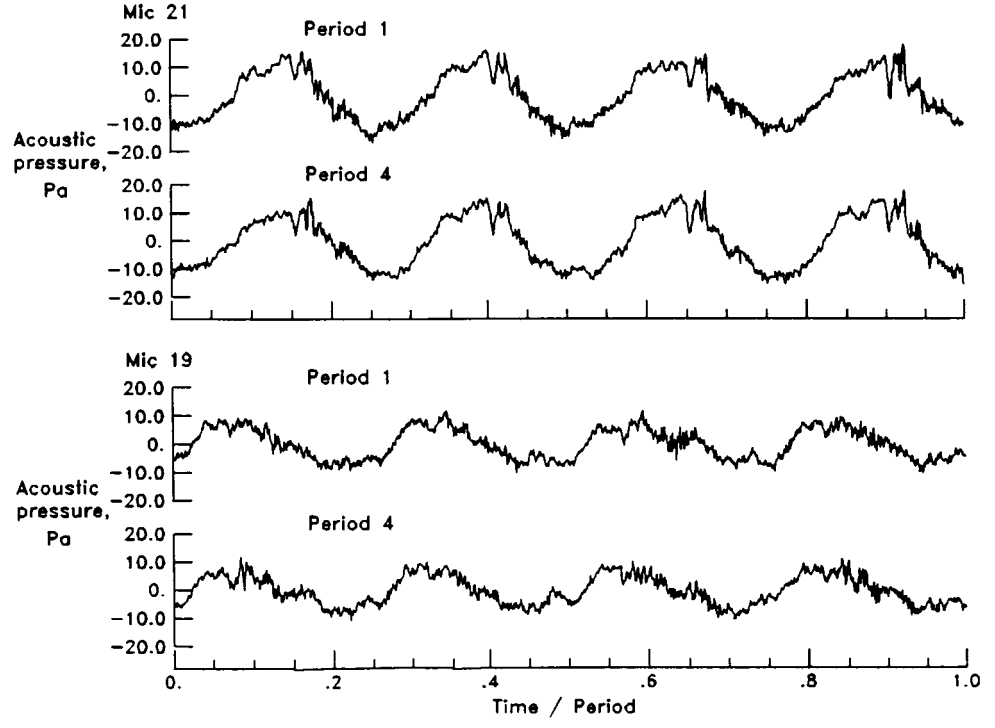

(t) $\alpha_{\mathrm{TPP}} = -3.9°$; $\alpha'_{\mathrm{TPP}} = -4.3°$; $\mu = 0.281$; $\theta = 3.7°$. Run point 682.

Figure 16. Continued.

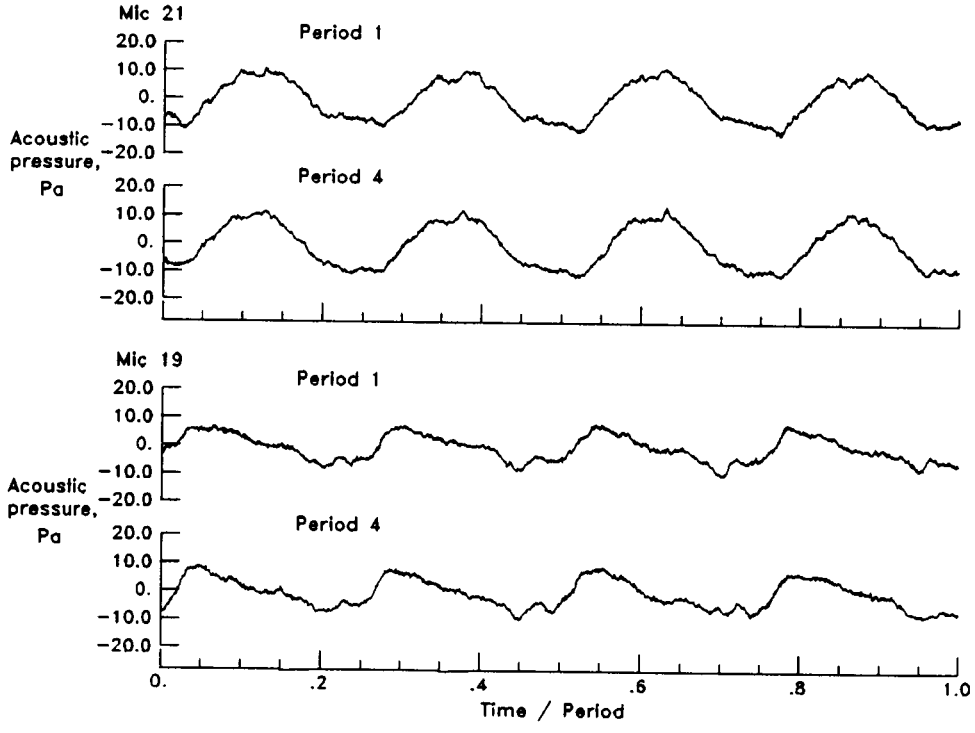

(u) $\alpha_{TPP} = -9.9°$; $\alpha'_{TPP} = -10.3°$; $\mu = 0.278$; $\theta = -2.6°$. Run point 681.

Figure 16. Concluded.

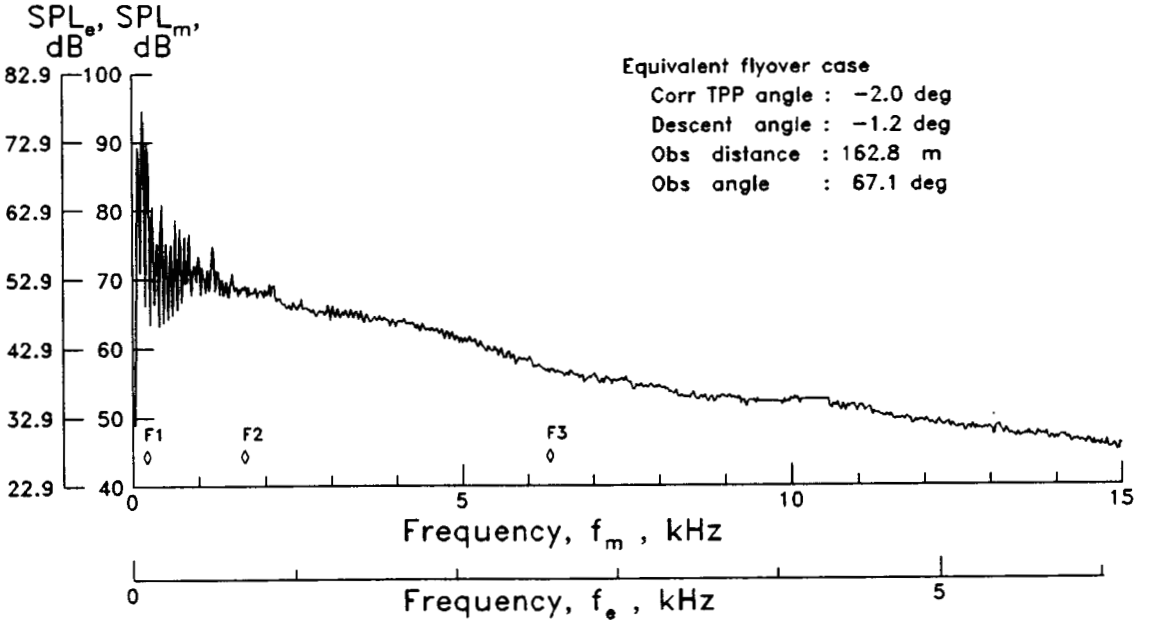

(a) $\alpha_{TPP} = 2.7°$; $\mu = 0.086$. Run point 659.

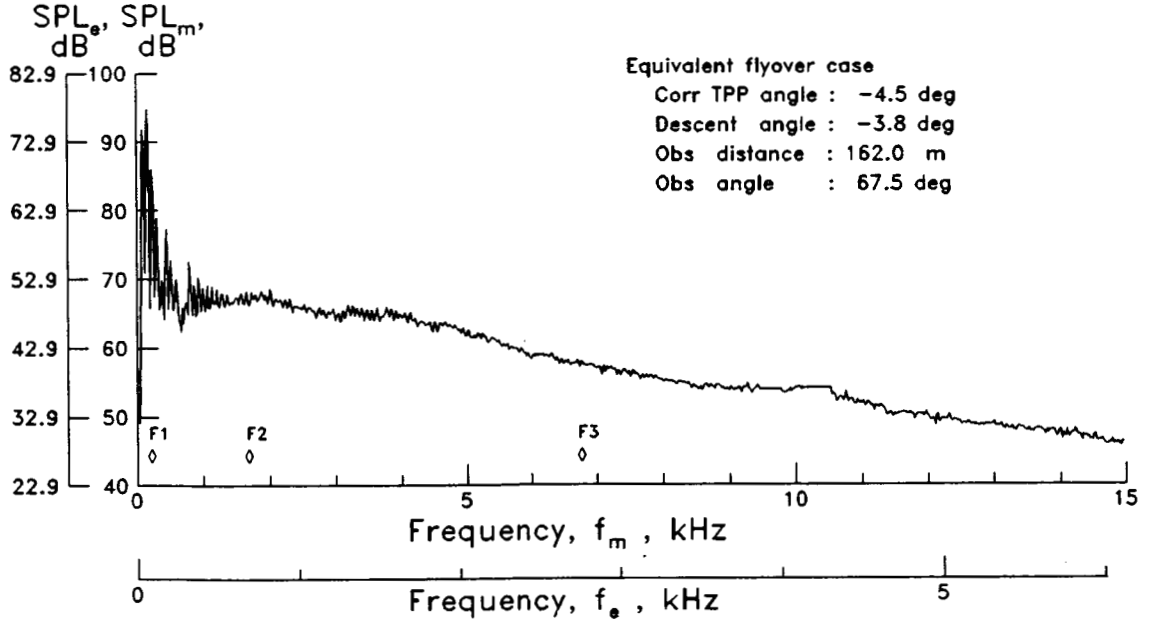

(b) $\alpha_{TPP} = 0.1°$; $\mu = 0.086$. Run point 660.

Figure 17. Noise spectra from microphone 21 with equivalent flyover-observer scales.

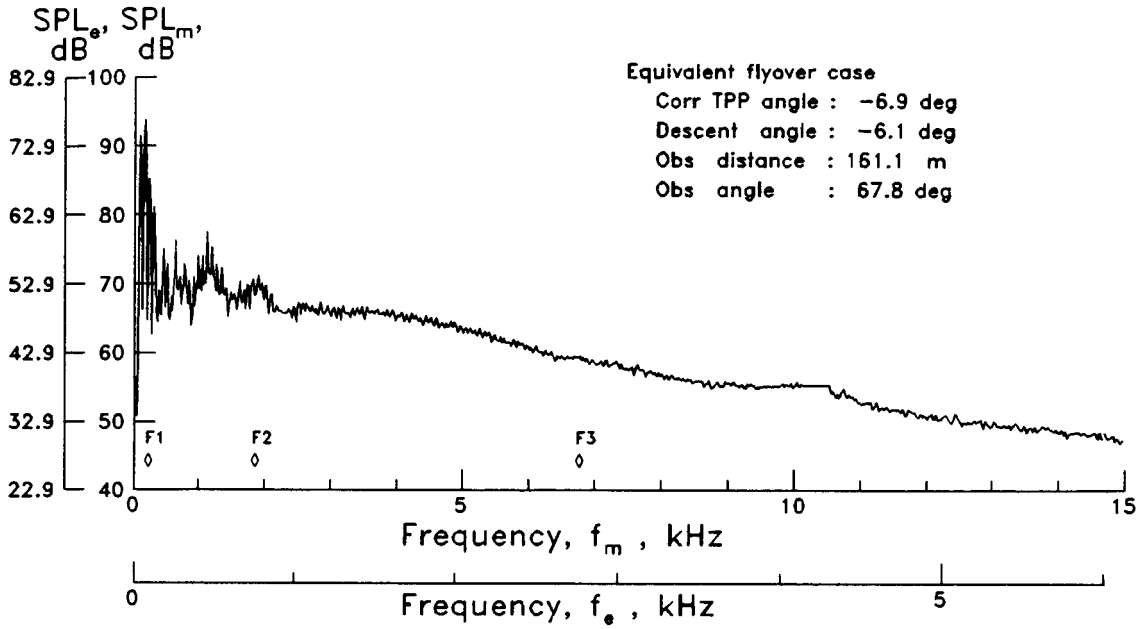

(c) $\alpha_{\mathrm{TPP}} = -2.4°$; $\mu = 0.088$. Run point 661.

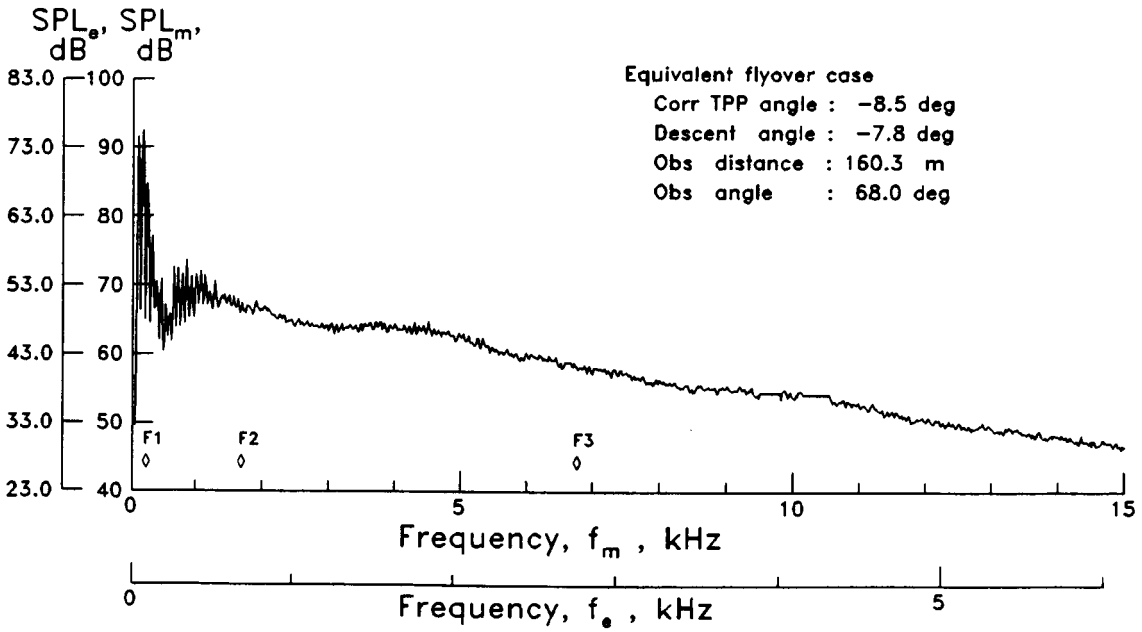

(d) $\alpha_{\mathrm{TPP}} = -3.9°$; $\mu = 0.087$. Run point 662.

Figure 17. Continued.

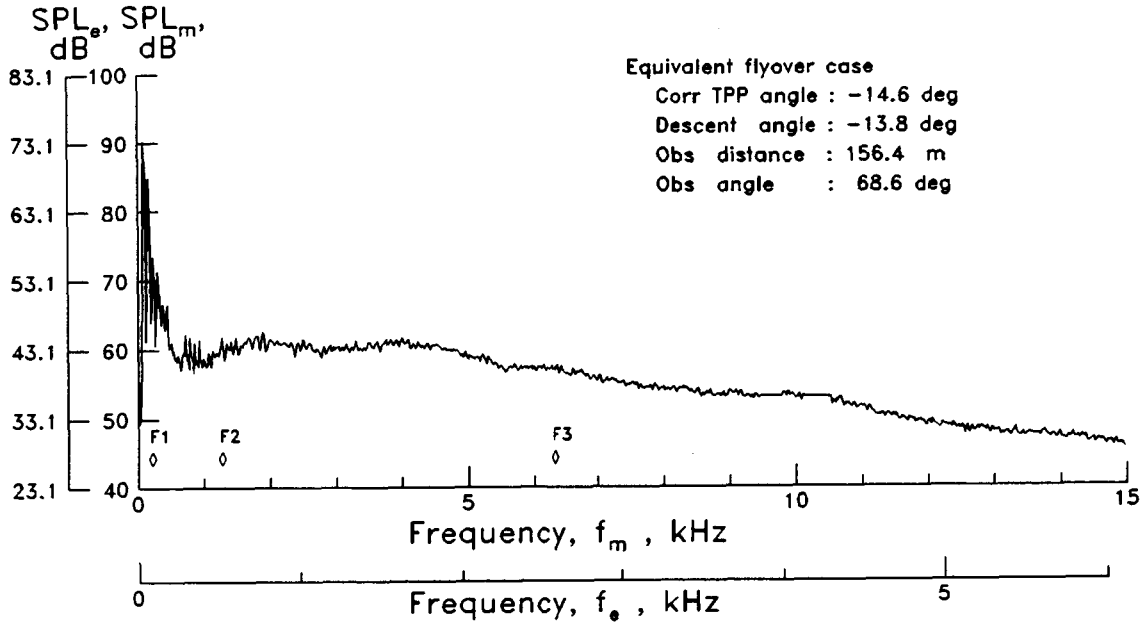

(e) $\alpha_{\mathrm{TPP}} = -9.9°$; $\mu = 0.085$. Run point 669.

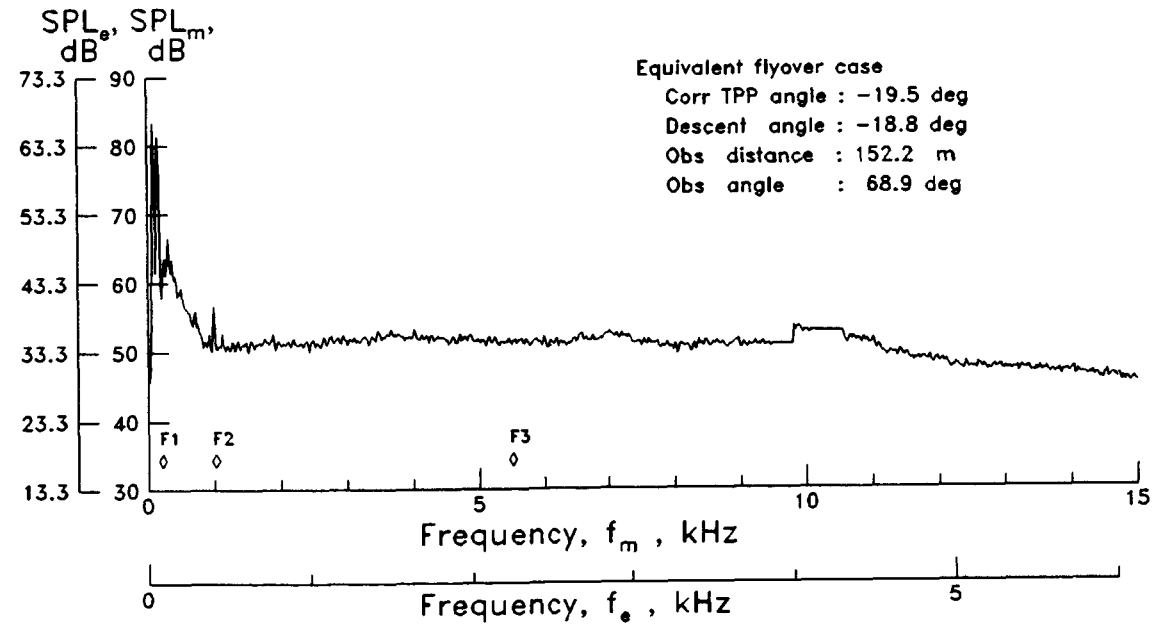

(f) $\alpha_{\mathrm{TPP}} = -14.9°$; $\mu = 0.084$. Run point 670.

Figure 17. Continued.

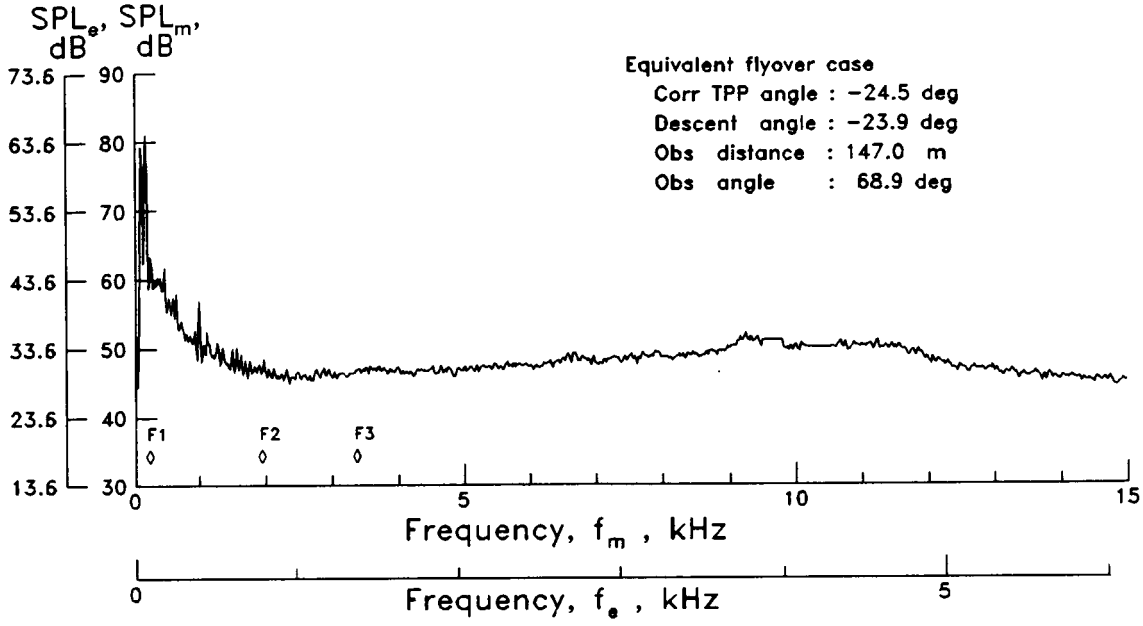

(g) $\alpha_{\mathrm{TPP}} = -19.9°$; $\mu = 0.082$. Run point 671.

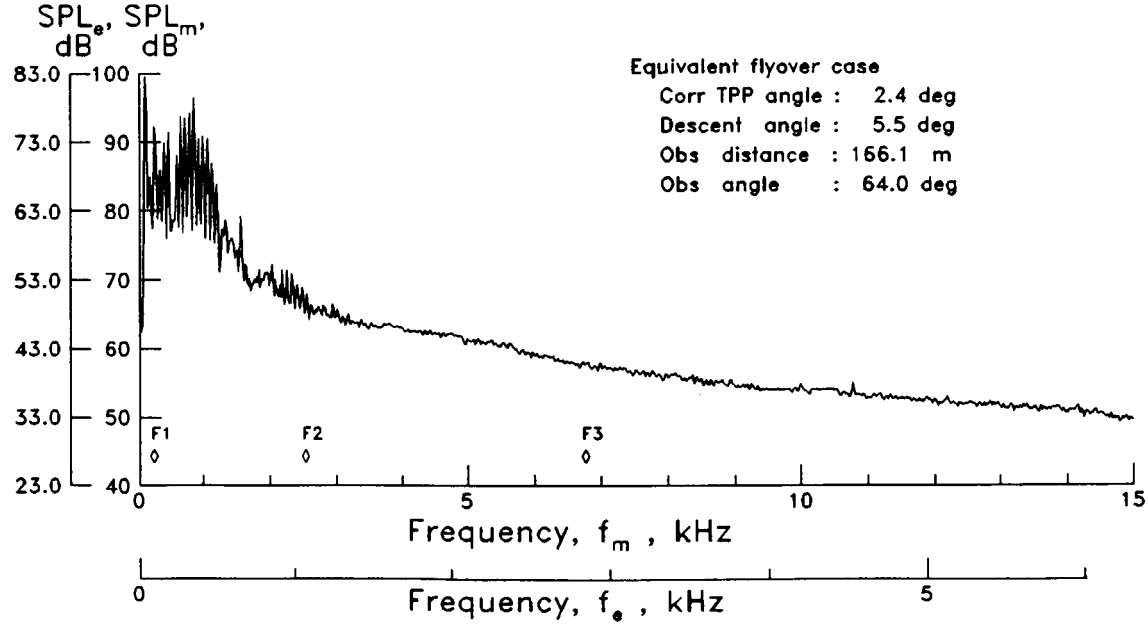

(h) $\alpha_{\mathrm{TPP}} = 3.6°$; $\mu = 0.174$. Run point 638.

Figure 17. Continued.

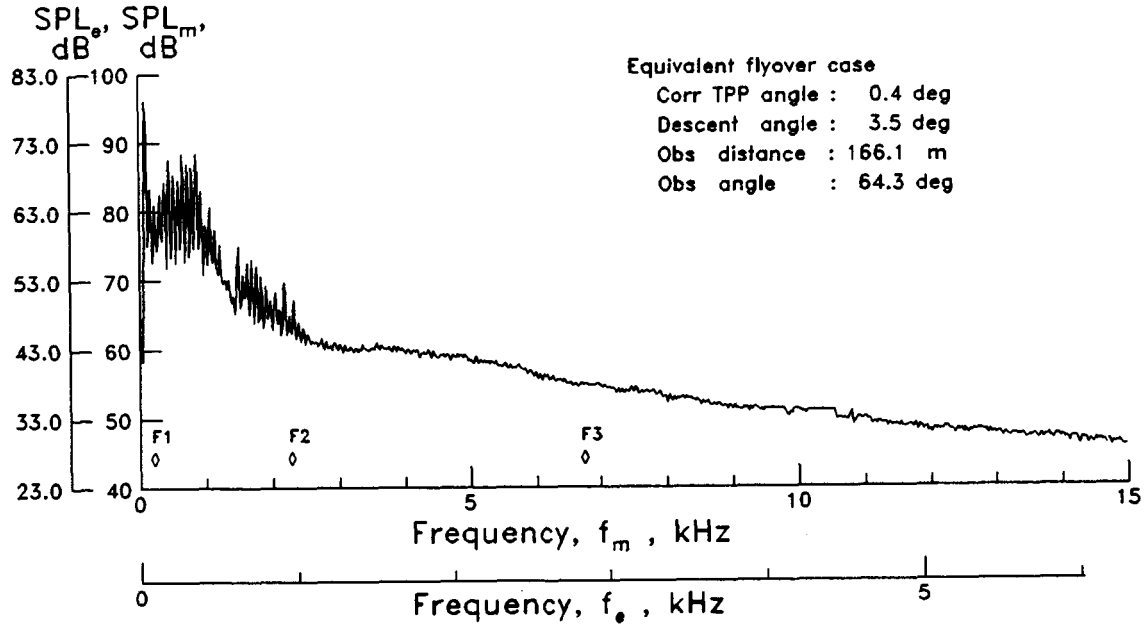

(i) $\alpha_{\mathrm{TPP}} = 1.6°$; $\mu = 0.175$. Run point 640.

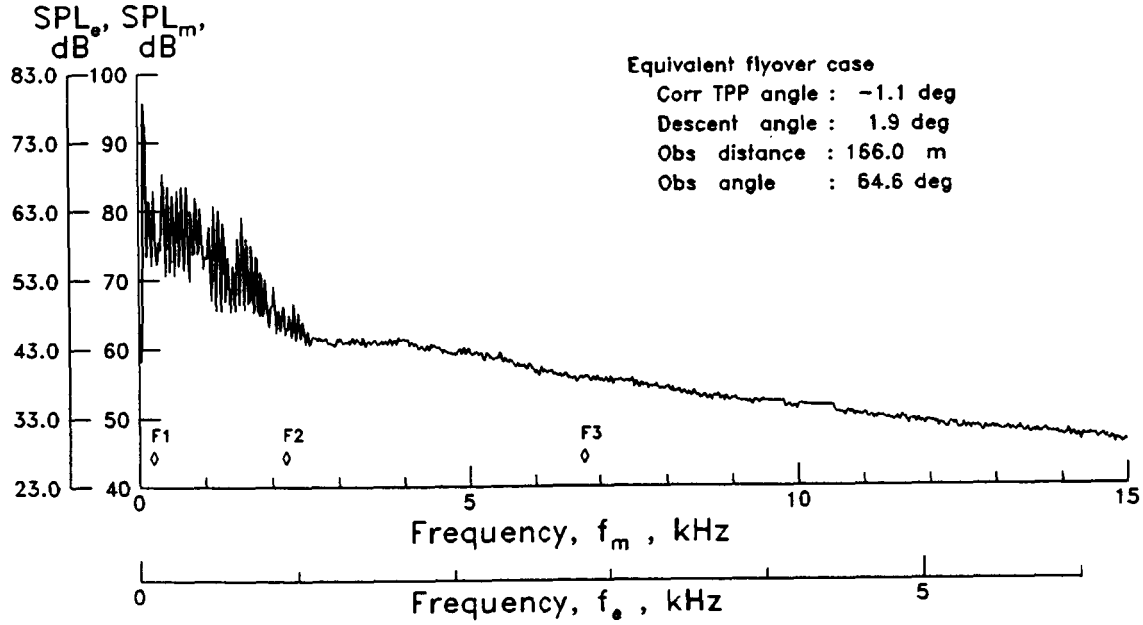

(j) $\alpha_{\mathrm{TPP}} = 0.1°$; $\mu = 0.174$. Run point 642.

Figure 17. Continued.

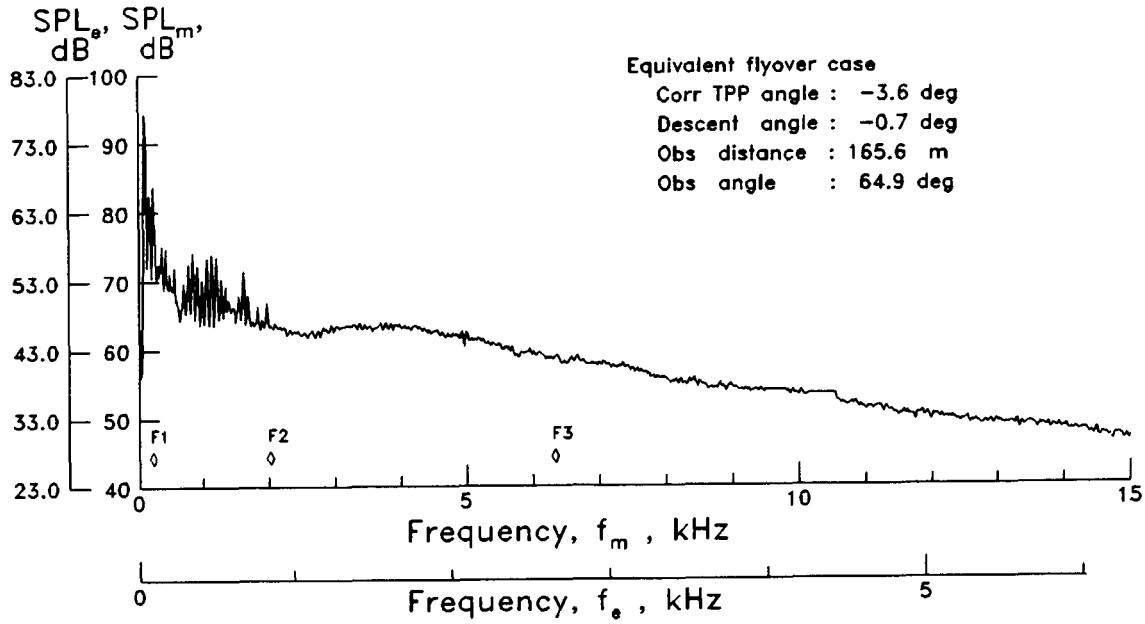

(k) $\alpha_{\mathrm{TPP}} = -2.4°$; $\mu = 0.172$. Run point 646.

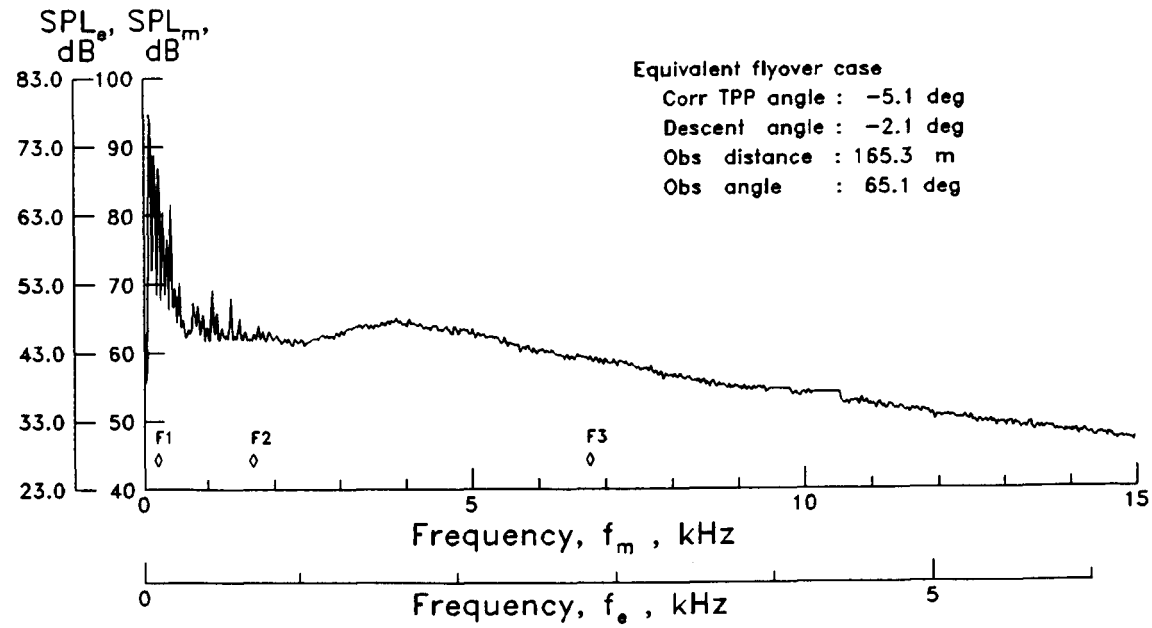

(l) $\alpha_{\mathrm{TPP}} = -3.9°$; $\mu = 0.173$. Run point 649.

Figure 17. Continued.

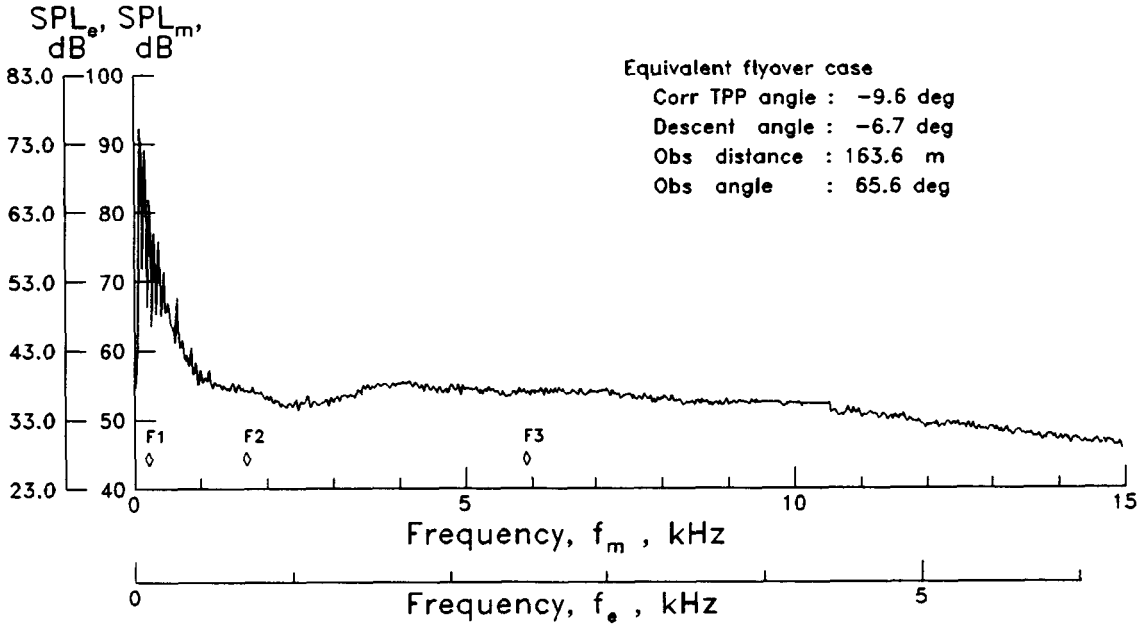

(m) $\alpha_{\mathrm{TPP}} = -8.4°$; $\mu = 0.173$. Run point 652.

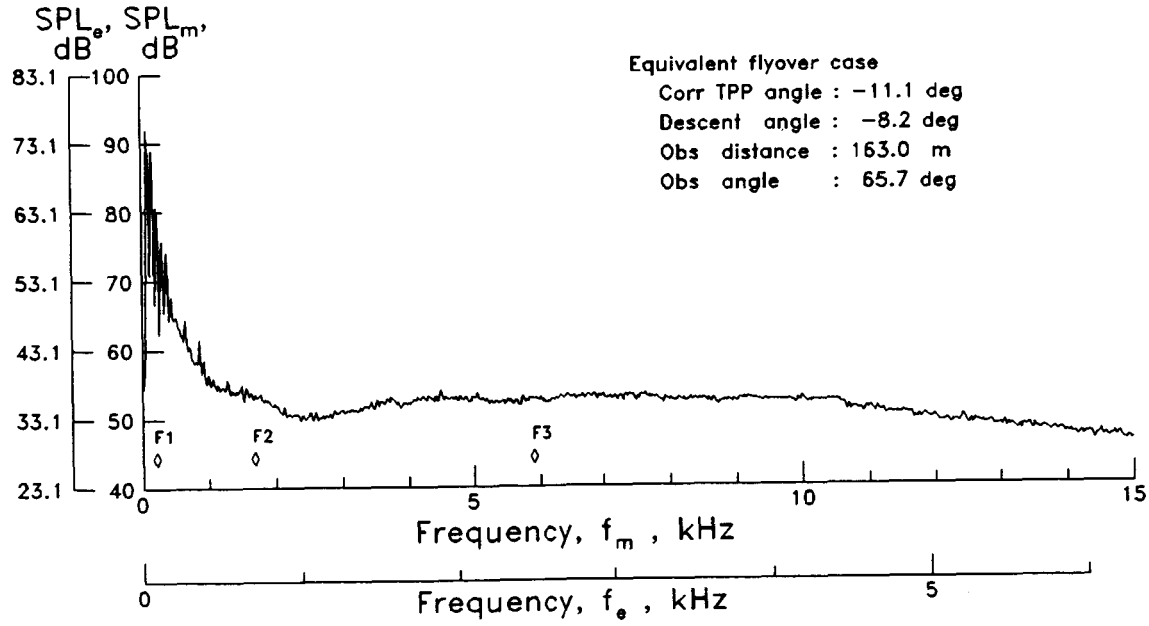

(n) $\alpha_{\mathrm{TPP}} = -9.9°$; $\mu = 0.171$. Run point 653.

Figure 17. Continued.

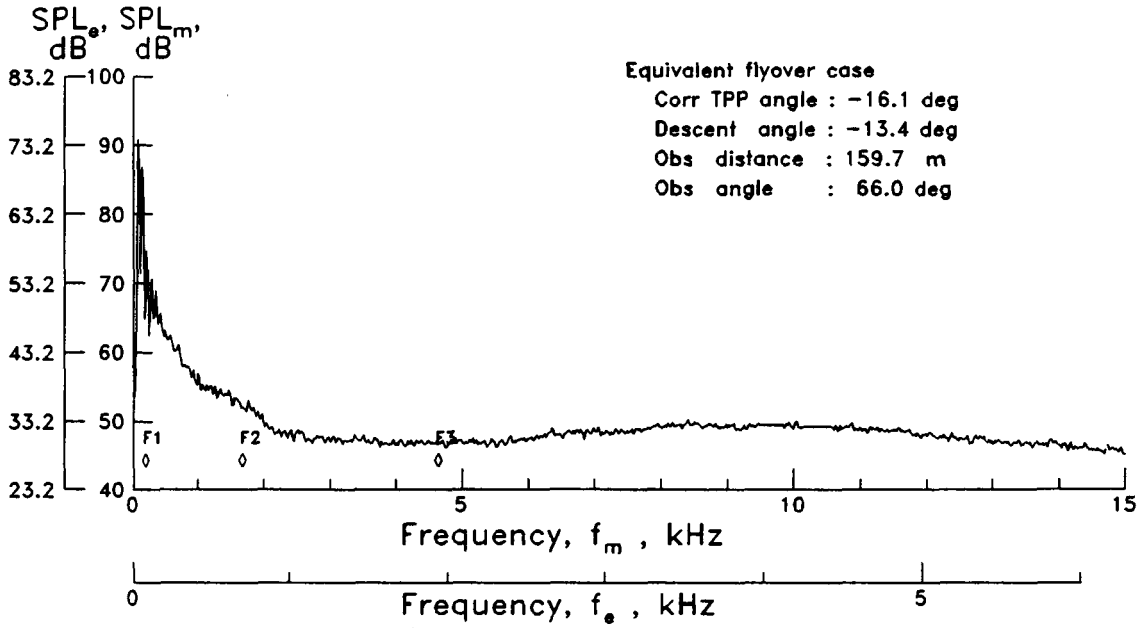

(o) $\alpha_{\mathrm{TPP}} = -14.9°$; $\mu = 0.169$. Run point 656.

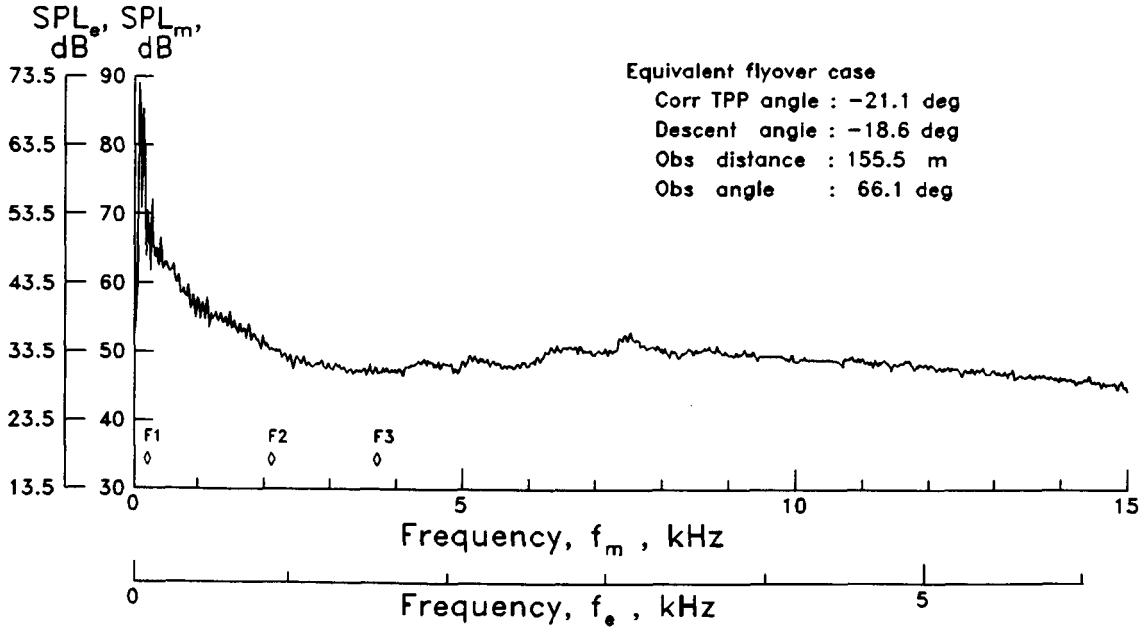

(p) $\alpha_{\mathrm{TPP}} = -19.8°$; $\mu = 0.164$. Run point 657.

Figure 17. Continued.

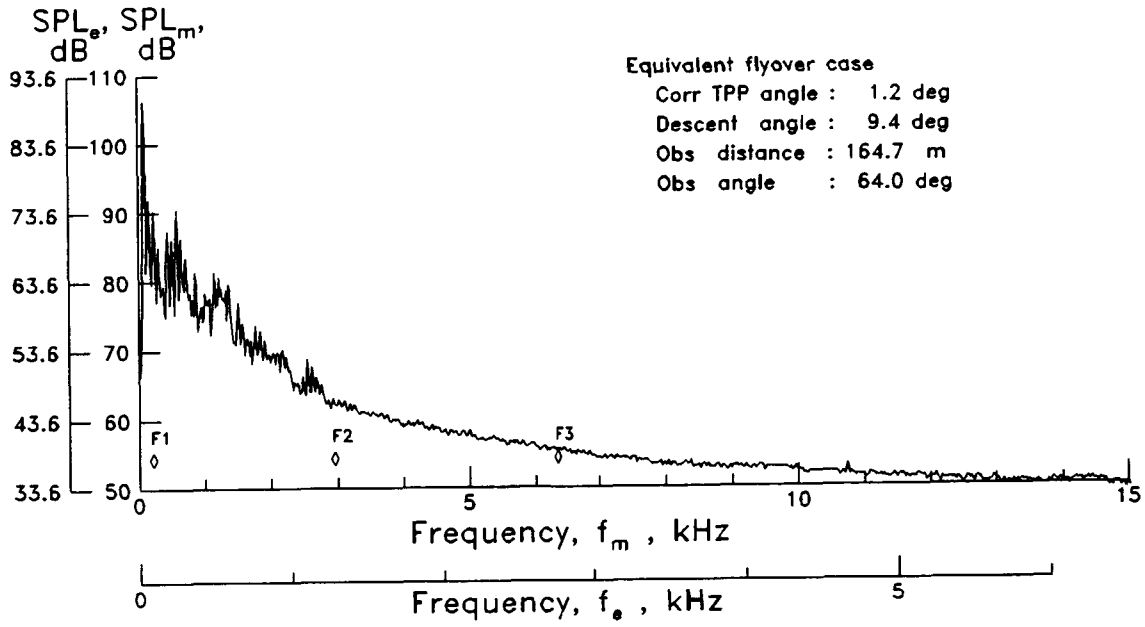

(q) $\alpha_{\mathrm{TPP}} = 1.6°$; $\mu = 0.281$. Run point 679.

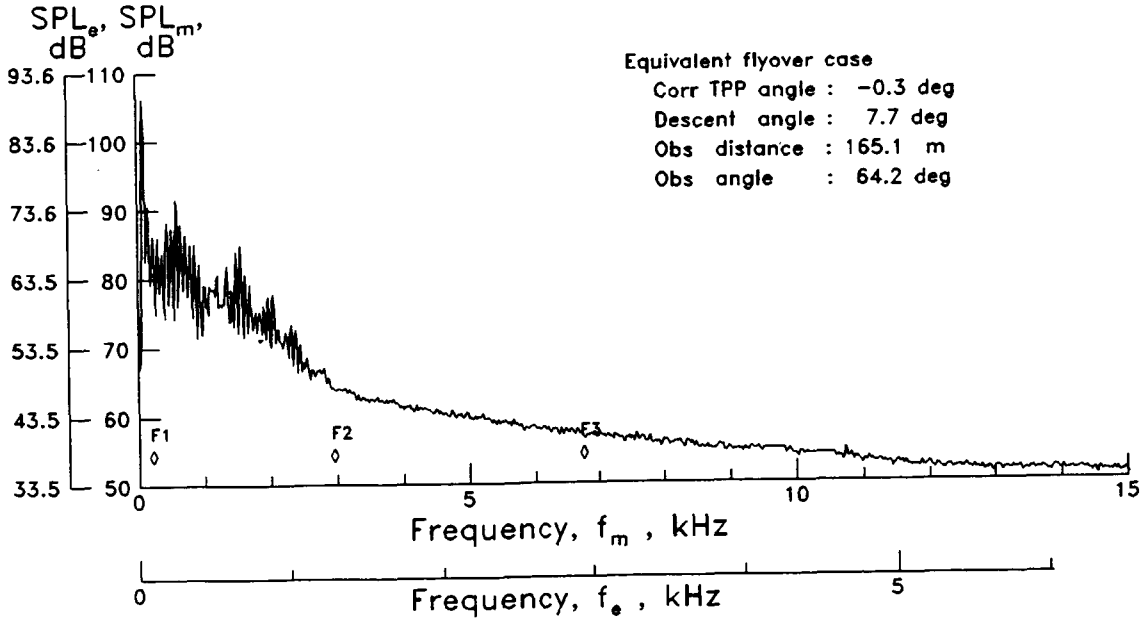

(r) $\alpha_{\mathrm{TPP}} = 0.1°$; $\mu = 0.279$. Run point 677.

Figure 17. Continued.

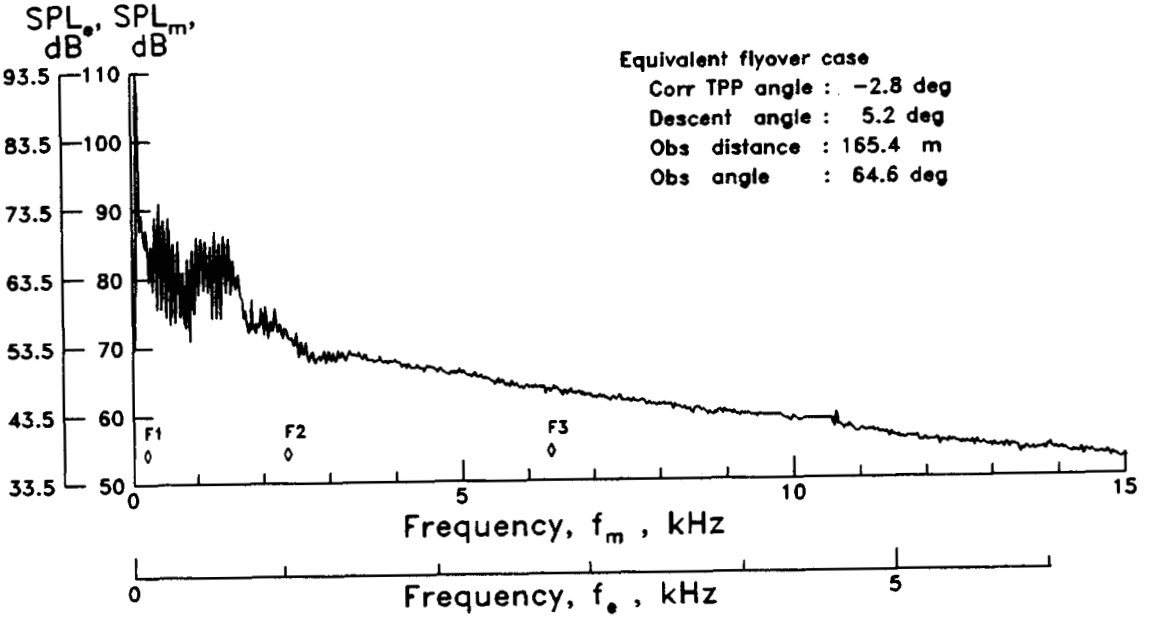

(s) $\alpha_{\mathrm{TPP}} = -2.4°$; $\mu = 0.280$. Run point 680.

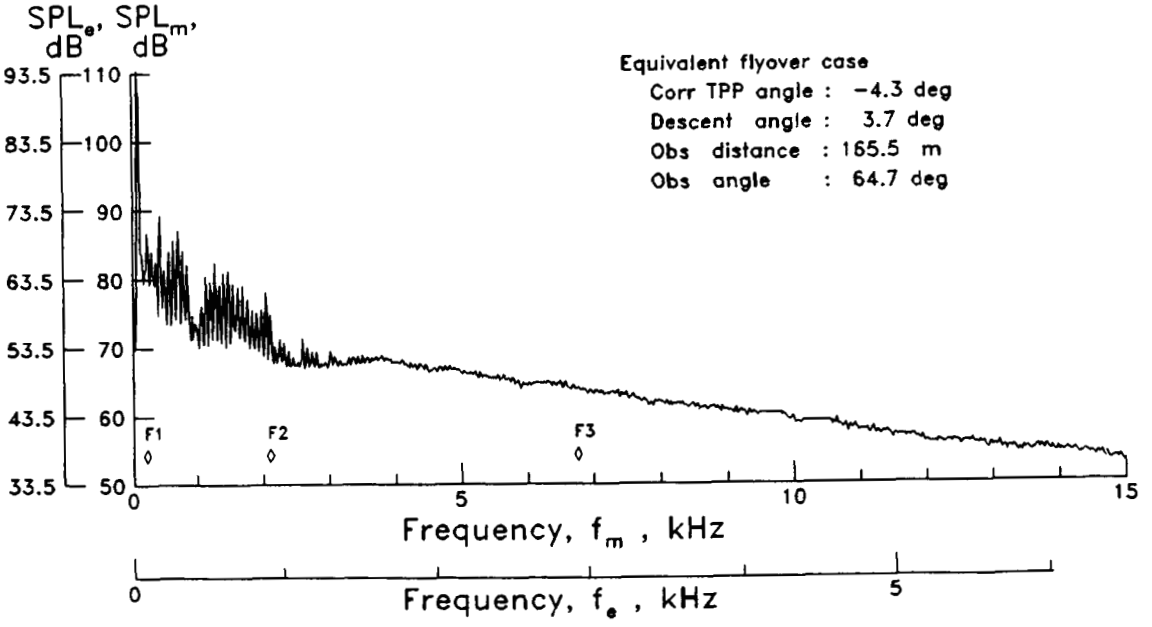

(t) $\alpha_{\mathrm{TPP}} = -3.9°$; $\mu = 0.281$. Run point 682.

Figure 17. Continued.

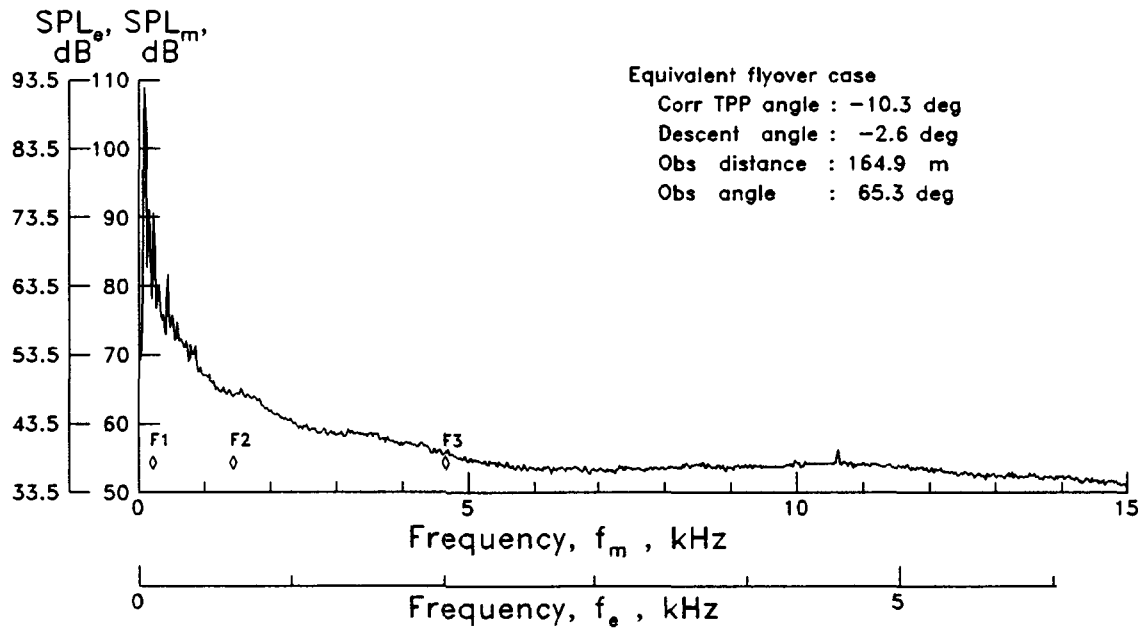

(u) $\alpha_{\mathrm{TPP}} = -9.9°$; $\mu = 0.278$. Run point 681.

Figure 17. Concluded.

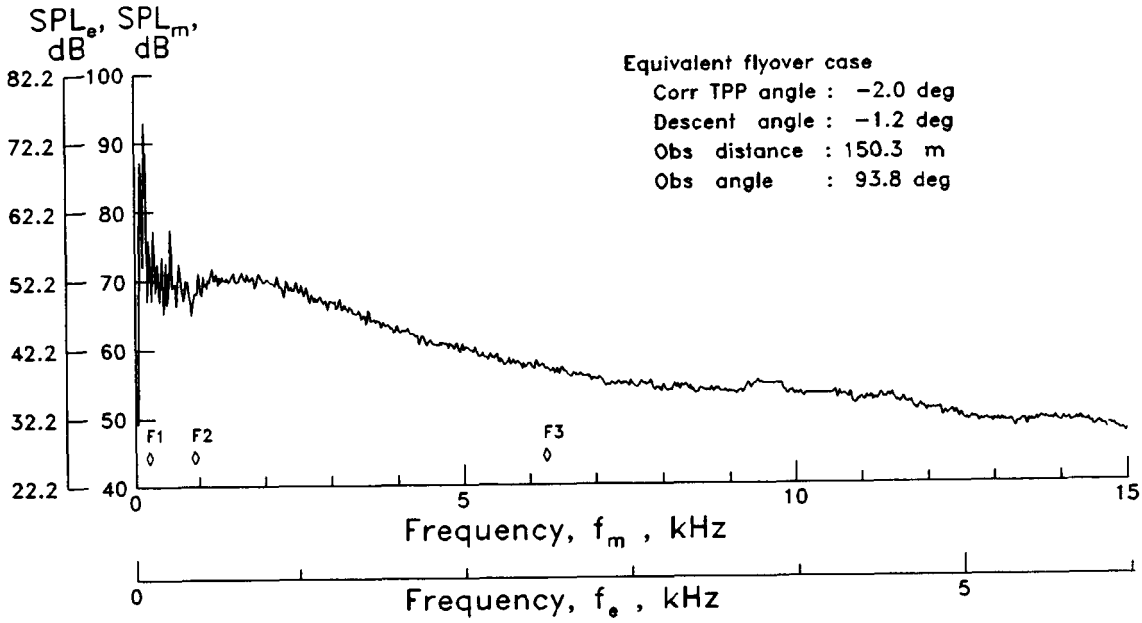

(a) $\alpha_{\mathrm{TPP}} = 2.7°$; $\mu = 0.086$. Run point 659.

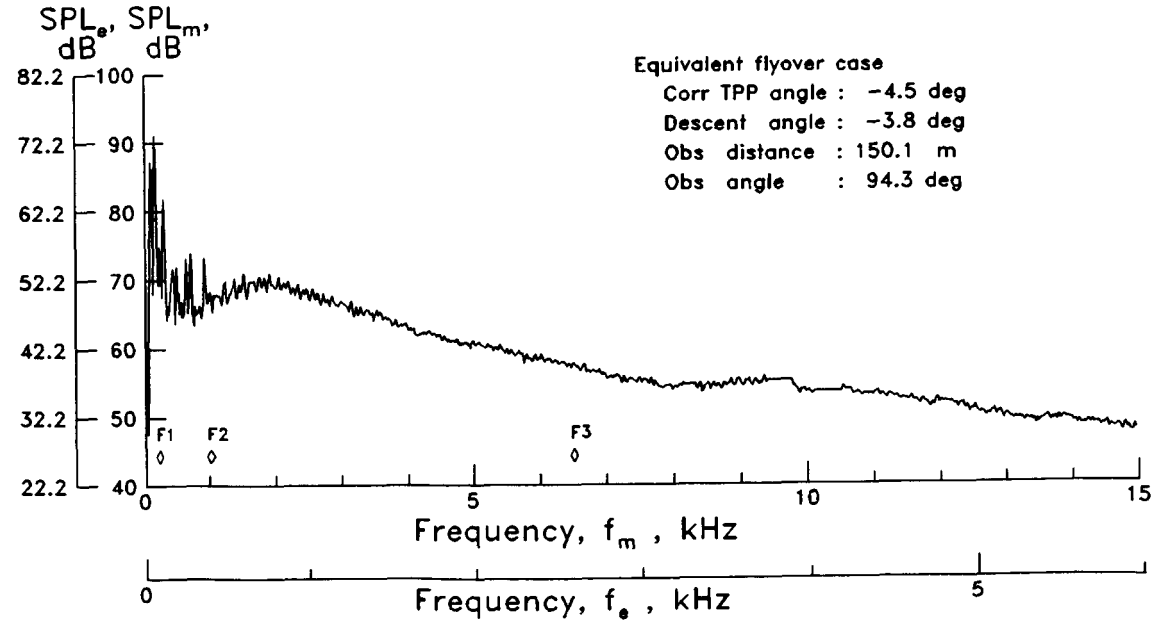

(b) $\alpha_{\mathrm{TPP}} = 0.1°$; $\mu = 0.086$. Run point 660.

Figure 18. Noise spectra from microphone 19 with equivalent flyover-observer scales.

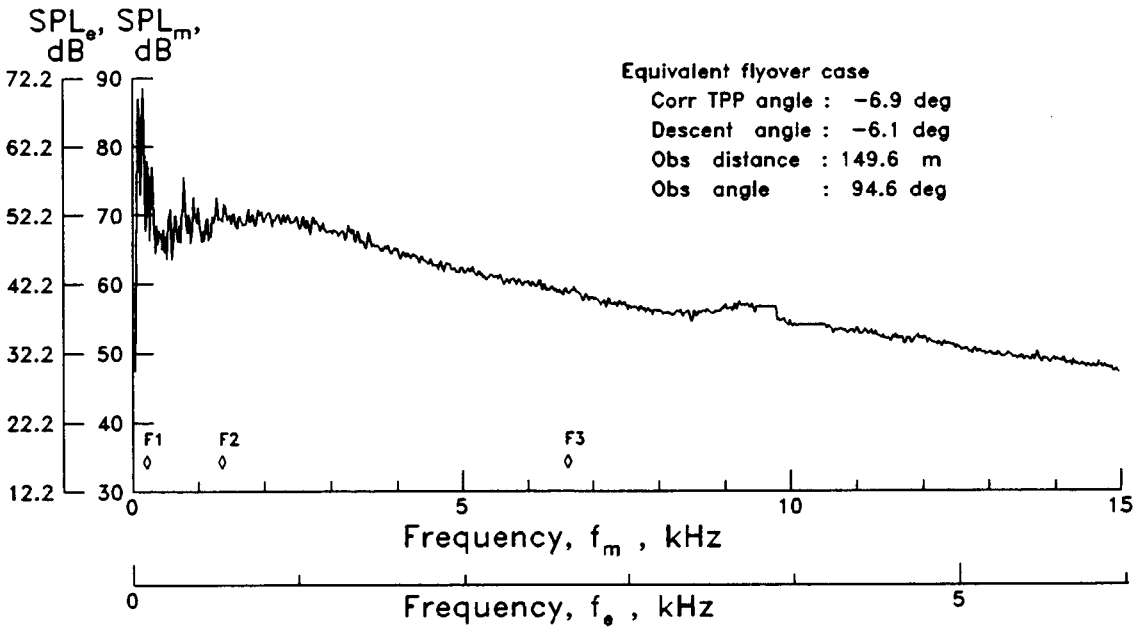

(c) $\alpha_{\mathrm{TPP}} = -2.4°$; $\mu = 0.088$. Run point 661.

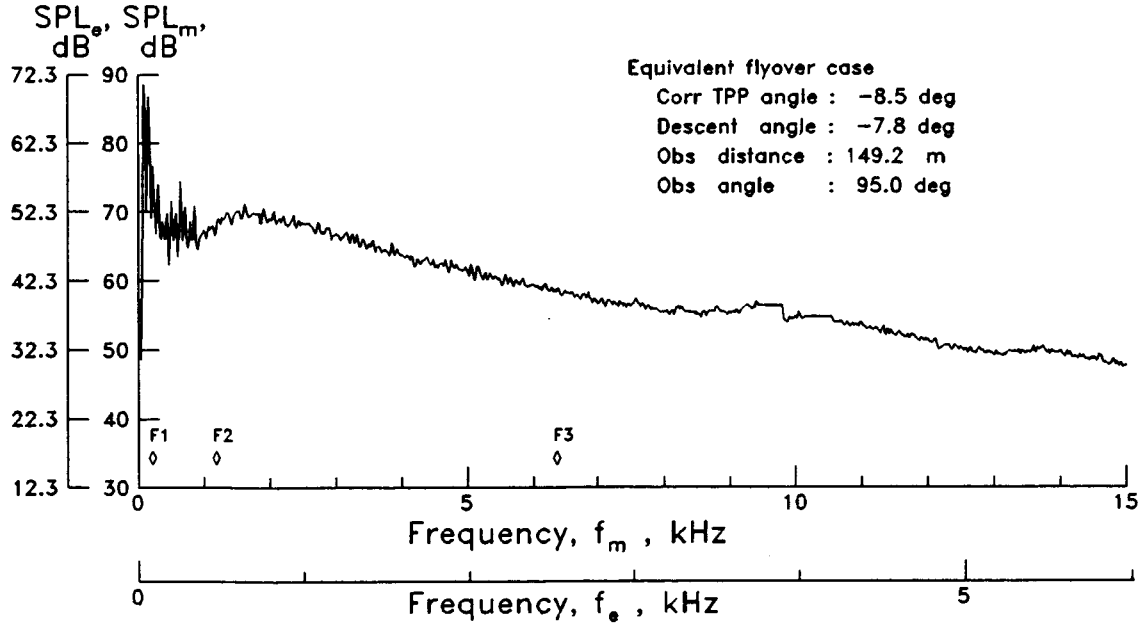

(d) $\alpha_{\mathrm{TPP}} = -3.9°$; $\mu = 0.087$. Run point 662.

Figure 18. Continued.

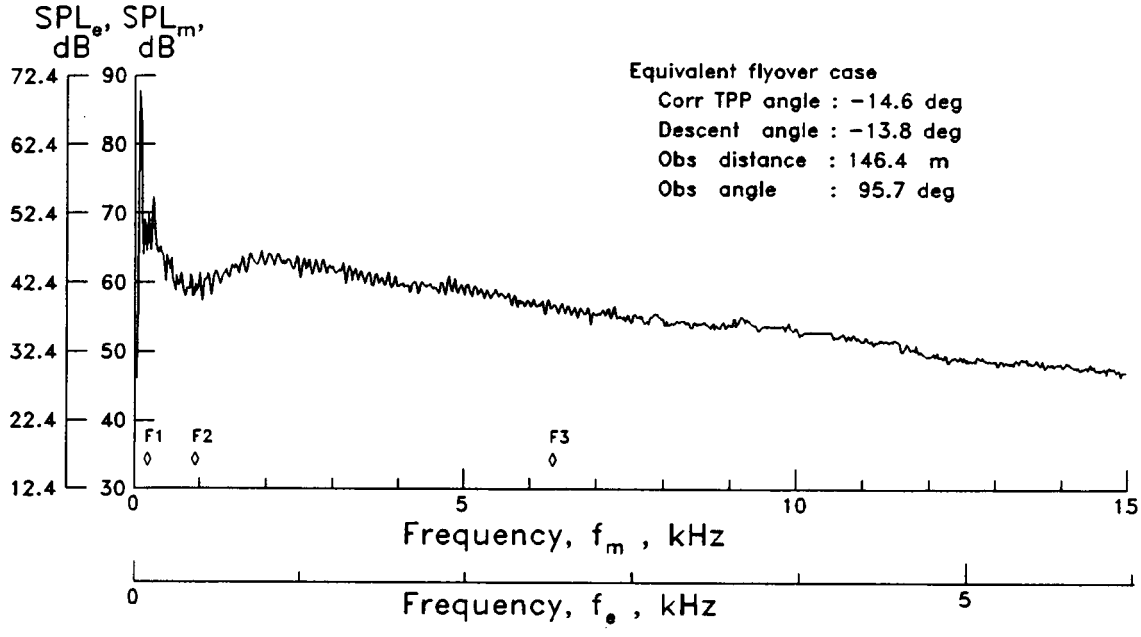

(e) $\alpha_{\mathrm{TPP}} = -9.9°$; $\mu = 0.085$. Run point 669.

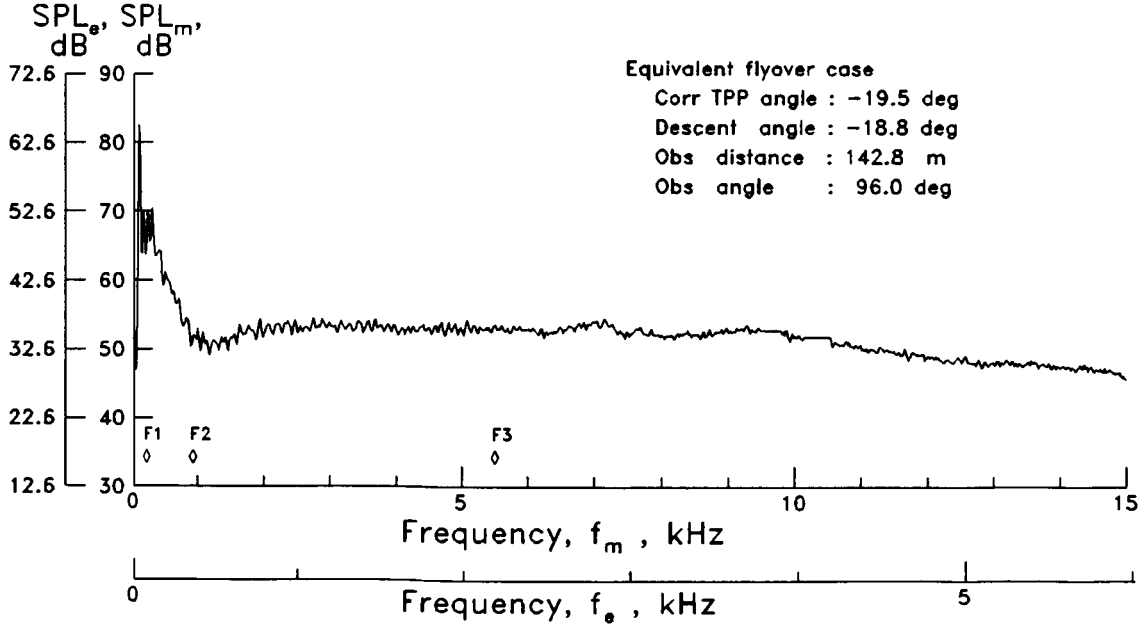

(f) $\alpha_{\mathrm{TPP}} = -14.9°$; $\mu = 0.084$. Run point 670.

Figure 18. Continued.

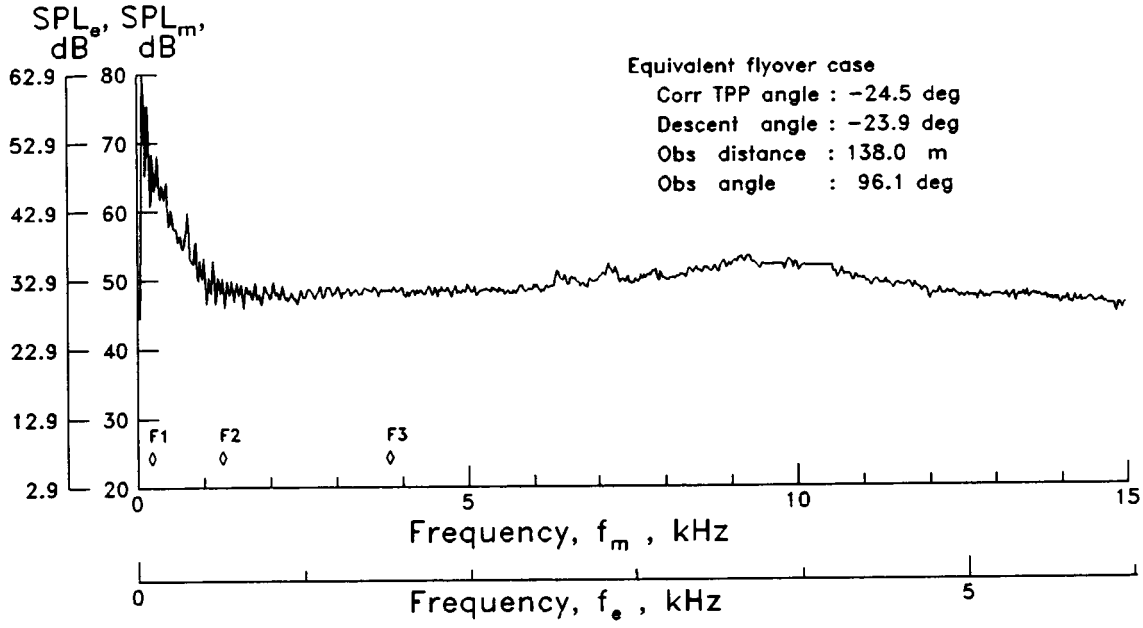

(g) $\alpha_{\mathrm{TPP}} = -19.9°$; $\mu = 0.082$. Run point 671.

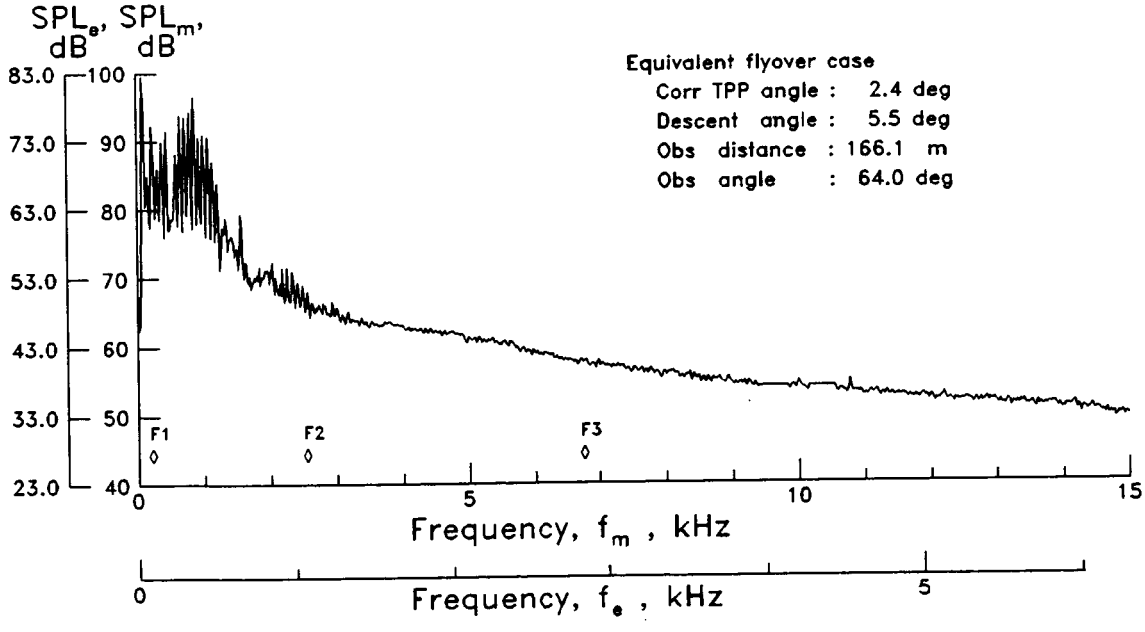

(h) $\alpha_{\mathrm{TPP}} = 3.6°$; $\mu = 0.174$. Run point 638.

Figure 18. Continued.

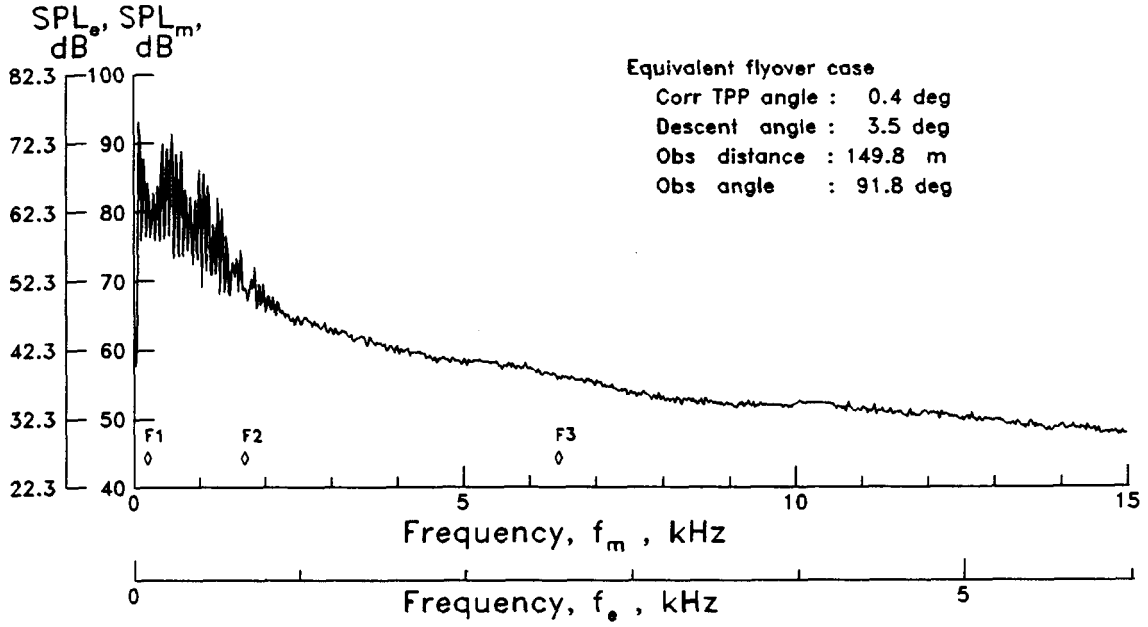

(i) $\alpha_{\mathrm{TPP}} = 1.6°$; $\mu = 0.175$. Run point 640.

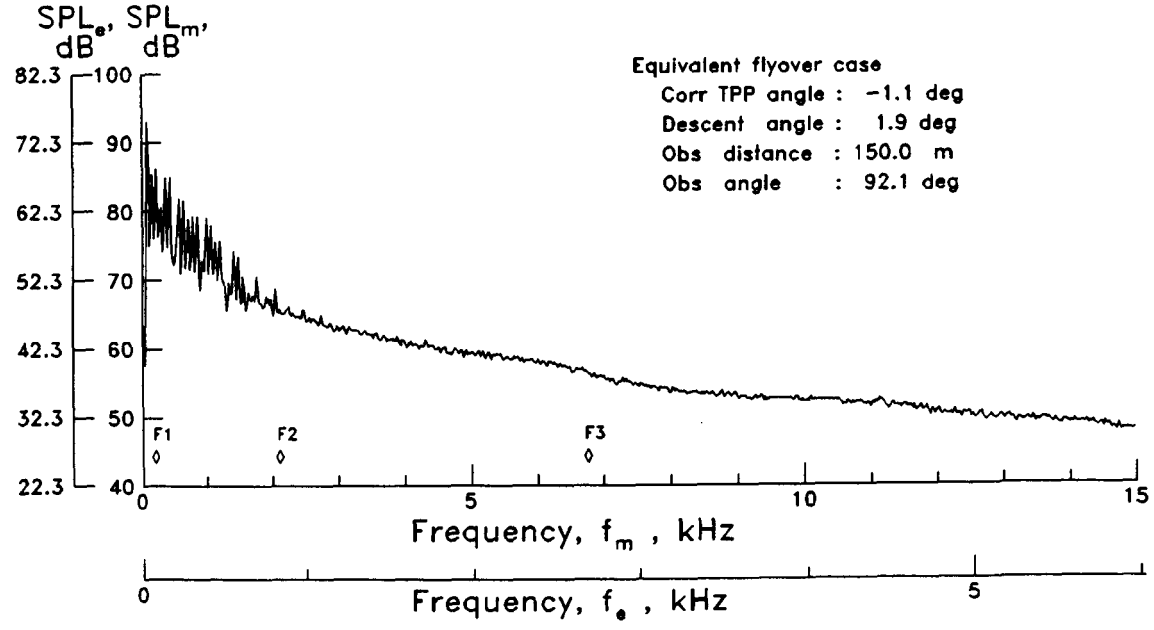

(j) $\alpha_{\mathrm{TPP}} = 0.1°$; $\mu = 0.174$. Run point 642.

Figure 18. Continued.

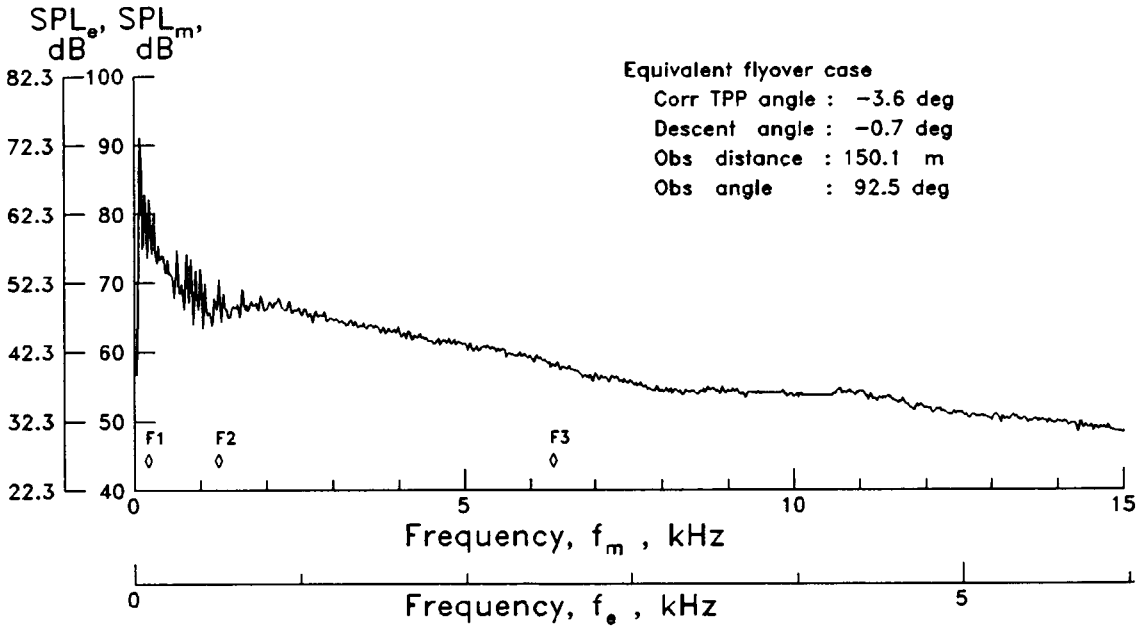

(k) $\alpha_{\mathrm{TPP}} = -2.4°$; $\mu = 0.172$. Run point 646.

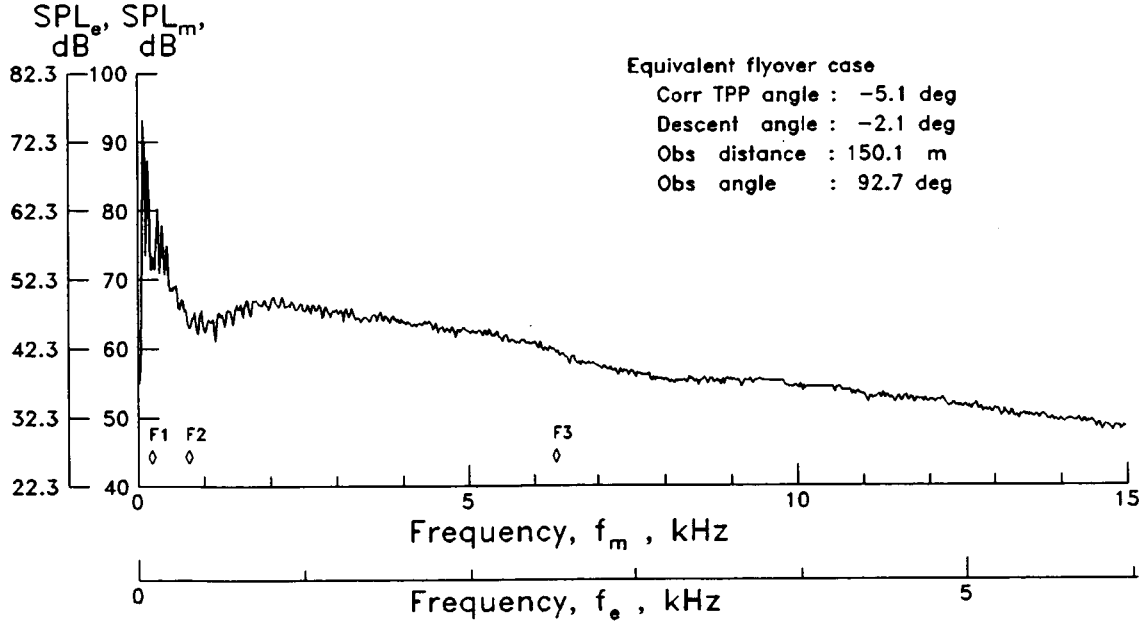

(l) $\alpha_{\mathrm{TPP}} = -3.9°$; $\mu = 0.173$. Run point 649.

Figure 18. Continued.

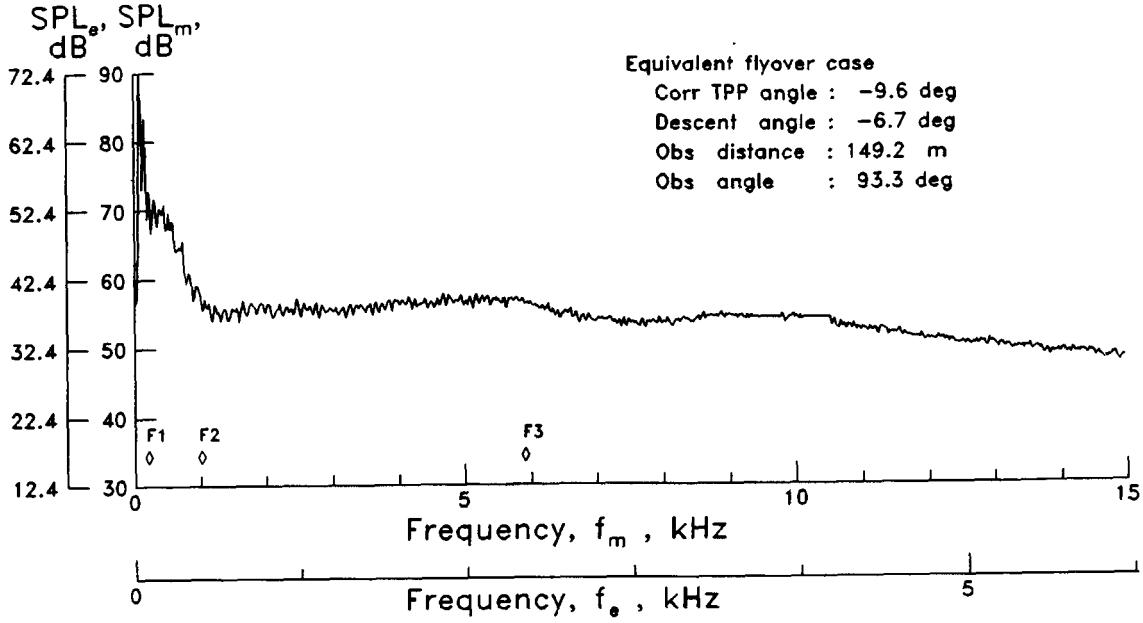

(m) $\alpha_{\mathrm{TPP}} = -8.4°$; $\mu = 0.173$. Run point 652.

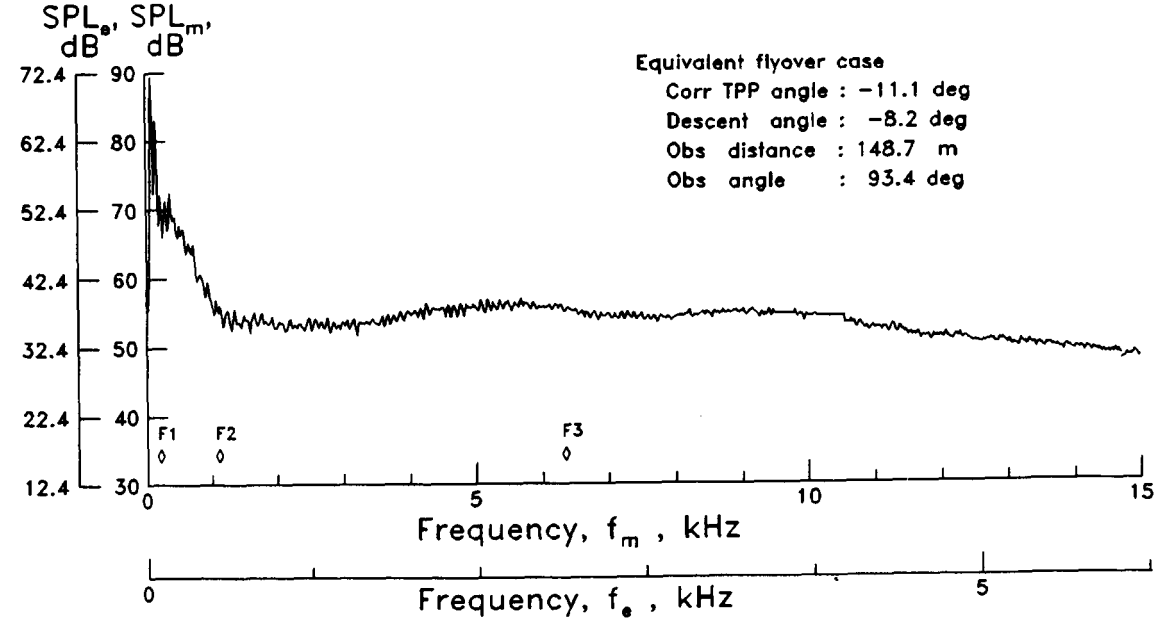

(n) $\alpha_{\mathrm{TPP}} = -9.9°$; $\mu = 0.171$. Run point 653.

Figure 18. Continued.

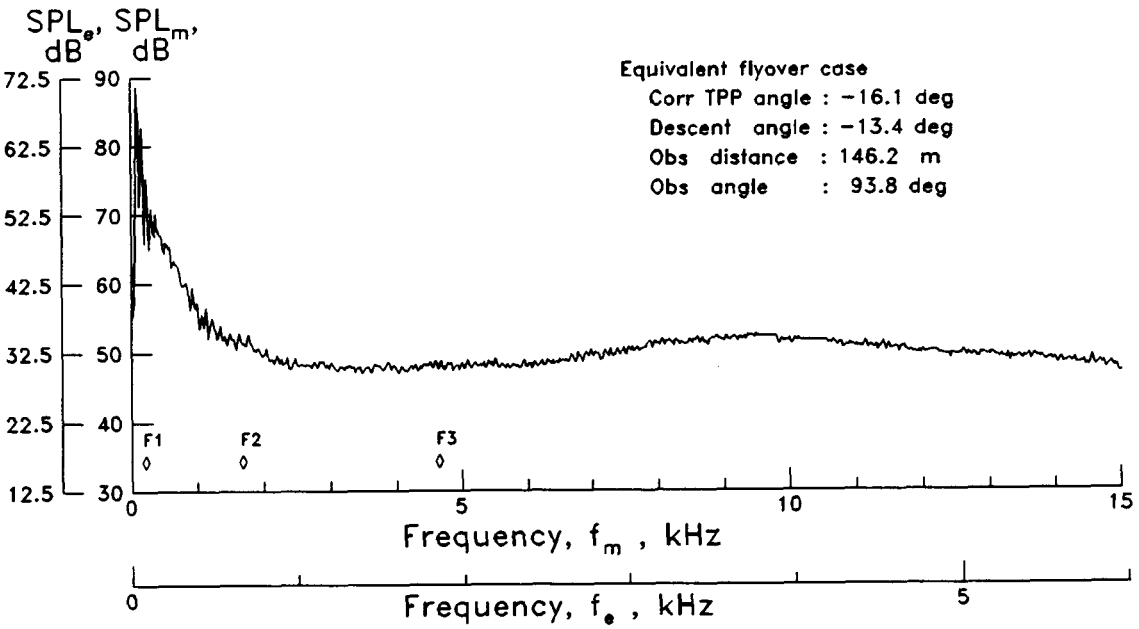

(o) $\alpha_{\mathrm{TPP}} = -14.9°$; $\mu = 0.169$. Run point 656.

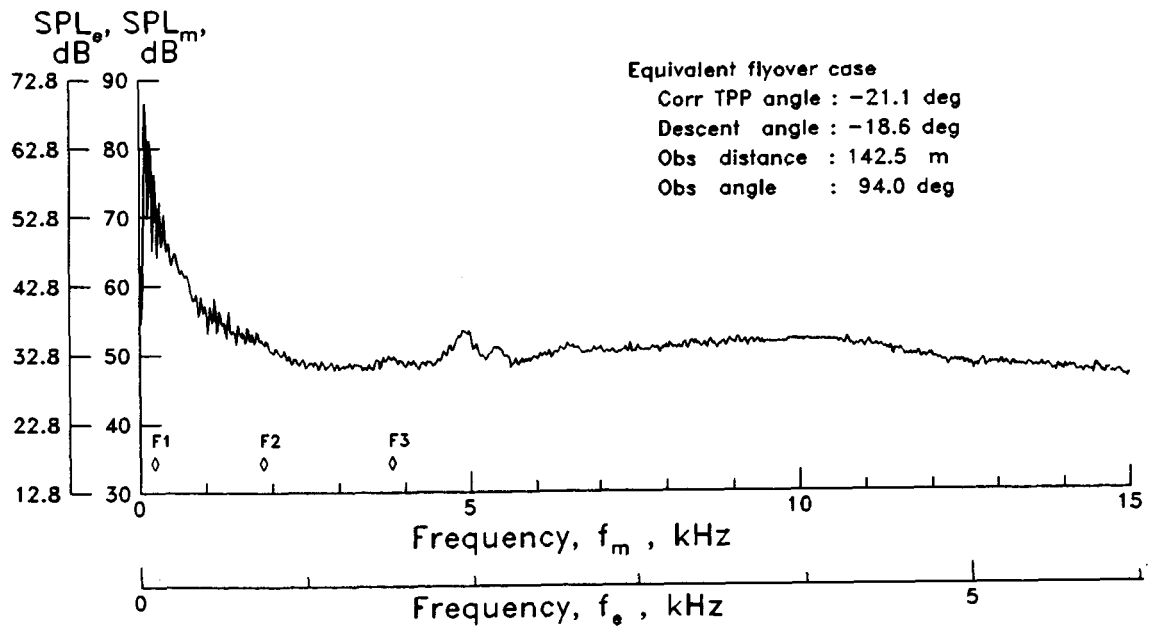

(p) $\alpha_{\mathrm{TPP}} = -19.8°$; $\mu = 0.164$. Run point 657.

Figure 18. Continued.

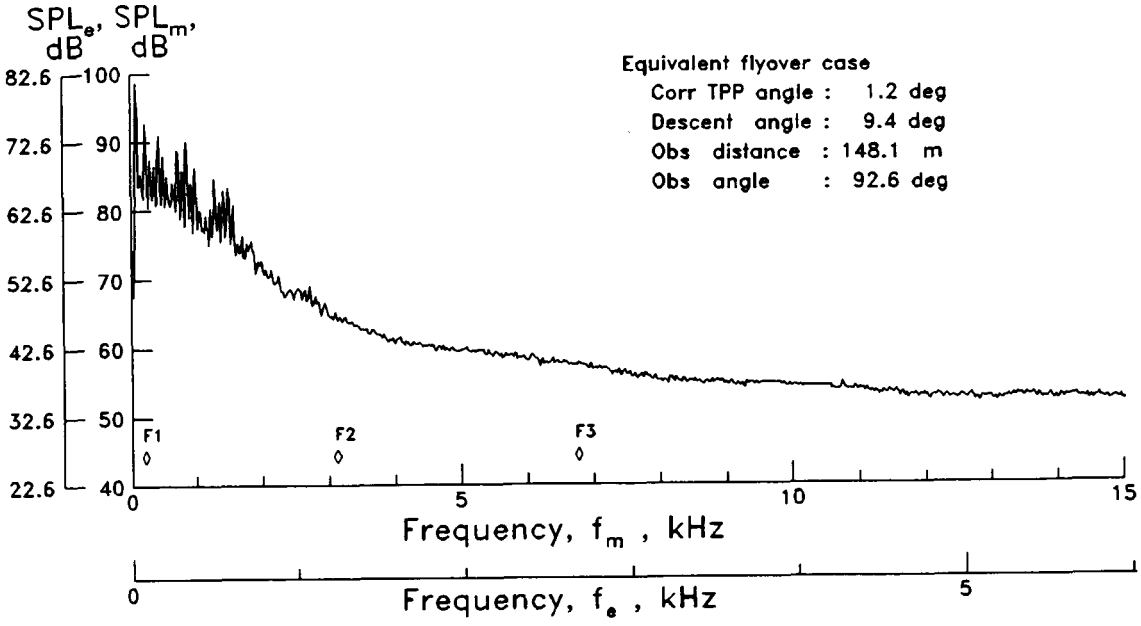

(q) $\alpha_{\mathrm{TPP}} = 1.6°$; $\mu = 0.281$. Run point 679.

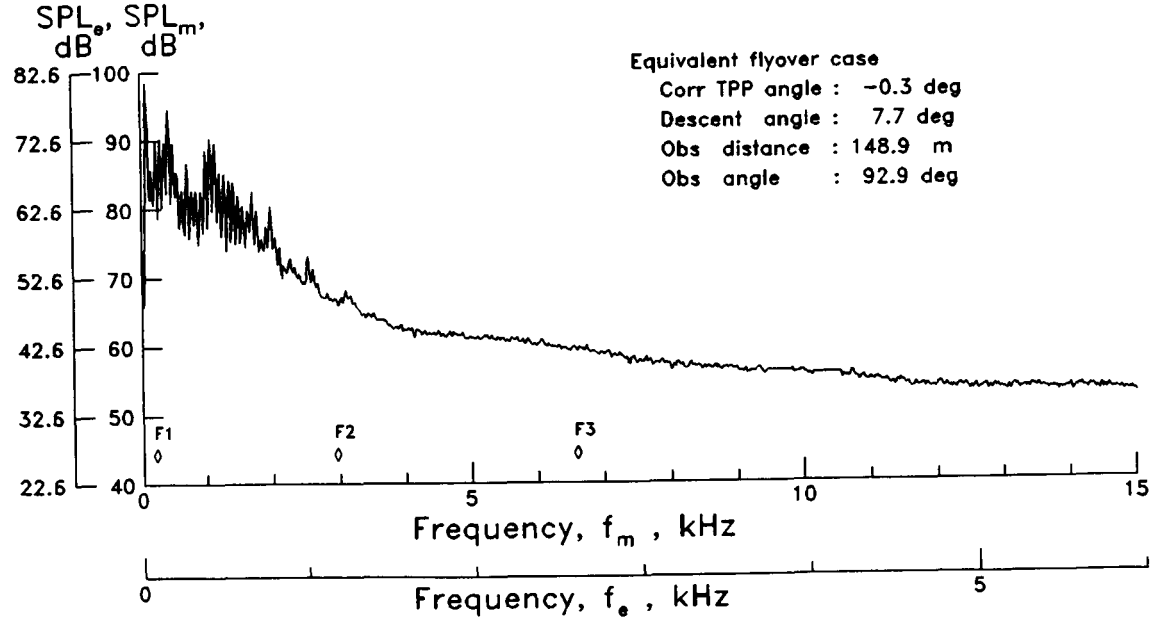

(r) $\alpha_{\mathrm{TPP}} = 0.1°$; $\mu = 0.279$. Run point 677.

Figure 18. Continued.

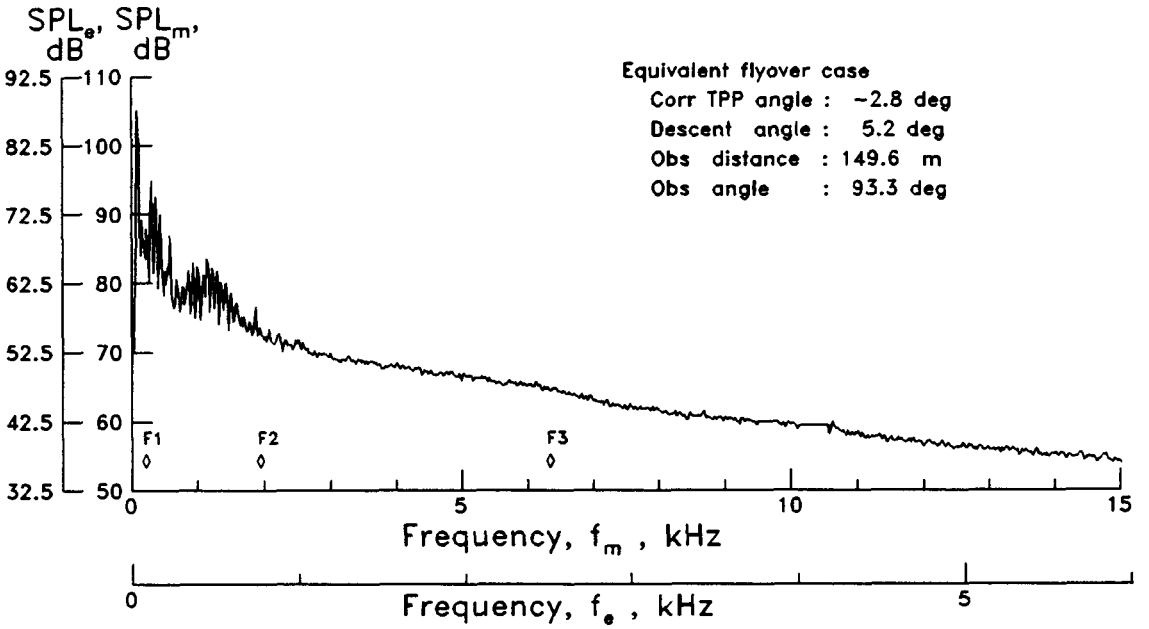

(s) $\alpha_{\mathrm{TPP}} = -2.4°$; $\mu = 0.280$. Run point 680.

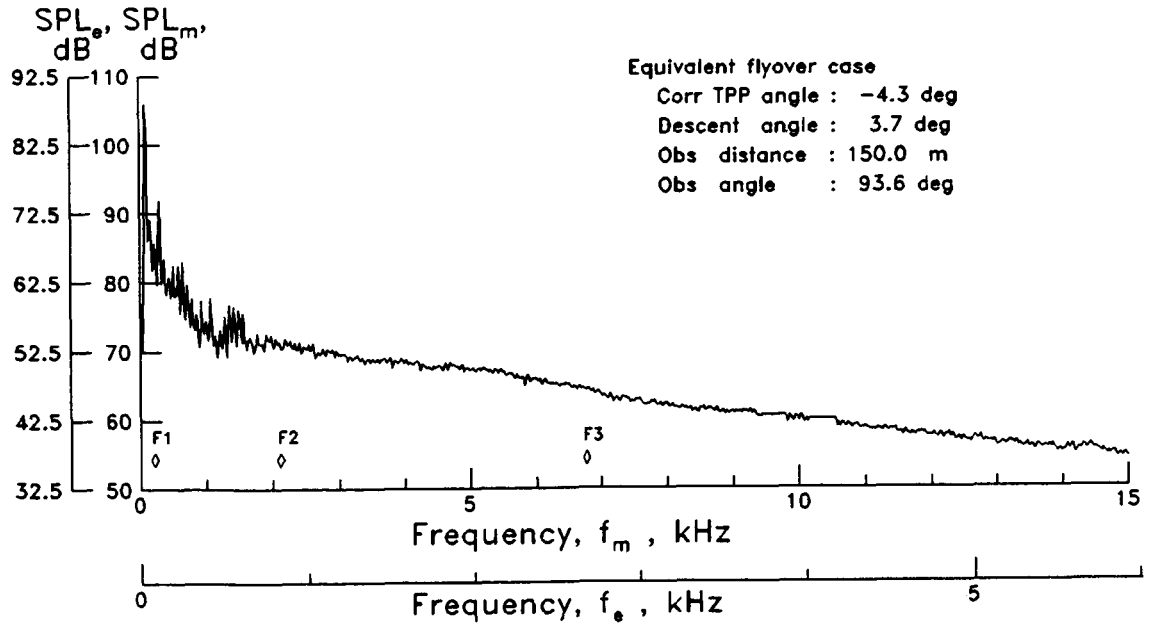

(t) $\alpha_{\mathrm{TPP}} = -3.9°$; $\mu = 0.281$. Run point 682.

Figure 18. Continued.

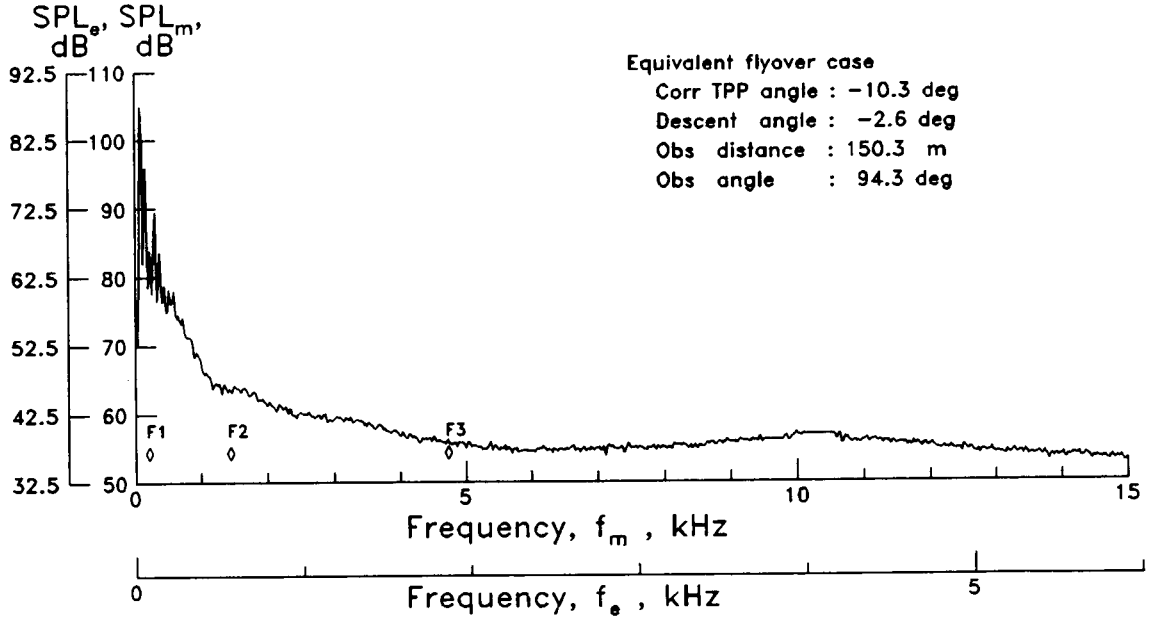

(u) $\alpha_{\mathrm{TPP}} = -9.9°$; $\mu = 0.278$. Run point 681.

Figure 18. Concluded.

National Aeronautics and Space Administration

Report Documentation Page

1. Report No.	2. Government Accession No.	3. Recipient's Catalog No.
NASA TP-2825		

4. Title and Subtitle	5. Report Date
Helicopter Main-Rotor Noise *Determination of Source Contributions Using Scaled Model Data*	August 1988
	6. Performing Organization Code
7. Author(s)	8. Performing Organization Report No.
Thomas F. Brooks, J. Ralph Jolly, Jr., and Michael A. Marcolini	L-16399
9. Performing Organization Name and Address	10. Work Unit No.
NASA Langley Research Center Hampton, VA 23665-5225	505-63-51-00
	11. Contract or Grant No.
12. Sponsoring Agency Name and Address	13. Type of Report and Period Covered
National Aeronautics and Space Administration Washington, DC 20546-0001	Technical Paper
	14. Sponsoring Agency Code

15. Supplementary Notes

Thomas F. Brooks and Michael A. Marcolini: Langley Research Center, Hampton, Virginia.
J. Ralph Jolly, Jr.: Planning Research Corporation, Hampton, Virginia.

16. Abstract

Acoustic data from a test of a 40-percent model MBB BO-105 helicopter main rotor are scaled to equivalent "full-scale" flyover cases. The test was conducted in the anechoic open test section of the German-Dutch Wind Tunnel (DNW). The measured data are in the form of acoustic pressure time histories and spectra from two out-of-flow microphones underneath and forward of the model. These are scaled to correspond to measurements made at locations 150 m below the flight path of a full-scale rotor. For the scaled data, a detailed analysis is given for the identification in the data of the noise contributions from different rotor noise sources. Key results include a component breakdown of the noise contributions, in terms of noise criteria calculations of dBA and PNL, as functions of rotor advance ratio and descent angle. It is shown for the scaled rotor that, during descent, impulsive blade-vortex interaction (BVI) noise is the dominant contributor to the noise. In level flight and mild climb, broadband blade-turbulent wake interaction (BWI) noise is dominant due to the absence of BVI activity. At high climb angles, BWI is reduced and self-noise from blade boundary-layer turbulence becomes the most prominent.

17. Key Words (Suggested by Authors(s))	18. Distribution Statement
Rotor acoustics Blade-vortex interaction noise Rotor broadband noise	Unclassified—Unlimited Subject Category 71

19. Security Classif.(of this report)	20. Security Classif.(of this page)	21. No. of Pages	22. Price
Unclassified	Unclassified	65	A04

For sale by the National Technical Information Service, Springfield, Virginia 22161-2171